8015595

LAWRENCE, GEORGE NELSON

OPTICAL PERFORMANCE ANALYSIS OF CARBON-DIOXIDE LASER
FUSION SYSTEMS

The University of Arizona PH.D. 1980

PLEASE NOTE:

In all cases this material has been filmed in the best possible way from the available copy. Problems encountered with this document have been identified here with a check mark ✓.

1. Glossy photographs ________
2. Colored illustrations ________
3. Photographs with dark background ________
4. Illustrations are poor copy ________
5. Print shows through as there is text on both sides of page ________
6. Indistinct, broken or small print on several pages ________ throughout ________
7. Tightly bound copy with print lost in spine ________
8. Computer printout pages with indistinct print ✓
9. Page(s) ________ lacking when material received, and not available from school or author ________
10. Page(s) ________ seem to be missing in numbering only as text follows ________
11. Poor carbon copy ________
12. Not original copy, several pages with blurred type ________
13. Appendix pages are poor copy ________
14. Original copy with light type ________
15. Curling and wrinkled pages ________
16. Other ________

OPTICAL PERFORMANCE ANALYSIS OF CO_2 LASER FUSION SYSTEMS

by

George Nelson Lawrence

A Dissertation Submitted to the Faculty of the

COMMITTEE ON OPTICAL SCIENCES (GRADUATE)

In Partial Fulfillment of the Requirements
For the Degree of

DOCTOR OF PHILOSOPHY

In the Graduate College

THE UNIVERSITY OF ARIZONA

1 9 8 0

THE UNIVERSITY OF ARIZONA
GRADUATE COLLEGE

As members of the Final Examination Committee, we certify that we have read the dissertation prepared by George Nelson Lawrence

entitled Optical Performance Analysis of CO_2 Laser Fusion Systems

and recommend that it be accepted as fulfilling the dissertation requirement for the Degree of ______________.

James C. Wyant — Date 2/7/80

Murray Sargent III — Date 2/6/80

______________ Date

______________ Date

______________ Date

Final approval and acceptance of this dissertation is contingent upon the candidate's submission of the final copy of the dissertation to the Graduate College.

I hereby certify that I have read this dissertation prepared under my direction and recommend that it be accepted as fulfilling the dissertation requirement.

Robert R Shannon — 2/7/80

Dissertation Director — Date

STATEMENT BY AUTHOR

This dissertation has been submitted in partial fulfillment of requirements for an advanced degree at The University of Arizona and is deposited in the University Library to be made available to borrowers under rules of the Library.

Brief quotations from this dissertation are allowable without special permission, provided that accurate acknowledgment of source is made. Requests for permission for extended quotation from or reproduction of this manuscript in whole or in part may be granted by the head of the major department or the Dean of the Graduate College when in his judgment the proposed use of the material is in the interests of scholarship. In all other instances, however, permission must be obtained from the author.

SIGNED: George N. Laurence

PREFACE

This dissertation discusses the theoretical basis for the LOTS computer program, which has been developed by this author to analyze the optical train of CO_2 laser fusion systems. This work has been carried out under contract from Los Alamos Scientific Laboratories to the Optical Sciences Center, University of Arizona, spanning the period from May 1976 to January 1980. Los Alamos provided the project, numerous problems to be solved, and the funds to solve them. My contributions have been to determine the scope and method of the optical train calculations and to develop the LOTS program and its theoretical bases.

Requests for a copy of the LOTS program (usable on CDC 6000 series computers using SCOPE or NOSIBE systems) and the LOTS Manual should be directed to Dr. J. Wyant, Principal Investigator for this project.

In my opinion the development of controlled nuclear fusion is a necessity if mankind is to maintain a high-technology civilization beyond the next century or two. The laser fusion programs at Los Alamos are among the most important scientific efforts being undertaken in our age. It will be a source of lifetime satisfaction to me to have made a small contribution to this project.

Working with the people at Los Alamos has been the most enjoyable part of this work. In particular I would like to thank Dr. I. Liberman for giving me the initial encouragement to undertake this project. V. K. Viswanathan, as the first user, struggled valiantly with the awkwardness and errors in the early versions of LOTS but nevertheless managed to get some use out of it and inspired me to continue. P. Wolfe provided invaluable assistance with the physics of the gain and saturation materials and with the LASL computer system. K. Jones and J. Munroe both gave generously of their time during my visits to LASL. Dr. W. Sweatt helped considerably with my understanding of the Antares system. I am indebted to J. Parker for the method of solving the gain equations for noncollimated beams.

I was extraordinarily fortunate in having Dr. J. Wyant as my Principal Investigator and Professor R. Shannon as my dissertation director. I would like to thank Dr. Wyant for having enough confidence to give me a free hand in the development of LOTS and Professor Shannon for sound advice, for a carefully calculated amount of pressure on me to finish, and for suggesting the method of creating random wavefronts. Dr. J. Loomis was a major influence in my education in computer programming.

I would like to thank Sunglan Kwon for help in programming, and to thank Sherrie Cornett and Kathy Seeley for patiently typing all these equations.

The University Computer Center provided invaluable assistance by maintaining accounting and operational systems that reward ingenuity.

I would like to thank my wife for far more patience than I could have reasonably expected with my long hours in the computer room.

TABLE OF CONTENTS

TABLE OF CONTENTS--Continued

LIST OF ILLUSTRATIONS

LIST OF ILLUSTRATIONS--Continued

LIST OF ILLUSTRATIONS--Continued

LIST OF TABLES

ABSTRACT

The components and phenomena which must be considered in the analysis of the CO_2 laser fusion system are described. The applicability of ray trace, interferogram reduction, and prior diffraction propagation programs is discussed. The basic structure of the LOTS CO_2 laser fusion analysis program is outlined. The general three-dimensional vector description of the laser pulse is simplified to a two-dimensional complex amplitude description. Methods of treating the nonlinear gain and saturable absorber media are developed. The numerical calculation of near-field diffraction distributions in noncollimated beams and the far-field diffraction distributions in spatial filters and imaging is discussed. Estimates of sampling errors are developed for the case of diffraction from a uniformly illuminated circular aperture for the near and far field. Methods of introducing interferometric data into the calculations are described. Smoothed random wavefronts are used to substitute for components known only by their specification values. Requirements and techniques of construction of these random wavefronts are explored. Capabilities and commands for the LOTS program are presented. A preliminary design of the Antares 100 kilojoule CO_2 laser fusion system is analyzed to demonstrate how the LOTS code is used.

CHAPTER 1

INTRODUCTION

Inertial confinement by means of high energy CO_2 lasers is one of the most promising of the techniques under development to achieve controlled nuclear fusion. The large, ambitious CO_2 laser fusion project at Los Alamos Scientific Laboratory poses many scientific and engineering challenges. Among these challenges is devising a method of predicting the wavefront quality and energy of the CO_2 laser pulse as a function of all the optical components in the system.

The laser optical train simulation (LOTS) code has been developed at the Optical Sciences Center, University of Arizona, for the Los Alamos Scientific Laboratory under the auspices of the U.S. Department of Energy and the University of Arizona to provide an end-to-end analysis of the laser fusion optical train. The LOTS code and considerations in its development are the subjects of this dissertation.

Description of a Typical Laser Fusion System

The pulsed CO_2 lasers in the laser fusion program range in size from the 100 J single beam system developed in 1973 to the 100 kJ, 72-beam Antares system to be completed in 1983. However, from the point of view of an optical engineering analysis--apart from changes of scale--the factors to be considered are similar in all CO_2 laser fusion systems.

A brief description of the Antares system will introduce the problems and considerations of the optical analysis. Figure 1.1 shows

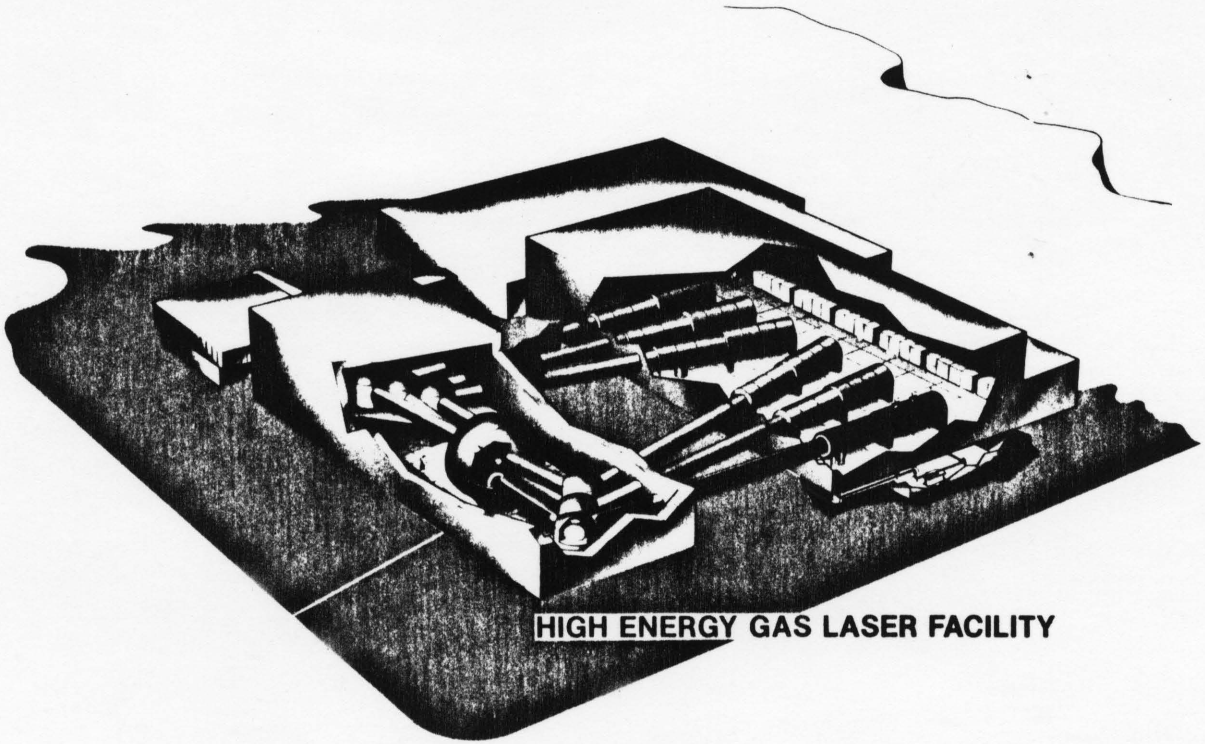

Fig. 1.1. Antares Laser Fusion System (Overview).

an artist's rendering of the Antares system. Six large power amplifiers are evident. The laser pulses from these six amplifiers are directed into the target chamber where they simultaneously strike the laser fusion target. Figure 1.2 shows one of the power amplifiers in greater detail. The amplifier emits an annular beam which is subdivided into 12 segments making 72 separate beams in all.

Figure 1.3 follows one of the beams through the power amplifier. An incident annular pulse entering at Station 1 is subdivided into 12 segments by a polyhedron mirror at Station 3. A discussion of some of the effects of window segmentation was discussed by Lawrence and Munroe (1977). From the polyhedron mirror one segment is followed as it travels through the rest of the system. The pulse is brought to a focus at Station 7 where a spatial filter (pinhole aperture) acts to remove aberrations and to provide protection from retroreflected pulses. The CO_2 gain media exists between the windows at Station 8 and Station 15. The regions designated by dashed lines have a strong positive gain coefficient. The rest of the region between Station 8 and Station 15 has a weak negative gain coefficient representing unpumped gas absorption.

A saturable absorber medium exists between Station 13 and Station 14. By lowering the small signal gain this material helps to prevent premature pulsing of the amplifier prior to the arrival of the pulse from the oscillator. The laser pulse is reflected from the mirror at Station 14 and returns through the saturable absorber and the four gain cells before exiting the gain medium at Station 15. The pulse encounters additional directing mirrors and a final focus mirror (not shown in Fig. 1.3) before hitting the target.

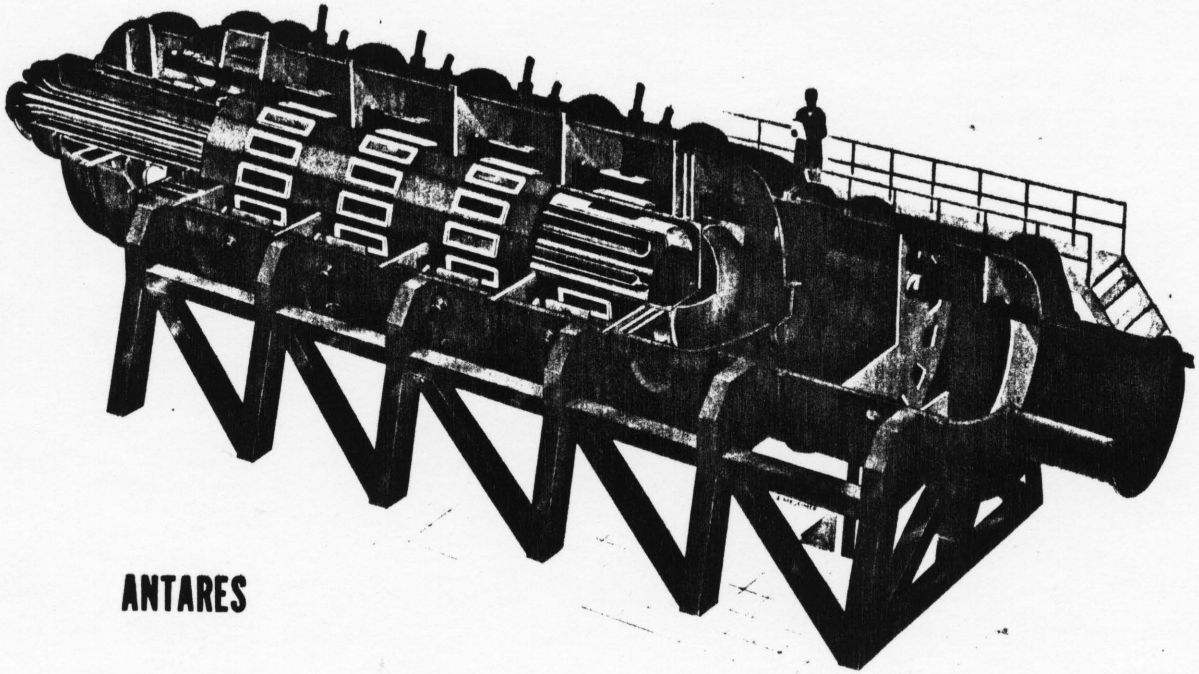

Fig. 1.2. Antares Power Amplifier.

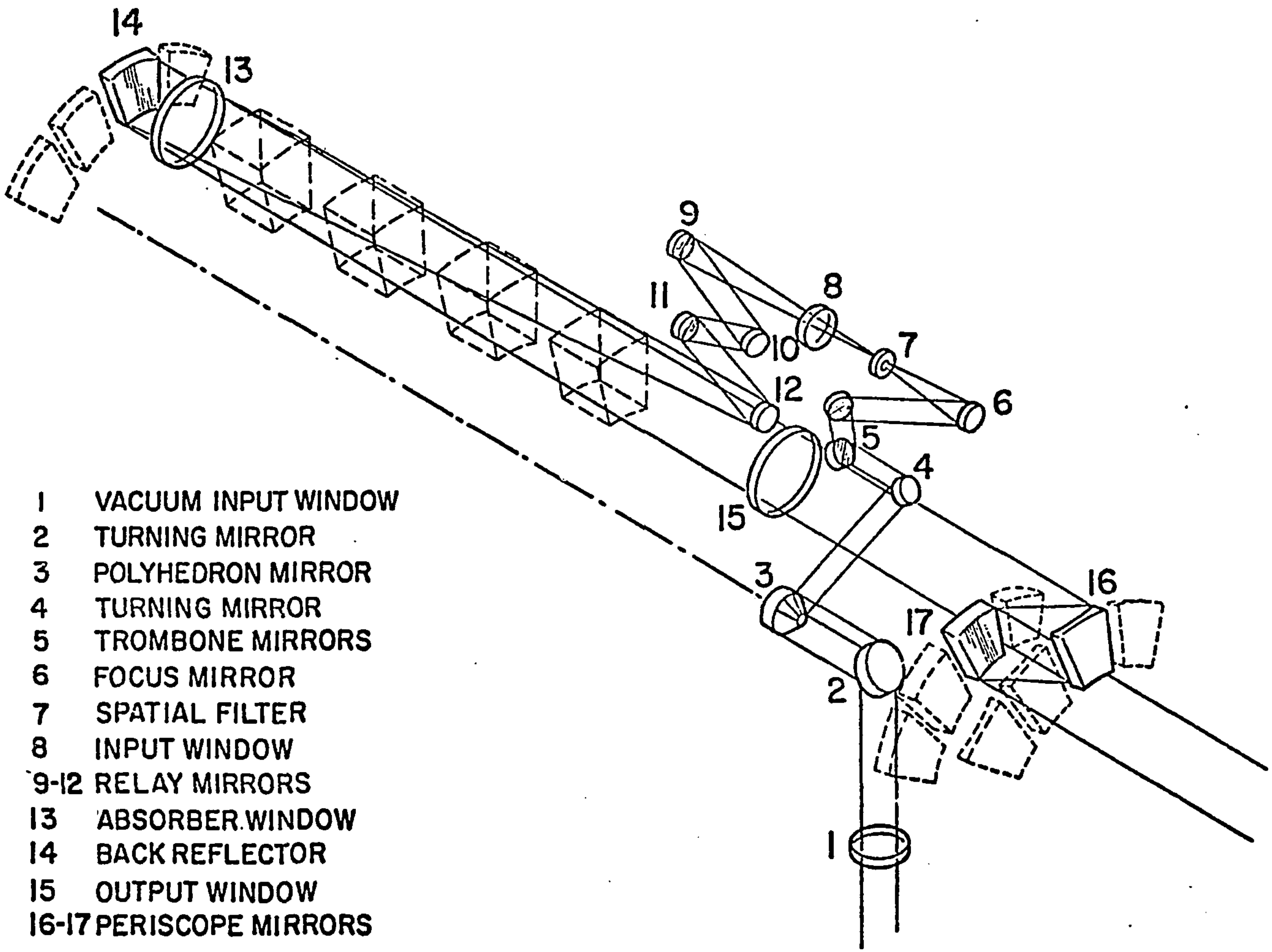

Fig. 1.3. Antares Power Amplifier Optical Schematic.

The factors that are necessary to model the laser fusion system are shown in Table 1.1.

Table 1.1. Factors Considered.

Nonlinear gain
Saturable absorbers
Diffraction propagation
Spatial filters
Aberrated components
Clear apertures
Attenuation

The nonlinear gain and diffraction propagation calculations must be valid for collimated and converging or diverging beams.

When the front end of the system is included, calculations may consider 100 or more optical surfaces. To facilitate analysis of this type of system at reasonable cost, it is necessary to have a flexible and efficient computer program.

At the laser fusion target, the interaction of the multiple beams and the target material is a highly complex process which is the subject of considerable research as the laser fusion program advances. The scope of the optical analysis to be performed with LOTS is limited to predicting the performance of one beam independently of the other beams and without consideration of target interaction. Thus LOTS cannot be used for determining the design goals of the laser train but rather is used for predicting how well these goals are met.

From this brief description of the CO_2 laser fusion system it is apparent that analysis of the system is a complex task. In order to develop a flexible and efficient analysis program it is necessary to make realistic decisions on the degree of physical detail included. The philosopy adopted in the development of LOTS has been to treat the physical factors to a degree of precision necessary to make valid engineering decisions from the calculations. This approach has not only led to a program efficient in computer central memory and central processor time but has kept the software development time within the schedule constraints of the laser fusion system. Without this practical attitude, LOTS could not have been completed in time to be useful in analyzing the system.

Existing Analytical Tools

In defining the scope of the LOTS program it was necessary to consider the applicability of existing optical analysis techniques.

Ray Trace Programs

The principal analytical tools for analyzing conventional optical systems are ray trace programs. These programs do an excellent job of determining the aberrations of optical systems as a function of the idealized geometry of the system. Tilt or decenter of components may be considered but surface inaccuracy of arbitrary shape can be considered only with difficulty. In the laser fusion system the F-numbers are generally very large and the cumulative aberration from idealized components is essentially negligible. The final focusing mirrors are of moderately low F-number but are parabolic so that for perfect alignment they are free of aberration. The chief cause of aberration in the laser fusion systems is manufacturing error. Chapter 5 addresses idealized component error and manufacturing error in detail.

In addition to being unable to handle manufacturing error readily, ray trace programs cannot handle spatial filters or near-field diffraction, nor can they treat general nonuniform intensity.

Because of the ease with which ray trace programs may be used to determine the ideal geometry aberration or the first order properties of the beam, it was assumed that ray trace analysis would be done on every system as a first step. LOTS was therefore designed to handle perturbations to the optical beam about a nominal optical axis and aberrations to the beam which are due either to manufacturing error or to ideal component error as determined by a ray trace program.

Gaussian Beam Calculations

Analytical solutions to the diffraction propagation of Gaussian beams are well known. Even the problems of truncated Gaussian beams with phase errors have been studied analytically (Lowenthal, 1974). Gaussian beam theory is useful in the immediate vicinity of the oscillator. However, clipping of the beam by apertures, nonlinear gain, and the coupling of phase errors into nonuniform energy density by propagation and spatial filters alter the energy density profile so that the laser beam is no longer Gaussian. It is necessary to use a general approach that makes no assumptions about the energy density distribution.

Diffraction Propagation Programs

Considerable work has been done on diffraction propagation in laser amplifiers. Table 1.2 lists several techniques with a reference describing the technique.

Table 1.2. Propagation Techniques.

Hermite-Gaussian (Siegman and Sziklas, 1974)
Fast Fourier Transform (Sziklas and Siegman, 1975)
Finite Difference Technique (Rench, 1974)
Spline Expansion (Lax, Agrawal and Louisell, 1979)

The propagation technique used in LOTS is the fast Fourier transform (FFT) approach. This technique is considered to be the fastest for propagation steps of arbitrary size (Sziklas and Siegman, 1975). The spline expansion technique was published after completion of work on LOTS. It offers advantages of increased accuracy but there is a penalty of increased computational time and increased program complexity. This technique merits consideration in future efforts.

The programs listed in Table 1.2 have been developed to do propagation in reasonator cavities and for large CW CO_2 laser systems. LOTS shares its FFT technique with many of these programs. The problems of resonator designers, CW laser system designers, and CO_2 pulsed laser fusion system designers are very different. Commonality between programs is essentially limited to the FFT propagation technique.

Interferogram Data Reduction Programs

The task of interferogram data reduction requires a complex and specialized program. LOTS takes the data from an interferogram reduction program such as FRINGE (Loomis, 1976) in the form of polynomial coefficients or in the form of a complex array of phase errors.

Input-Output Scheme for LOTS

Based on the factors of Table 1.1 and the existing analytical tools discussed in the last section, the flow of information into and out of LOTS takes the form shown schematically in Fig. 1.4. The initial pulse distribution may be defined as a truncated Gaussian, or if necessary, in more general fashion by a complex multiplying array. Optical elements are defined in terms of focal length, aperture shapes and sizes, aberrations, and efficiency. Laser amplifier and saturable absorber characteristics may be entered as well as the effective propagation distance.

The complex amplitude distribution is the fundamental pulse representation, and parameters such as the wavefront quality or pulse energy may be determined from the complex amplitude distribution at any point in the optical train.

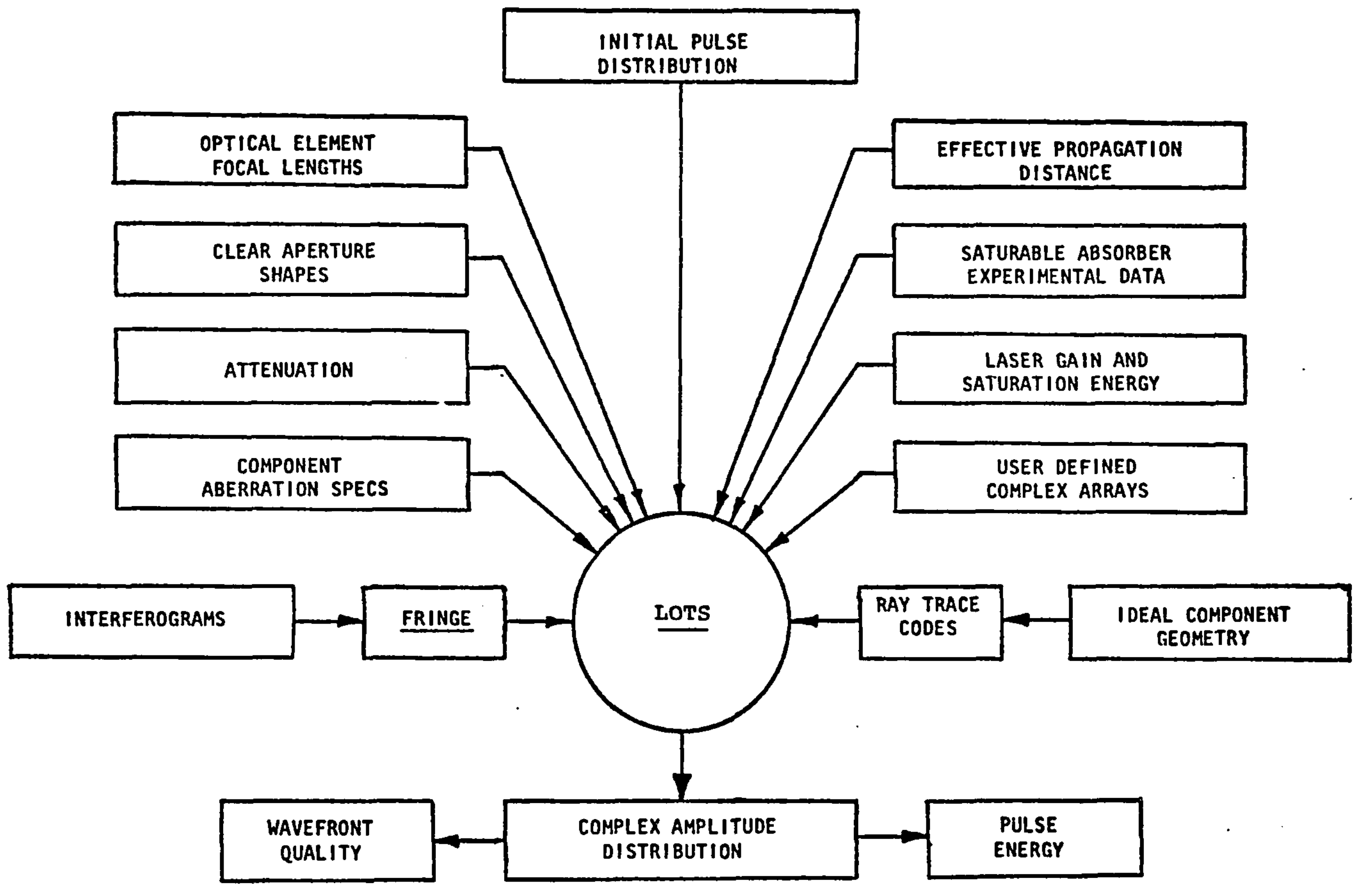

Fig. 1.4. Flow Chart for the LOTS Program.

CHAPTER 2

REPRESENTATION OF THE LASER PULSE

The most general representation of the laser pulse is a three-dimensional vector wavefront traveling at the speed of light in the medium. It is most convenient to work with retarded time, t_r, defined by

$$t_r = t - \frac{z}{c} ,$$

where t is the usual time variable, z is the spatial coordinate along the direction of propagation, and c is the speed of light in the medium. In this scheme the pulse is described by two spatial coordinates transverse to the direction of travel and the retarded time with some point on the pulse taken as zero retarded time.

Vector versus Scalar Theory

In general, vector theory is required when beams of radiation interfere at large angles, when large numerical aperture beams occur, or when birefringent effects are important. For accurate calculation of the effect of multiple beams (such as exist in the Helios and Antares systems) as they interfere at the target, vector theory is required. Because the scope of LOTS is limited to one beam at a time, this problem does not arise.

Scalar theory is reasonably valid at convergence angles of f/2 but becomes somewhat inaccurate at convergence angles faster than f/1.

This problem has been considered by Richards and Wolfe (1959) for uniform irradiance beams and by Innes and Bloom (1966) for Gaussian beams. The convergence angles of the existing laser fusion systems satisfy the F-number requirements for accuracy. However, the user should be cautious of results for other systems having F-numbers less than one.

At the time of this writing birefringent effects have not been considered a significant source of error in the CO_2 laser fusion systems.

The elements most likely to introduce birefringent effects are the salt windows used in the power amplifier which are about 4 in. thick. These windows are used at nearly normal incidence so birefringent effects should be small. Most of the other elements are reflective.

The laser pulse may therefore be considered as a time-varying irradiance distribution.

Basis for Energy Density Description

As discussed in Chapter 4, the CO_2 gain medium may be described by the rate equation approximation. Where this approximation is applicable, coherent quantum effects may be ignored and it is necessary to deal only with the time integrated irradiance, i.e., the energy density distribution.

For fast-reacting saturable absorbers the response is a function of the time-varying irradiance distribution. However, it is anticipated that experimental data will take the form of transmission versus energy density measurements using pulse shapes representative of the laser fusion pulse. The results of calculations on the system are not strongly affected by the saturable parameters so that a high degree of accuracy is not required.

The energy density distribution, while adequate for gain and saturation calculations, is too great a simplification for the aberration calculations which require a complex representation. The solution to this problem is to use a complex amplitude distribution defined such that if E(x,y) is the energy density in joules per square centimeter,

$$E(x,y) = A(x,y)A^*(x,y). \tag{2.1}$$

A(x,y) is the complex amplitude distribution with units of square root joules per centimeter.

Computer Representation of the Pulse

The complex amplitude distribution is represented in the computer as a two-dimensional complex array. Based on sampling considerations as discussed in Chapter 3, it is desirable to have the matrix as large as possible to improve the accuracy of diffraction calculations. For efficient calculation, the FFT routines discussed in Chapter 3 require that the entire matrix be held in central memory and further, for maximum efficiency, the matrix should contain 2^b elements per side, where b is an integer. Typical program lengths, even with considerable overlay subdivision are approximately $40,000_8$ where the subscript 8 indicates a number in octal base. A 64 x 64 complex matrix requires an additional $20,000_8$ giving a running length of $60,000_8$. This value is quite practical on the Los Alamos CDC 6600 or the University of Arizona Cyber 175. This size matrix was selected for the LOTS program. The next larger size array is 128 x 128 and requires $100,000_8$ for the matrix and a running length of $140,000_8$. On either computer system this size is considerably less practical. Turn-around time is significantly longer. A calculation of the type described in Chapter 7 requires about 40 seconds on the Cyber 175 and about 200 seconds on the CDC 6600 with the 64 x 64 matrix. Increasing the matrix size to 128 x 128 would increase running time by a factor of four with only a factor of two increase in sampling rate.

Recognizing that certain problems of diffraction spillover cannot be handled by a 64 x 64 array, LOTS was designed for maximum efficiency at this size as the best compromise for the majority of problems in the optical analysis of the laser fusion system.

CHAPTER 3

DIFFRACTION CALCULATIONS

In the laser fusion systems, diffraction calculations are divided into two basic types: the far field calculations used for the final distribution at the target and in spatial filters and the near field calculations used for diffraction propagation. Subject to the restrictions discussed in Chapter 2, scalar diffraction theory is adequate for these calculations. For the purposes of calculating the beam aberrations and energy, the theory may be further restricted to Fresnel diffraction theory. Fresnel theory is appropriate when the propagation distance z meets the condition (Gaskill, 1978, p. 366)

$$z^3 > \frac{\pi(a_1+a_2)^4}{4\lambda}, \tag{3.1}$$

where a_1 is the maximum extent of the diffracting aperture and a_2 is the maximum extent of the field. The Fresnel number defined as

$$F \equiv \frac{a^2}{\lambda z} \tag{3.2}$$

is commonly used as a measure of diffraction effects. The inequality of Eq. (3.1) becomes important at high Fresnel numbers where it is most restrictive when $a_1 = a_2$. For this condition the Fresnel theory is valid if

$$F < \frac{a^{2/3}}{\lambda^{2/3}\,\pi^{1/3}\,2^{2/3}}. \tag{3.3}$$

The smallest aperture used in the laser fusion system is about 1 cm in radius. This requires that the Fresnel number be less than 41. For an aperture of 10 cm radius the Fresnel number must be less than 192. For the purposes of calculating the beam aberrations and energy, the diffraction effects at these high Fresnel numbers are insignificant and no noticeable error arises from using the Fresnel theory or from ignoring diffraction entirely. As discussed in the sampling section, the finite size of the matrix will prove to be a greater limitation.

The basic Fresnel diffraction propagation equation to transfer from plane 0 to plane 1 is

$$p_1(x,y) = p_0(x,y) ** h(x,y), \tag{3.4}$$

where

$$h(x,y) = \frac{1}{j\lambda z} \exp\left(j \frac{\kappa r}{2z}\right)$$

$r^2 = x^2 + y^2$

z = propagation distance

κ = wave number

** = two-dimensional convolution.

The constant phase factor e^{jkz} is neglected.

Far-Field Diffraction

For convergent or divergent beams it is useful to separate the phase curvature from the rest of the complex distribution. To this purpose we define f(x,y) such that

$$p(x,y) = f(x,y) \exp\left(-j \frac{\kappa r^2}{2z}\right), \tag{3.5}$$

where z is the radius of curvature. Applying the usual factorization (Goodman, 1968), Eq. (3.4) becomes

$$p_1(x_1,y_1) = \frac{1}{j\lambda z} \exp\left(j \frac{\kappa r_1^2}{2z}\right) FF\left[p_0(x_0,y_0) \exp\left(j \frac{\kappa r_0^2}{2z}\right)\right]$$

$$\xi = \frac{x_1}{\lambda z}, \qquad \eta = \frac{y_1}{\lambda z} \tag{3.6}$$

where

ξ,η = spatial frequency variables

FF = two-dimensional Fourier transformation.

To propagate to the center of curvature of the wavefront, Eq. (3.5) is substituted into Eq. (3.6) to give

$$p_1(x_1,y_1) = \frac{1}{j\lambda z} \exp\left(j \frac{\kappa r_1^2}{2z}\right) FF\left[f_0(x_0,y_0)\right]. \tag{3.7}$$

Equation (3.7) is used to calculate the distribution at the target and at the focus of a spatial filter. In the case of the spatial filter the distribution is operated on by the aperture and then expanded and recollimated. The expansion is represented by Eq. (3.6) but the recollimation cancels the quadratic phase factor outside the square bracket giving the distribution at plane 2 at the end of the spatial filter,

$$f_2(x_2,y_2) = \frac{1}{j\lambda z} FF\left[p_1(x_1,y_1) \exp\left(j \frac{\kappa r_1^2}{2z}\right)\right]. \tag{3.8}$$

Strictly speaking, Eq. (3.8) is not a far-field calculation because of the quadratic phase factor, but for focal lengths of the order of a few meters or less the quadratic factor is sufficiently small that the far field label is appropriate.

The fundamental equations for far-field calculations are Eq. (3.7) for imaging and Eq. (3.8) for recollimation.

Near-Field Calculations

While it is essential to include the far-field diffraction calculations, the need for near-field calculations is less pressing. From the viewpoint of the laser fusion system calculations the importance of diffraction decreases as the Fresnel number increases. Since the matrix size and computational time increase as the square of the Fresnel number of the calculations, it is important to be practical in determining the Fresnel number requirements of the program.

Circular apertures exhibit considerable diffraction structure in the intensity pattern at the center of the aperture (Fig. 3.1). Square apertures similar to the trapezoidal apertures used in Antares show less structure in the intensity pattern in the center (Fig. 3.2). High spatial frequency intensity variations such as are shown in Figs. 3.1 and 3.2 will be almost completely smoothed out by a spatial filter with a radius of the order of the first or second dark ring in the Airy pattern. If a spatial filter does not remove these effects then some change in energy extraction in a saturated amplifier would be expected. To test this effect a calculation was done with a configuration similar to the final pass of the Antares power amplifier. A pulse was passed through the last part of the amplifier, in one case assuming no diffraction, and in another case assuming diffraction of Fresnel number 10 had occurred. A square aperture of 40 cm on a side was applied before and after the diffraction propagation. Including the effects of diffraction

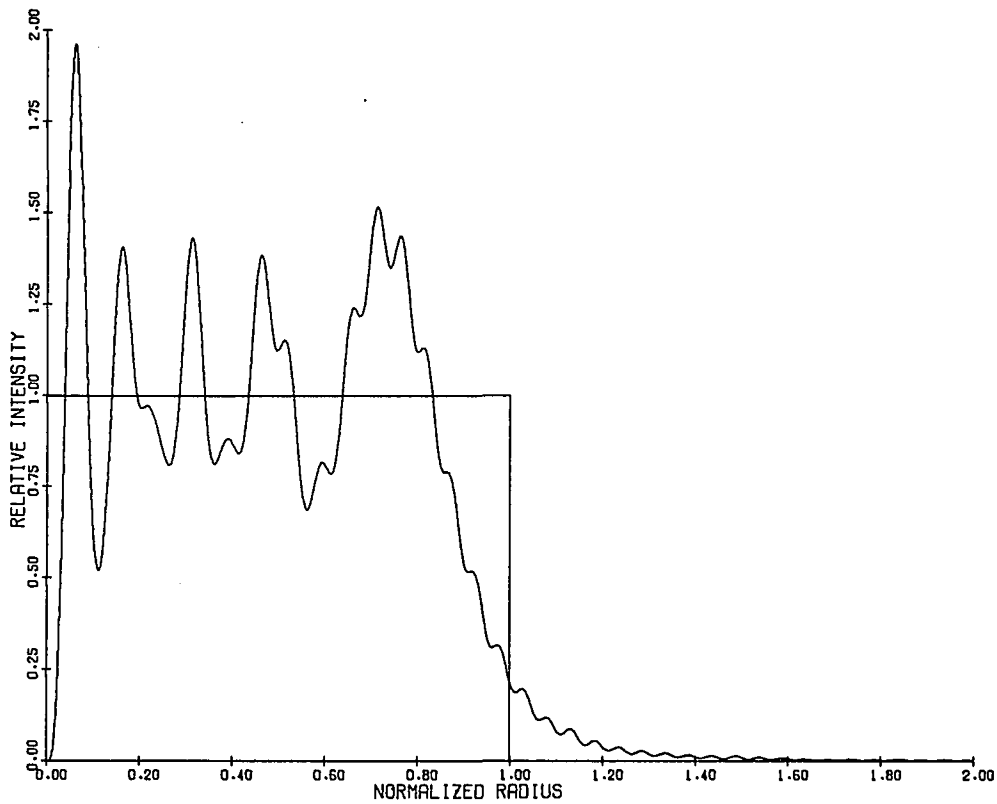

Figure 3.1. Diffraction Pattern for a Circular Aperture at a Fresnel Number of 10.

The pattern is shown with the center on the left. The geometrical distribution is also shown.

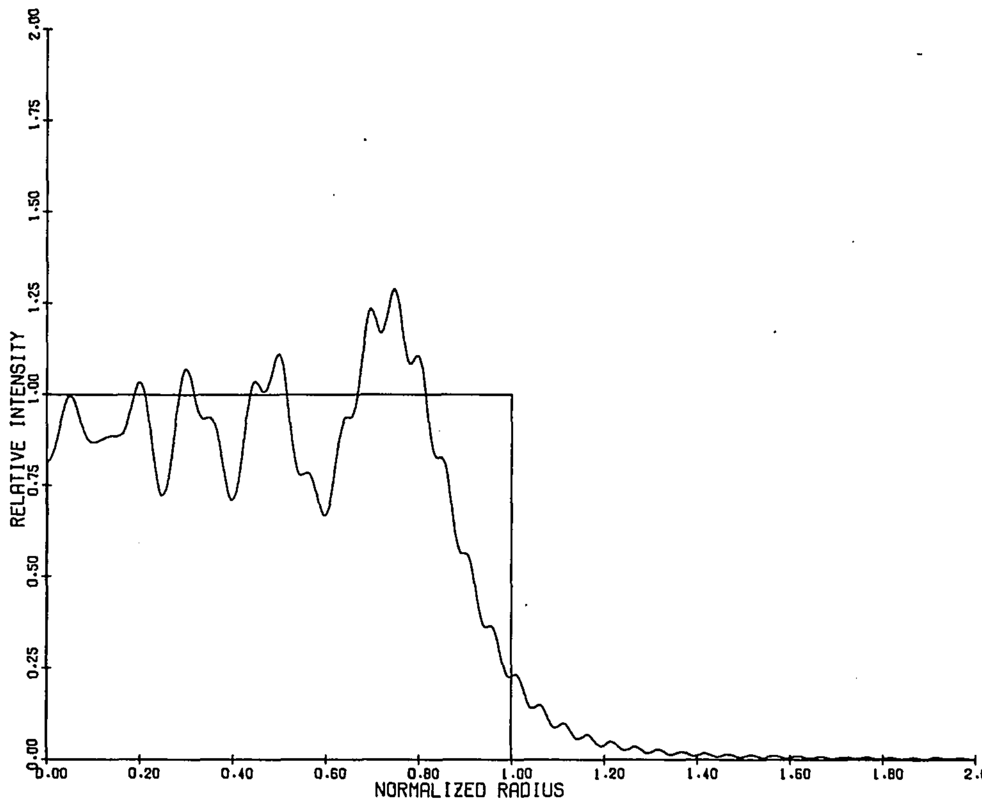

Figure 3.2. Diffraction Pattern of a Square Aperture with a Fresnel Number of 10.

losses at the second aperture, energy extraction was 3.27% lower in the amplifier when diffraction was considered. Figure 3.3 shows an intensity profile of the distribution before and after the saturated gain. The intensity variations are considerably smoothed out. Calculations with the same parameters using a circular aperture gave an energy extraction of 3.48% less when diffraction was considered. This slightly larger value is attributed to the center structure in the circular pattern.

The phase of the distribution is perturbed by diffraction as well as the energy density. Chapter 4 discusses the advantages of using the Strehl ratio as a measure of the wavefront aberration. For this discussion it may be defined as

$$\text{Strehl ratio} = 1 - {\frac{2\pi}{\lambda}}^{2} \sigma^2, \tag{3.9}$$

where σ is the RMS wavefront error. To measure the effect of phase errors due to diffraction, the following configuration was used in calculation. Light filling a circular aperture uniformly was propagated a distance defined by the Fresnel number and then the distribution was truncated by a second aperture d the same size as the first. This configuration is typical of the laser fusion system. Table 3.1 contains a list of the Fresnel numbers and corresponding Strehl ratios. At a Fresnel number of 10 the Strehl ratio is 0.976, corresponding to 1/40 wave of RMS aberration according to Eq. (3.9). Only a 1% improvement is realized at a Fresnel number of 40.

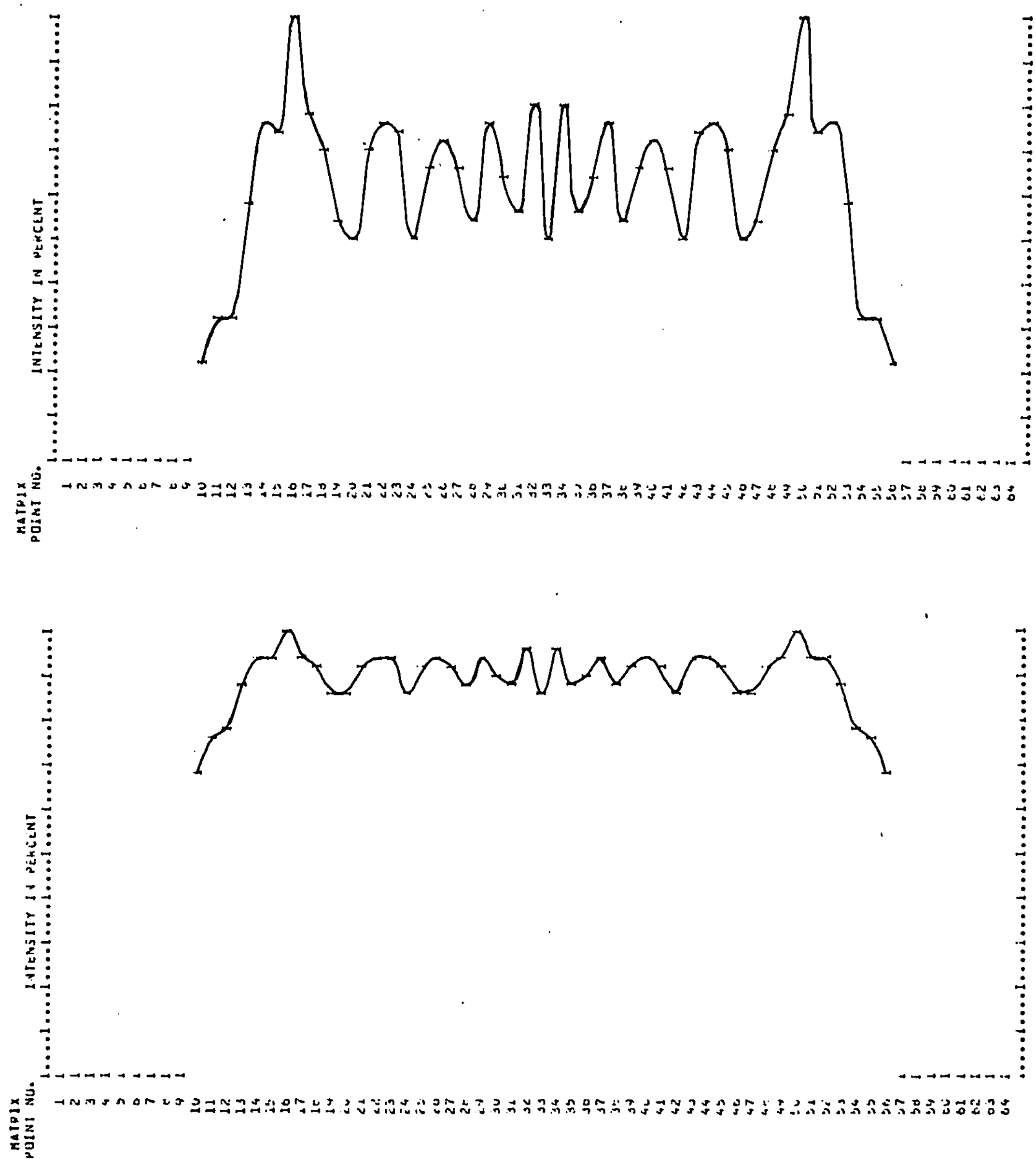

Figure 3.3. Relative Energy Density Profile before and after Saturated Gain.

The upper plot shows a circular diffraction pattern at a Fresnel number of 10. The lower plot shows the energy density profile after saturated gain, similar to the Antares power amplifier, has been applied.

Table 3.1. Strehl Ratio Versus Fresnel Number.

Fresnel Number	Strehl Ratio
5	0.968
10	0.976
20	0.982
40	0.986

For the same configuration and a Fresnel number of 10, the radius encircling 80% of the energy in the far-field pattern is increased by only 1.3% compared with the far field pattern with no diffraction.

In the front end of the system apertures are typically 1 cm and a Fresnel number of 10 corresponds to a propagation distance of 1 m. Since there are propagation distances greater than 1 m, it was decided to provide near-field diffraction capability. However, because of spatial filters and saturated gain, the final energy density distribution is relatively insensitive to changes in the front end. After the beam is expanded through the power amplifier the beam is about 15 cm in radius in the Helios system and about 20 cm in the Antares system. These correspond to 225 m and 400 m respectively to achieve a Fresnel number of 10. These distances are considerably longer than the propagation distances in the two systems and there is therefore little point in including near-field diffraction after the beam is expanded in the power amplifier.

The low information value of high Fresnel number calculations is stressed, not because it is difficult, but because it is commonly misunderstood. It is common in unstable resonator design to deal with Fresnel numbers of the order to 5 to 60 (Rench and Chester, 1973). For the higher Fresnel numbers the finite difference technique is most efficient. In this technique the aperture function is given a soft edge expressly to reduce the diffraction ripples (Rench, 1974). While this approach is not questioned by this author for designing unstable resonators, for the purposes of calculating high Fresnel number diffraction patterns it is hardly better than geometrical theory.

Equation (3.4) may be Fourier transformed to yield

$$P_2(\xi,\eta) = P_1(\xi,\eta)H(\xi,\eta;z), \qquad (3.10)$$

where

$$H(\xi,\eta;z) = \frac{1}{j\lambda z}\exp[-j\pi\lambda z(\xi^2+\eta^2)].$$

Capital letters indicate frequency domain distributions, and lowercase letters indicate spatial domain distributions. This form of the equation is more efficient computationally than the convolution of Eq. (3.4) because of the fast Fourier transform (FFT) algorithm. Equation (3.10) may be rewritten as

$$p_2(x,y) = FF^{-1}\{H(\xi,\eta;z)FF[p\ (x,y)]\}. \qquad (3.11)$$

For noncollimated beams the quadratic phase factor due to the phase curvature may be removed from the calculation by defining $f_1(x,y)$ and $f_2(x,y)$ similar to Eq. (3.5). With the conventions shown in

Fig. 3.4 as derived in Appendix A, Eq. (3.11) becomes

$$f_2(x_2,y_2) = FF^{-1}\{H(\xi,\eta;z_e)FF[f_1(x_1,y_1)]\} \tag{3.12}$$

where

$$z_e = \frac{z_1}{z_2}(z_2-z_1)$$

$$H(\xi,\eta;z_e) = \frac{z_1}{z_2}\exp[-j\pi\lambda z_e(\xi^2+\eta^2)]$$

$$x_2 = \frac{z_2}{z_1}x_1$$

$$y_2 = \frac{z_2}{z_1}y_1 .$$

The general Eq. (3.12) is the basic near-field diffraction equation. The effective propagation distance, z_e, may be used in Eq. (3.2) to give an effective Fresnel number.

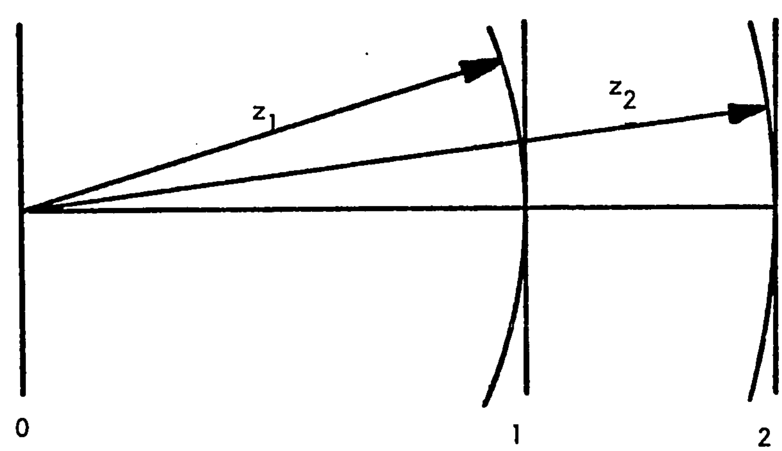

Figure 3.4. Expanding Wavefront Convections.

Discrete Fourier Transform

The continuous two-dimensional Fourier transform (CFT) and its inverse are defined by

$$H(\xi,\eta) = FF[h(x,y)] = \iint_{-\infty}^{\infty} h(x,y) \exp[-j2\pi(\xi x+\eta y)]dxdy, \tag{3.13}$$

where

$$h(x,y) = FF^{-1}[H(\xi,\eta)] = \iint_{-\infty}^{\infty} H(\xi,\eta) \exp[j2\pi(\xi x+\eta y)]d\xi d\eta. \tag{3.14}$$

In numberical calculations these transformations can be approximated by another set of transformations called discrete Fourier transforms (DFT). The DFT may be developed from the CFT (Brigham, 1974). A simpler but less rigorous approach is to make use of a limiting process.

If s is the length of one side of a square region and h(x,y) effectively vanishes for $|x|$, $|y| > s/2$, sampling interval T may be defined such that $s/T = N$. Then N is the number of sampled points. The integral in Eq. (3.13) is in the limit

$$\mathscr{L}_{N\to\infty} \left\{ \frac{1}{N^2T^2} \sum_{k=N/2}^{N/2-1} \sum_{\ell=-N/2}^{N/2-1} h(kT,\ell T) \exp\left[-j2\pi\left(\frac{km+\ell n}{N}\right)\right] \right\}$$

$$= \iint_{-\infty}^{\infty} h(x,y) \exp[-j2\pi(x\xi+y\eta)]dxdy. \tag{3.15}$$

In going from the CFT to the DFT the following conversions take place

$$\begin{array}{lll} x \to kT & \xi \to \dfrac{m}{NT} & d\xi \to \dfrac{1}{NT} \\ y \to \ell T & \eta \to \dfrac{n}{NT} & d\eta \to \dfrac{1}{NT} . \end{array} \tag{3.16}$$

Similarly the expression in Eq. (3.13) is in the limit

$$\mathscr{L}_{N\to\infty}\left\{T^2 \sum_{m=-N/2}^{N/2-1} \sum_{n=-N/2}^{N/2-1} H\left(\frac{m}{NT}, \frac{n}{NT}\right) \exp\left[j2\pi\left(\frac{km+\ell n}{N}\right)\right]\right\}$$

$$= \iint_{-\infty} H(\xi,\eta) \exp[j2\pi(x\xi+y\eta)]d\xi d\eta. \tag{3.17}$$

Since all summations are to be taken over the same limits, the following abbreviated notation will be used

$$\sum_{k=-N/2}^{N/2-1} = \sum_{k} \quad \text{for any variable } k.$$

The DFT and its inverse are defined respectively as

$$H\left(\frac{m}{NT}, \frac{n}{NT}\right) = T^2 \sum_{k\ell}\sum h(kT,\ell T) \exp\left[-j2\pi\left(\frac{km+\ell n}{N}\right)\right] \tag{3.18}$$

$$h(kT,\ell T) = \frac{1}{N^2T^2} \sum_{mn}\sum H\left(\frac{m}{NT}, \frac{n}{NT}\right) \exp\left[j2\pi\left(\frac{km+\ell n}{N}\right)\right]. \tag{3.19}$$

Several useful properties of the DFT are listed in Table B.1 with the corresponding CFT expressions.

Fast Fourier Transforms

The fast Fourier transform (FFT) is generally the most efficient method of computing the DFT for large arrays (Brigham, 1974). FFT computer routines accomplish the following function

$$FFT(f;J,N) = \sum_{k\ell}\sum f(kT,\ell T) \exp\left[j2\pi J\left(\frac{km+\ell n}{N}\right)\right] \tag{3.20}$$

$$J = \begin{cases} -1 \text{ for forward transform} \\ 1 \text{ for inverse transform.} \end{cases}$$

The DFT can be expressed as

$$H\left(\frac{m}{NT}, \frac{n}{NT}\right) = T^2 FFT(h;-1,N). \tag{3.21}$$

The inverse DFT is

$$h(kT,\ell T) = \frac{1}{N^2T^2} FFT(h;1,N). \tag{3.22}$$

Sampling Theory Applied to Diffraction

Calculation of the Fresnel diffraction pattern of a uniformly illuminated circular aperture is representative of some of the problems encountered in the laser pulse propagation calculations. The principal considerations are the choice of the number of sampled points across the aperture and the ratio of the aperture width to the matrix width. The well known sampling theorem states that a sampled function may be perfectly reconstructed if the sampling rate is twice the highest frequency present. A nonperiodic distribution represented on a finite matrix cannot be band limited and must therefore have errors due to sampling.

It is sometimes convenient in this discussion to work in matrix units, i.e., T = 1. Under this condition the spatial frequency at the edge of the aperture matrix in the frequency domain is ½.

Sampling in the Far Field and Frequency Domain

For near field diffraction using Eq. (3.12) aliasing may occur in either the spatial or frequency domain. The considerations of aliasing in the frequency domain are the same as those for the far field calculations of Eq. (3.7) and Eq. (3.8) and will be the first ones to be addressed. In both the far field and frequency domain cases the distribution is an Airy pattern. The energy density distribution takes the form

$$E(\rho) = \frac{2J_1(2\pi a\rho)^2}{2\pi a\rho} \tag{3.23}$$

where

J_1 = Bessel function of the first kind of order one.

a = aperture radius

ρ = spatial frequency.

From Appendix C, the asymptotic expression for the envelope of the Airy pattern, valid for $a\rho > 1$, is

$$E(\rho) \approx \frac{1}{\pi^4 a^3 \rho^3} . \tag{3.24}$$

Since this discussion is being carried out in matrix units, $\rho = \frac{1}{2}$ at the edge of the frequency matrix. The normalized value of energy density at the edge is

$$E_{edge} \approx \frac{8}{\pi^4 a^3} . \tag{3.25}$$

Had the envelope of the Airy pattern fallen off to zero at the edge of the matrix, there would be no aliasing. E_{edge} represents an approximate measure of the aliasing error in the vicinity of the edge. Since the aperture radius, a, is measured in matrix units, Eq. (3.25) allows estimation of the alias error in the frequency or far field distribution. It is worth emphasizing that this error is independent of the matrix size, provided, of course, the aperture fits inside the matrix.

The argument just stated seems to suggest that the aperture radius should be as large as possible. This may shrink the frequency distribution to an objectional degree. The first dark ring of the Airy pattern occurs at a spatial frequency of

$$\rho = \frac{0.61}{a} . \tag{3.26}$$

In the frequency domain each matrix point represents an interval of frequency of 1/NT. Then for T = 1, the frequency radius r in matrix units is

$$r = 0.61 \frac{N}{a} \tag{3.27}$$

where N is the number of points on one side of the matrix. Thus resolution in the frequency domain may set an upper limit on the aperture radius and consequently a lower limit on aliasing error for a given matrix size.

Sampling in the Near Field

Equation (3.25) specifies the minimum size of a uniform aperture for a given amount of aliasing in the frequency domain or far field. Since the uniform aperture is featureless, the spatial domain could be ignored. Near field diffraction introduces structure into the spatial distribution and the following discussion addresses the sampling interval needed to resolve these diffraction details. The point spread function for free space propagation of Eq. (3.4) contains a quadratic phase factor which may be expressed as

$$h(x,y) = \frac{1}{j\lambda z} \exp\left(j\pi F \frac{r^2}{a^2}\right) \tag{3.28}$$

where

F = Fresnel number

$r = x^2 + y^2$

a = aperture radius.

In the integral notation for convolutions, Eq. (3.4) is

$$p_1(x,y) = \iint_{-\infty}^{\infty} p_0(\alpha,\beta)h(x-\alpha,y-\beta)d\alpha d\beta \tag{3.29}$$

where

$$h(x,y) = \frac{1}{j\lambda z} \exp\left(j \frac{\kappa r^2}{2z}\right).$$

An appropriate measure of the frequencies present in the circular aperture diffraction pattern is obtained by the rate of change of the quadratic phase factor as it intersects the edges of the aperture. In this calculation h(x,y) is rewritten in terms of the Fresnel number, F,

$$h(r^2) = \frac{1}{j\lambda z} \exp\left(j\pi F \frac{r^2}{a^2}\right). \tag{3.30}$$

The phase velocity is then

$$\frac{d\theta}{dr} = 2\pi F \frac{r}{a}, \tag{3.31}$$

corresponding to a spatial frequency, f, such that

$$f = F \frac{r}{a^2}. \tag{3.32}$$

Equation (3.32) gives the frequency of the quadratic phase factor at a distance, r, from the center for an aperture of radius, a, at a Fresnel number of F.

Figure 3.5 shows a circular aperture truncating a zone plate representing the point spread function of diffraction propagation for different amounts of decentration of the quadratic phase factor and the aperture. The upper pattern on the left in Fig. 3.5 shows six zones corresponding to F = 6. This pattern corresponds to a value for $p_1(0,0)$ in Eq. (3.29). Because the area of the zones are equal in the Fresnel approximation, $p_1(0,0) = 0$ for any even Fresnel number. Figure 3.6 shows the intensity pattern at F = 6 from the center to the edge. As expected, the intensity is zero at a normalized radius of zero.

Equation (3.32) suggests that the perimeter of the aperture causes modulation of the amplitude pattern at frequency f = 6. Because (as seen in Fig. 3.5) the modulation sits on a large bias level, the frequency content of amplitude and intensity patterns is similar and the intensity pattern should also exhibit the frequency f = 6. Measurement on Fig. 3.6 gives a value of f = 5.9 approximately. The rationale for use of Eq. (3.32) in this fashion becomes clear upon further examination of Fig. 3.5. The upper center pattern shows the point spread function shifted to the right to pass part of Zone 7 on the left and obscure part of Zone 6 on the left corresponding to point p_1 in Fig. 3.6. If the white or odd zones are assigned a positive value, then the center pattern has gained a positive contribution from Zone 7 and lost a negative contribution from Zone 6. The value of the corresponding integral is no longer zero. The center pattern corresponds approximately to the peak in Fig. 3.6 at a normalized radius of 0.1. Moving the point spread function further to the right partly reverses the

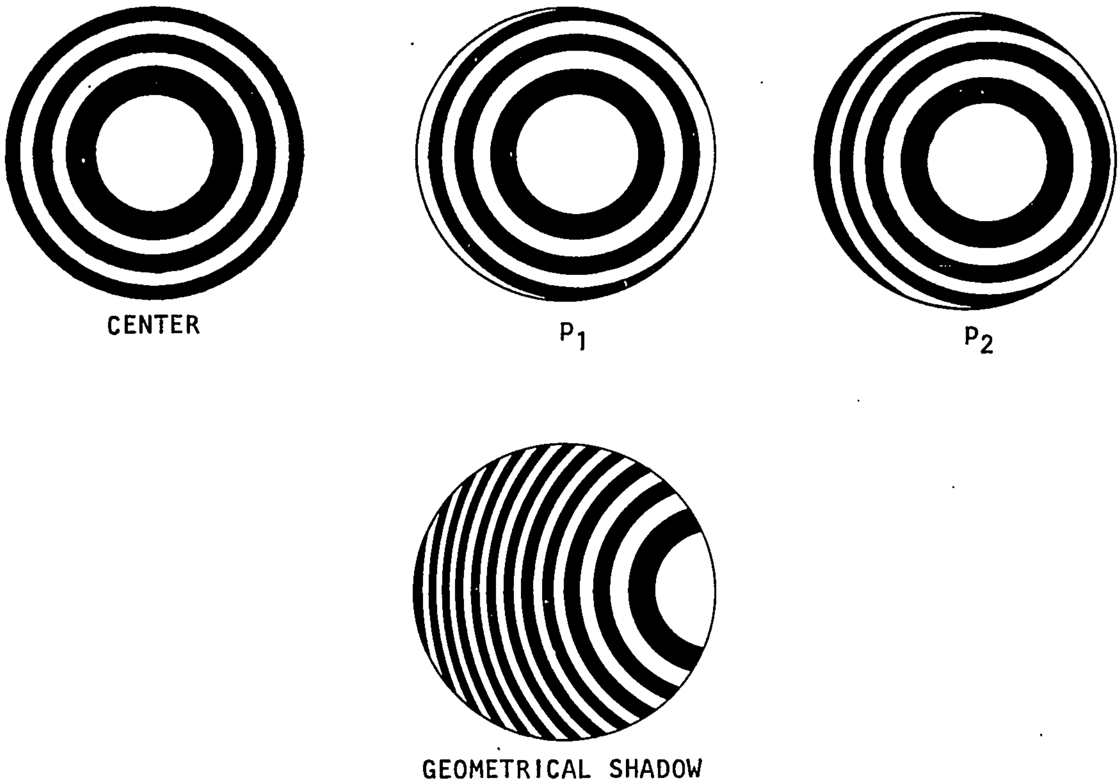

Figure 3.5. Fresnel Zones for Different Decentered Positions of the Aperture.

The Fresnel number is 6. The left pattern is centered showing six zones. The upper pattern in the center shows part of Zone 7 on the left. The right pattern shows part of Zone 8 and Zone 7 on the left. The lower pattern shows the condition at the geometrical shadow.

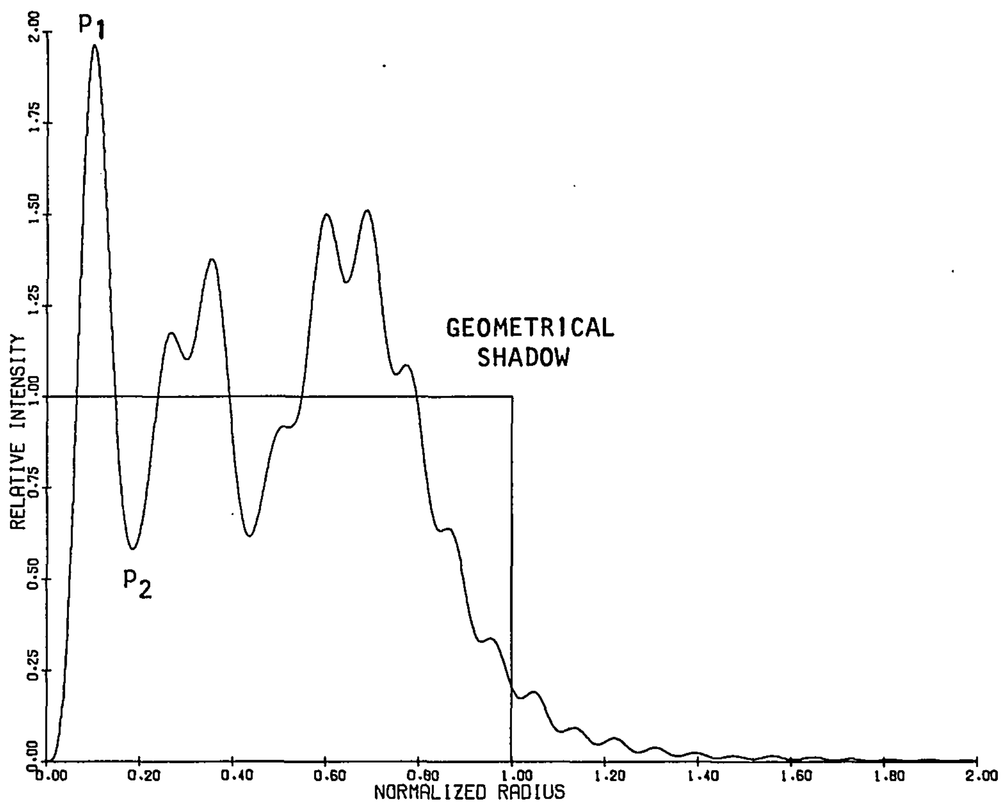

Figure 3.6. Diffraction Pattern for a Circular Aperture at Fresnel Number of 6.

previous change because a positive contribution is lost from Zone 5 and a negative contribution is acquired from Zone 8. The upper right pattern in Fig. 3.5 corresponds to the minimum at point p_2 at a radius 0.2 in Fig. 3.6.

Modulation in the vicinity of the geometrical shadow shows modulation at a higher frequency. At the edge of the aperture the integral of Eq. (3.29) has the graphical representation shown at the bottom of Fig. 3.5. Only the left side contributes a modulation term at a frequency f = 12. Measured from Fig. 3.6 the frequency is approximately f = 11.6. The magnitude of this modulation is related to the area of Zone 24 passed by the left side of the aperture, which is small with respect to the area of Zone 1.

The minimum sampling frequency for center detail in the circular aperture is

$$f = \frac{F}{a} . \tag{3.33}$$

In matrix units the maximum frequency is ½. The requirement of Eq. (3.33) becomes

$$a \geq 2F. \tag{3.34}$$

For detail at the region of the geometrical shadow

$$f = 2\frac{F}{a} . \tag{3.35}$$

Sampling at f = F/a is shown in Fig. 3.7 while sampling at f = 2 F/a is shown in Fig. 3.8. The points designated by x's were calculated with a 64 x 64 complex array using the near field routines from

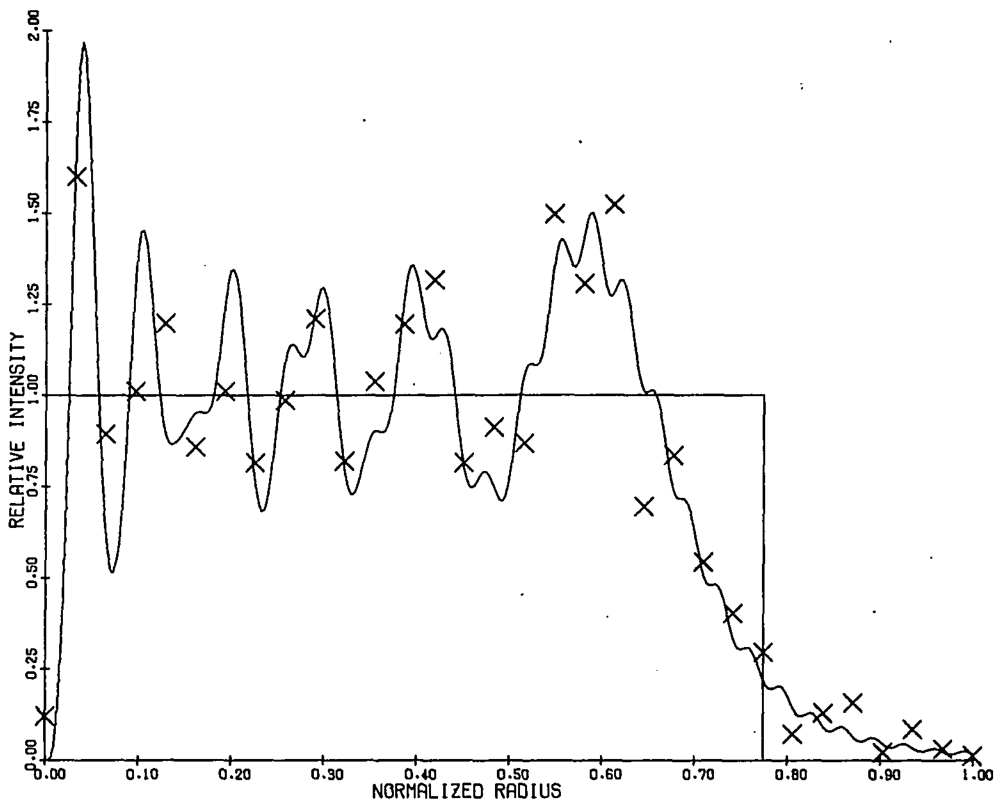

Figure 3.7. Sampling Errors for an Aperture Radius of 24 and a Fresnel Number of 12.

The x's represent the 64 x 64 matrix calculations. The solid line is the exact function.

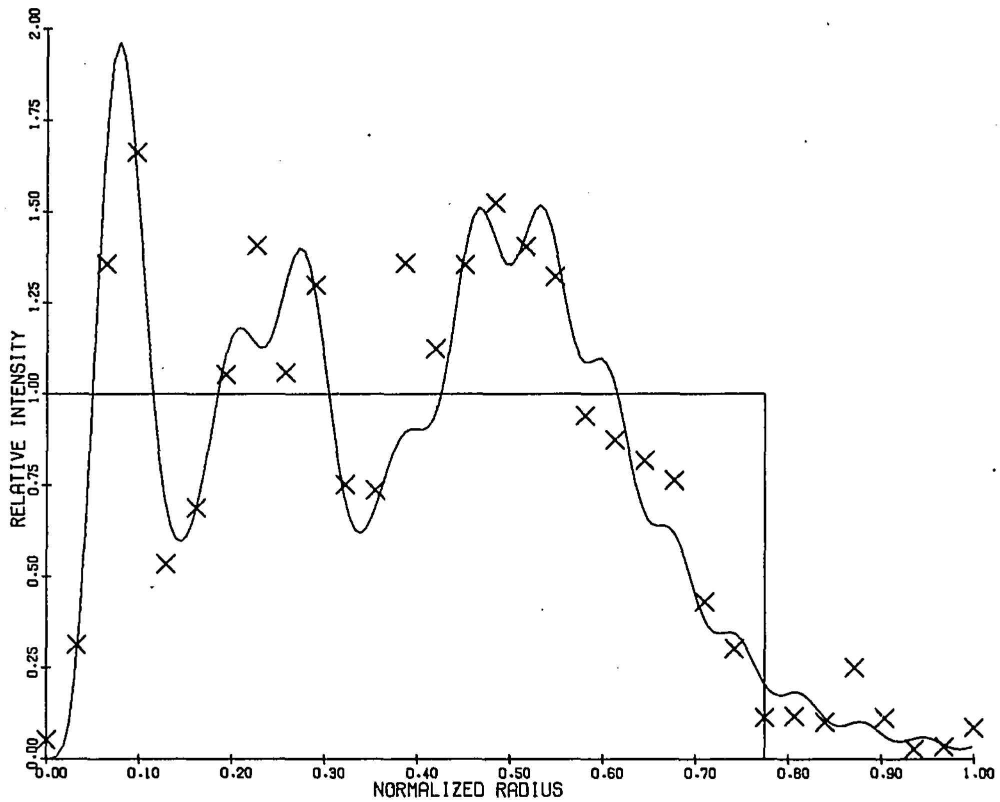

Figure 3.8. Sampling Errors for an Aperture Radius of 24 and a Fresnel Number of 6.

The x's represent the 64 x 64 matrix calculations. The solid line is the exact function.

LOTS. The solid curve was calculated using an effective matrix size of 4096 x 4096 by means of the central slice theorem,

$$F(\xi,0) = \int_{-\infty}^{\infty}\left[\int_{-\infty}^{\infty} f(x,y)\,dy\right] e^{j2\pi\xi x}dx, \tag{3.36}$$

so that only a one-dimensional transform is needed. Figure 3.7 shows the central detail roughly represented, but the finer detail is lost. Figure 3.8 at half the Fresnel number shows the center detail well but does not show the fine structure significantly better in spite of the fact that the sampling rate is adequate. This is because of errors due to spatial and frequency domain aliasing.

Energy spillover at the edge of the matrix causes spatial domain aliasing. An approximation of the normalized circular diffraction pattern which is accurate at a distance of a/F beyond the geometrical shadow is derived in Appendix C

$$I(a,r) \approx \frac{1}{\pi^2 F}\frac{(a/r)^3}{[1-(a/r)^2]^2}\,. \tag{3.37}$$

This expression represents approximately the envelope of the diffraction pattern.

Numerical techniques using the DFT treat the matrix as if it were one element of an infinite series as depicted in Fig. 3.9. The principal matrix is surrounded by an infinite array of similar cells, five of which are also shown in Fig. 3.9. At the edge of the principal cell a point, Q, has an aliased contribution principally from cell 3. At an interior point such as P the net contribution of cells 1, 2, 4, and 5 may exceed the contribution of cell 3. Equation (3.37) applied

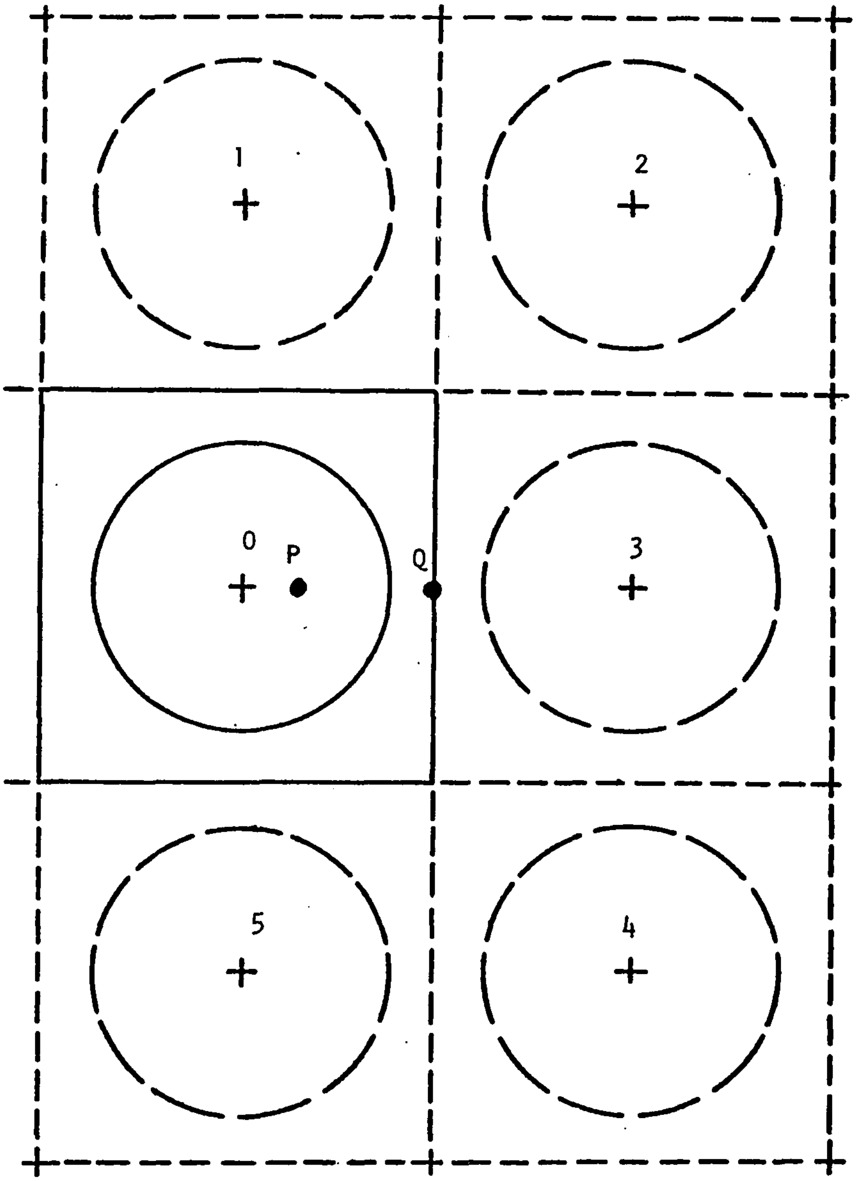

Figure 3.9. The Principal Cell and Several Ghost Cells that Contribute to Aliasing.

The principal cell 0 sits among an infinite array of ghost cells, five of which are shown.

to cell 3 will therefore give an optimistic answer for an interior point such as P.

To illustrate spatial domain aliasing consider near field diffraction at a Fresnel number of 4 with a 64 x 64 matrix. Table 3.2 shows values at the edge of the matrix, r = 32, for several values of aperture radius.

Table 3.2. Intensity at the Edge of the Matrix for Different Aperture Radii

Aperture radius	Edge normalized intensity
24	7.3×10^{-2}
18	1.1×10^{-2}
12	2.0×10^{-3}

In Fig. 3.10 the aliasing errors at the edge of the matrix (normalized radius of 1.0) are evident. The smooth curve in Fig. 3.10 was calculated from an effective matrix size of 4096 x 4096. The envelope of the pattern outside the geometrical shadow is in agreement with Eq. (3.36). Reducing the aperture radius to 18 while maintaining the Fresnel number at 4 yields the function shown in Fig. 3.11. The aliasing at the edge of the aperture is much reduced. Figure 3.12 shows an even further reduction of aliasing in the geometrical shadow. Both Figs. 3.11 and 3.12 still exhibit errors of intensity, some of which are of the order of 0.1.

Some of the residual error may be accounted for by frequency domain aliasing. For the uniformly illuminated circular aperture the

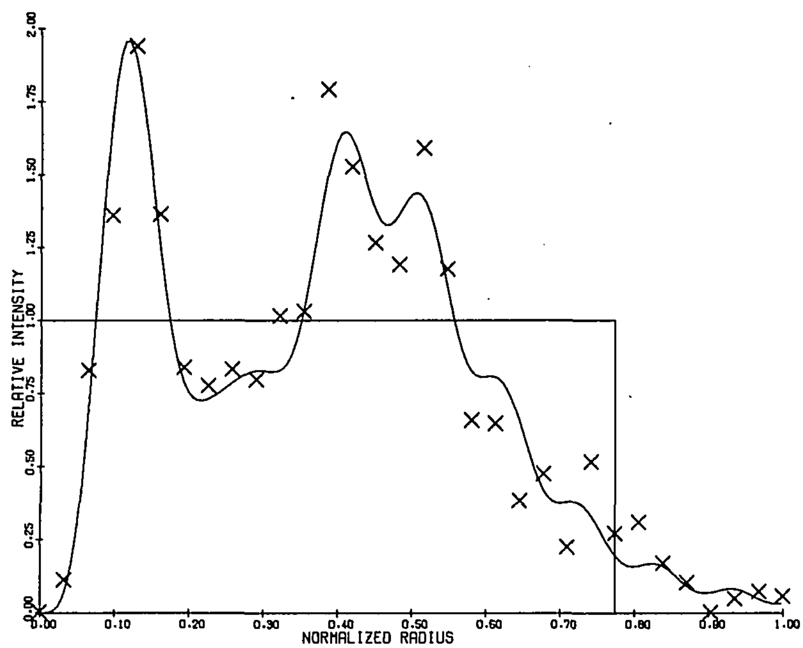

Figure 3.10. Diffraction Calculations for a Fresnel Number of 4 and an Aperture Radius of 24.

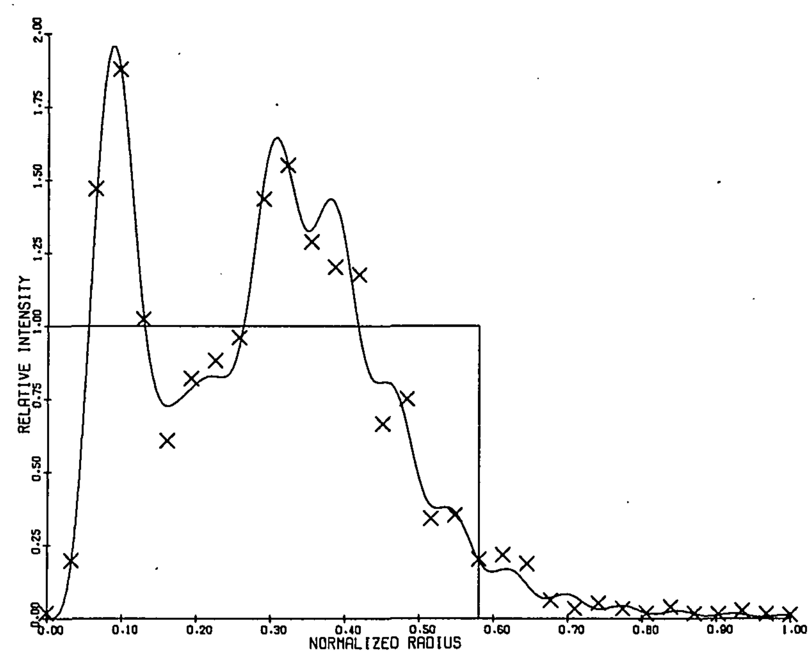

Figure 3.11. Diffraction Calculations for a Fresnel Number of 4 and an Aperture Radius of 18.

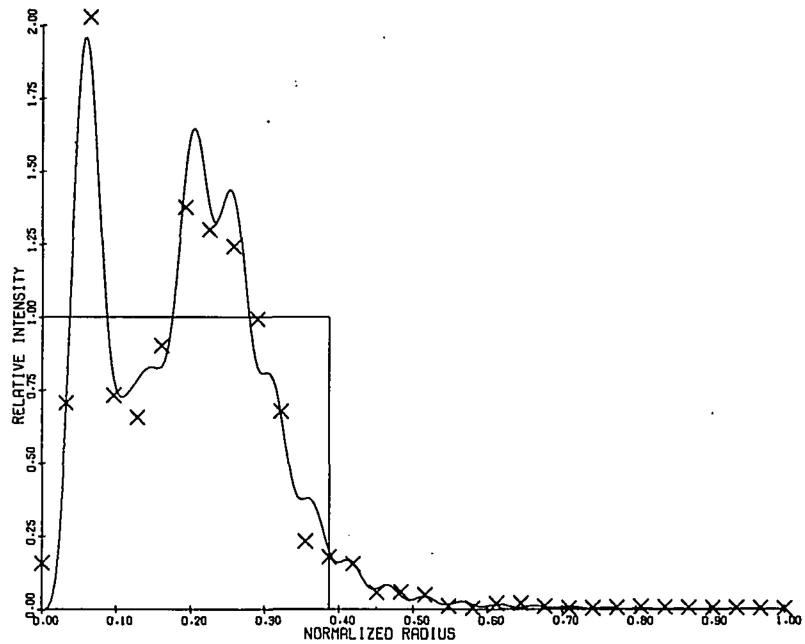

Figure 3.12. Diffraction Calculations for a Fresnel Number of 4 and an Aperture Radius of 12.

energy in the frequency domain outside a frequency radius ρ is given by the excluded energy equation for the Airy pattern (Born and Wolf, 1959, p. 443),

$$E(a,\rho) = J_0^2(2\pi a\rho) + J_1^2(2\pi a\rho). \tag{3.38}$$

This may be approximated after the first dark ring by the Bessel function approximation discussed in Appendix C by

$$E(a,\rho) = \frac{1}{\pi^2 a\rho}. \tag{3.39}$$

In matrix units the edge of the frequency matrix is at ½. This excluded energy is

$$E(a,\tfrac{1}{2}) = \frac{2}{\pi^2 a} \simeq \frac{1}{5a}. \tag{3.40}$$

For apertures of radius = 20 about 1% of the energy contributes to spurious phenomena in the spatial domain.

CHAPTER 4

NONLINEAR GAIN AND ABSORPTION

The effects of the laser amplifying media and the saturable absorbers are included, not primarily to determine the final energy of the laser fusion system, but rather because these effects must be included to do studies involving trade-off between laser wavefront quality and energy and because the energy density distribution is changed by nonlinear gain. Altering the energy density distribution changes the image distribution both directly and indirectly. The indirect effect occurs because the significance of phase errors at specific points in the aperture is determined by the strength of the energy density distribution at that point.

A measure of aberration which takes into account a variable energy density distribution is the generalized Strehl ratio

$$\text{Strehl ratio} = \frac{\iint_{-\infty}^{\infty} A(x,y)\,dxdy}{\iint_{-\infty}^{\infty} |A(x,y)|\,dxdy} \; . \tag{4.1}$$

In the case of uniform illumination this reduces to the usual expression (Born and Wolf, 1959) where $\theta(x,y)$ represents the aberration and S denotes integration over the aperture

$$\text{Strehl ratio} = \left[\frac{\iint_S e^{i\theta(x,y)} dxdy}{\iint_S dxdy} \right]^2 . \tag{4.2}$$

Equation (4.2) is often approximated for small aberration values as

$$\text{Strehl ratio} = 1 - \frac{2\pi}{\lambda}^{2} \sigma^2 , \tag{4.3}$$

where σ is the wavefront variance. Equation (4.1) and Eq. (4.2) are not approximations and may be used for any degree of aberration.

Figure 4.1 shows results typical of highly saturated gain. The skirts of the truncated Gaussian have had much higher gain than the center. Aberration at the outer part of the aperture will be of greater consequence after saturation.

Rate Equation Approximation

The theory of the laser amplifiers used in the Los Alamos CO_2 laser fusion program is based on the rate equation approximation. The requirements for this approximation are that (Sargent, Scully, and Lamb, 1974)

$$T_2 < \tau < T_1 ,$$

where T_2 is the dephasing time, τ is the pulse length, and T_1 is the level decay time. Coherence effects may be ignored when the dephasing time is less than the pulse length.

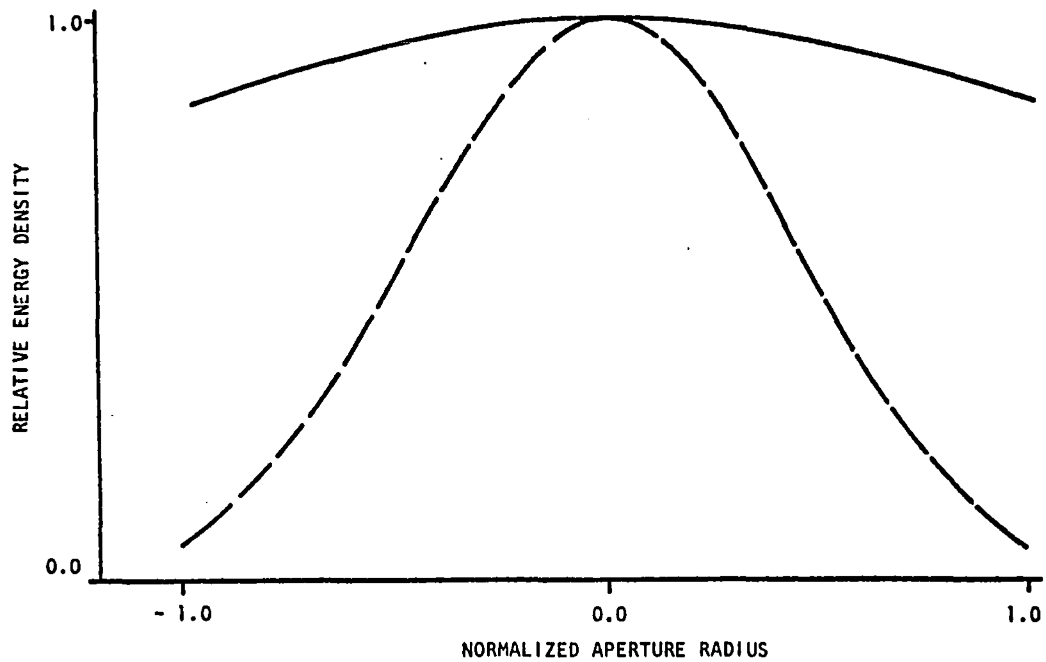

Figure 4.1. Effect of Saturated Gain on a Gaussian Distribution.

The dashed curve represents a truncated Gaussian input to the Helios power amplifier. The solid curve shows the resulting normalized energy density profile.

Figueira et al. (1973) showed the validity of the approximation for the 10.6 μm amplifiers used in the laser fusion systems for laser pulses of 5 ns duration with rotational relaxation times of about 0.2 ns. Stark et al. (1973) claimed that the agreement in energy extraction between the full density matrix approach and the rate equation approach was better than 1%.

In an early treatment of amplifier theory, Frantz and Nodvick (1963) used the photon transport equation

$$\left(\frac{\partial}{\partial t} + c\,\frac{\partial}{\partial z}\right) n(z,t) \;=\; \sigma c \Delta(z,t) n(z,t), \tag{4.1}$$

where $n(x,t)$ is the photon density, $\Delta(x,t)$ is the inversion density, σ is the resonance cross section and c is the speed of light in the medium and a second equation describing the effect of the radiation field on the inversion density

$$\frac{\partial \Delta(z,t)}{\partial t} \;=\; -2\sigma c n(z,t)\Delta(z,t). \tag{4.2}$$

Equations (4.4) and (4.5) may be solved simultaneously (Sargent et al., 1974) to yield an expression for $E(z)$, the energy density, in the laser pulse. It is convenient to write this expression in terms of g_0, the small signal gain, and E_s, the saturation energy

$$\frac{dE(z)}{dz} \;=\; -g_0 E_s\left[\exp\left(-\frac{E}{E_s}\right) - 1\right] \tag{4.3}$$

where

$$g_0 \;=\; \Delta(z,0)\sigma$$

$$E_s = \frac{\hbar\omega}{2\sigma}$$

$$E(z) = \int_{-\infty}^{\infty} c\hbar\omega n(z,t)\,dt.$$

Ignoring the pulse shape and using the energy density description reduces the three-dimensional distribution of the pulse to a two-dimensional one.

Equation (4.6) was found analytically to be valid by Schappert (1973) for 1 to 2 ns pulses, provided E_s was suitably adjusted. Experimental verification was provided by Stark et al. (1973).

Equation (4.6) has the closed form solution

$$E_f = E_s\left\{\ln \exp(g_0 L)\left[\exp\left(\frac{E_i}{E_s}\right) - 1\right] + 1\right\} \tag{4.7}$$

where E_i and E_f are the initial and final energy densities respectively and L is the length of the amplifying medium.

Equation (4.6) is valid only for essentially collimated beams. To treat beams which are noncollimated use is made of a generalization of Eq. (4.4) by Avizonis and Grotbeck (1966) to include a loss term, α, such that

$$\left(\frac{\partial}{\partial t} + c\,\frac{\partial}{\partial z}\right) n(z,t) = \sigma c\Delta(z,t)n(z,t) - \alpha c n(z,t). \tag{4.8}$$

Solving Eqs. (4.8) and (4.5) simultaneously gives the more general result

$$\frac{dE(z)}{dz} = -g_0 E_s\left[\exp\left(-\frac{E}{E_s}\right) - 1\right] - \alpha E(z). \tag{4.9}$$

Noncollimated beams may be treated by setting the loss coefficient equal to the energy density change due to the geometrical divergence or convergence of the beam

$$\frac{dE(z)}{dz} = -g_0 E_s \left[\exp\left(-\frac{E}{E_s}\right) - 1\right] - \frac{2E(z)}{z + z_0}, \qquad (4.10)$$

where z_0 is the initial wavefront radius. If g_0 is zero, the relationship for energy density expected from the geometrical theory is obtained

$$\frac{E_f}{E_i} = \left(\frac{z_0}{z + z_0}\right)^2. \qquad (4.11)$$

In LOTS Eq. (4.10) is solved by a Runga-Kutta technique for each point in the matrix for noncollimated beams. For collimated beams Eq. (4.7) is used.

The above amplifier theory neglects the effects of diffraction. Diffraction effects may be approximately included by applying the gain equations (4.7) or (4.10) and the Fresnel diffraction operation sequentially. More accurately the amplifier length may be subdivided and the amplifier and diffraction operations applied to each segment. The quality of the calculation improves with an increase in the number of subdivisions. In the main power amplifier of the laser fusion systems the Fresnel number is large and little or no subdivision may be necessary. A guide to subdivision is to choose the subdivision propagation distance based on the sampling consideration discussed in Chapter 4. Expressed in the effective propagation distance, Z_{eff},

$$Z_{eff} < \frac{2aT}{\lambda} \tag{4.12}$$

where

a = aperture radius

T = sampling interval

$Z_{eff} = (Z_2 - Z_1)(Z_1/Z_2)$

Z_1 = initial wavefront radius

Z_2 = final wavefront radius.

The above theory is designed to handle a single vibrational line. Multiple lines may be treated approximately by modifying g_0 and E_s.

Saturable Absorbers

Saturable absorbers are used in the CO_2 laser fusion system to reduce the small signal gain of the amplifiers while having the strong signal gain essentially unchanged. This nonlinear transmission helps to prevent the amplifier from prepulsing (Montgomery et al., 1978). If the saturable absorber is sufficiently fast, protection against pulses retroreflected at the laser fusion target will also be achieved. Fast response materials are also used for temporal pulse shaping (Phipps and Thomas, 1977). Some of the saturable absorber materials used, or proposed for use, are shown in Table 4.1.

In the case of a material acting like a two-level system if $\tau < T_1$, the concept of a saturation energy density is appropriate, if $\tau > T_1$ a saturation irradiance applies (Schappert and Stark, 1974).

Table 4.1. Representative Saturable Absorber Materials.

P-doped germanium	(Phipps and Thomas, 1977)
SF_6	(Czuchlewski et al., 1978)
NH_2D	(Schappert and Stark, 1974)
KR_eO_4 doped KCl	(Ahrenkiel et al., 1978)

In the latter case the transmission takes the form (Phipps and Thomas, 1977)

$$T_r(i) = \exp\left\{\frac{g_0 L}{[1 + (I/I_s)]q}\right\} \tag{4.13}$$

where

g_0 = small signal gain (or loss)

L = media length

I = incident irradiance

I_s = saturation irradiance

q = 1 for homogeneous broadening

½ for inhomogeneous broadening.

The energy density transmission function is dependent on the pulse shape. However, for a given pulse shape, Eq. (4.13) may be integrated numerically or experiments may be done with the medium and pulse shape of interest to get an energy density transmission function.

In the case of a two-level system with $\tau < T_1$, the Frantz-Nodvick theory applies with a negative gain coefficient. Unfortunately one of the principal materials, SF_6, has a long relaxation time but does not act like a two-level system (Hopf and Scully, 1970). Because of the influence of many levels, there is no well defined saturation energy and SF_6 bleaches less sharply with increasing energy than would be expected from the two-level theory.

In the absence of concise theoretical descriptions in terms of transmission of energy density, LOTS was designed to include saturable absorber effects by means of curve fitting to experimental data. It was noted that for most saturable absorber materials a plot of log transmission versus log energy density looks "S" shaped as shown in Fig. 4.2. This type of curve can be described in terms of four parameters: maximum transmission, TMAX; minimum transmission, TMIN; the energy density of saturation, ES; and the slope, S. ES is measured at the average log transmission value ½(log TMAX + log TMIN). The slope of log transmission versus log energy density is measured at the same point. An equation which yields an "S" shape with these four parameters is

$$\log T_r = (\log \mathrm{TMAX} - \log \mathrm{TMIN})$$

$$\times \left[1 - \frac{1}{\exp 4S \dfrac{\log E - \log \mathrm{ES}}{\log \mathrm{TMAX} - \log \mathrm{TMIN}}} \right] + \log \mathrm{TMIN}.$$

This equation fits the saturation forms of Eq. (4.13) and (4.7) nicely and fits experimental data well as shown in Fig. 4.3. The principal error occurs at low transmission values where it has no consequential effect on the laser pulse whose typical peak energy density is at least two orders of magnitude higher than this region.

This approach offers sufficient flexibility to accommodate forseeable saturable absorbers. It could also be used to treat gain media that did not fit Eq. (4.7).

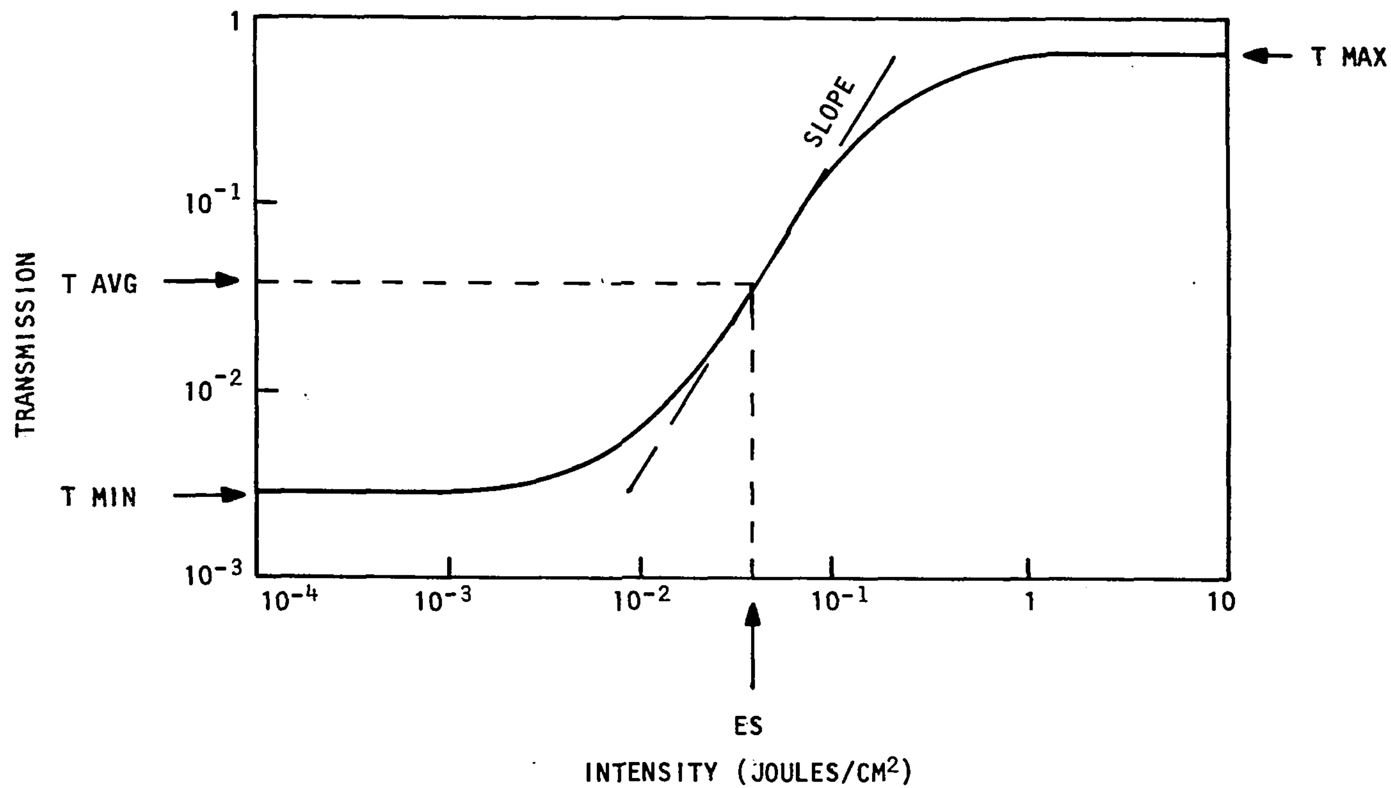

Figure 4.2. Plot of Log Transmission against Log Energy Density for an Idealized Saturable Absorber.

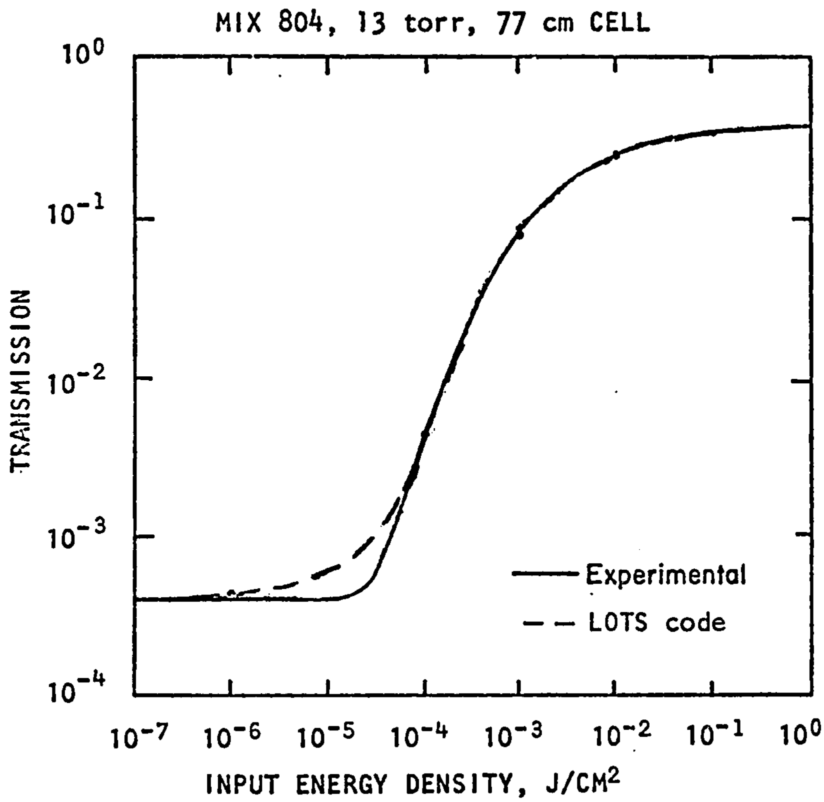

Figure 4.3. Saturable Absorber Experimental Data and LOTS Curve Fit Data.

CHAPTER 5

ABERRATION

In conventional optical systems, the focus of attention is on calculating and reducing the aberration of components independently of manufacturing errors. This type of aberration is referred to in this discussion as ideal component aberration. There is generally an attempt in the design of conventional systems to correct aberration by introducing aberration of opposite sign. Subtraction of nearly identical aberration contributions at different surfaces requires very accurate calculations. In these systems, manufacturing errors are generally considered after the principal design in separate, tolerancing calculations.

In contrast the emphasis in laser fusion systems is on manufacturing error. Because of the large F-numbers and zero field angles which characterize these systems, ideal component error is essentially negligible. The final focusing mirrors are reasonably fast but they are paraboloids working at infinite conjugates and are ideally aberration free on axis. Because of the large number of surfaces in the optical train, the cumulative effect of manufacturing error is quite significant. Since no correction by aberration subtraction is involved, accuracy of a few percent is sufficient. Where it is necessary to include ideal component aberration, the best method is to analyze the system on a ray trace program such as ACCOS. What aberration exists will be predominantly low order because of the small incidence angles on the surfaces with power. Values of the Seidel aberrations obtained in this fashion may be entered into LOTS.

Ideally all component aberrations would be determined from interferometric measurements on the finished component. However, in the early stages of the design, only the specification of the components will be available. Indeed, one of the primary uses of LOTS is to do studies of performance for different component specifications. Even in a completed system it may be sufficient to describe the less critical components--those in the front of the system--by their specification values.

Interferometric Data

Interferograms are generally available on the critical components in the LASL laser fusion systems. In order to be applied to pulse propagation these data must be transformed into phase errors at the matrix points.

Data reduction of interferograms is a complex task and requires a specialized program such as FRINGE (Loomis, 1978). At Los Alamos, interferograms are routinely reduced to determine statistical properties of the component. As an option, FRINGE will fit a set of Zernike polynomial coefficients to the wavefront (Viswanathan, Hayden, and Liberman, 1979). Zernike coefficients allow the radius of the component to be scaled easily. These coefficients may be entered into LOTS to reproduce the wavefront. Figure 5.1 shows an original interferogram and a computer-generated interferogram made by LOTS. The interferogram was

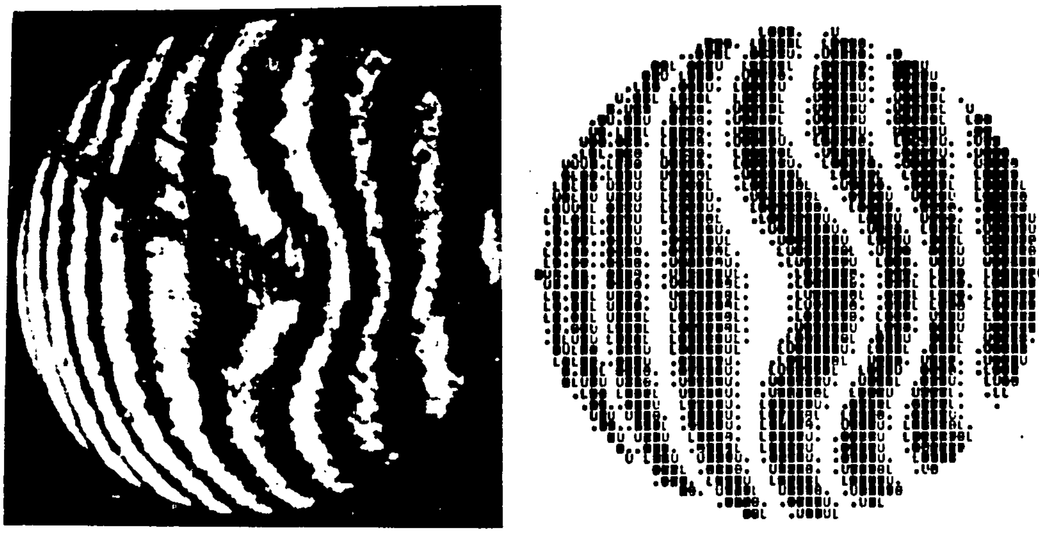

Original Interferogram LOTS Interferogram

Figure 5.1. Original and LOTS Interferograms Compared.

The original interferogram was data reduced with FRINGE and then reproduced by LOTS on a line printer from polynomial coefficients. Contrast is reversed in the computer-generated interferogram.

first digitized and then reduced by FRINGE to get the Zernike coefficients. The finite number of digitization points--typically 20 points across the diameter--and the finite number of polynomial coefficients introduce some smoothing to the data. To allow other means of data reduction, LOTS will read in a 64 x 64 complex array created by the user and multiply this array with the existing complex amplitude distribution. Provision is made for scaling this array by linear interpolation.

Even in the absence of polynomial coefficient fitting errors, the discrete nature of the matrix points will cause poor modeling of rapidly varying phase errors. Arguments similar to those used in Chapter 3 for diffraction calculations may be applied to this problem as well. In general, cyclical variations with period shorter than two matrix point separations will not be well represented. Polished surfaces will usually not have rapid phase variations because of the comparatively large size of the polishing tool. Diamond point turned surfaces show significant fine tool marks although this process has shown enormous improvement. The high spatial frequency of these tool marks cause their primary effect to be scattering of light well outside the central core of the image. This scattered light will be blocked by subsequent spatial filters. In the case of optics after the last spatial filter the scattered light will completely miss the target. In either case the effects of the scattered light may be approximately represented as a transmission loss.

Random Wavefronts

In general, in the design phase the aberration of components will be defined in terms of peak-to-valley or RMS wavefront error. The effects of aberrated components known only by their specification values may be included in beam propagation calculations by adding smoothed random wavefronts having the same specification values. These wavefronts should not only have the same peak-to-valley or RMS error but the same characteristic types of aberration value as well. In LOTS the autocorrelation function width is used to control the aberration type. Loosely defined, the autocorrelation function width is the locus of distances from a given point for which the phase is essentially the same. Proper autocorrelation widths are particularly important for the "energy-in-a-bucket" criterion commonly used at Los Alamos. This criterion specifies the radius encircling 80% of the energy in the image. Figure 5.2 is a plot of the encircled energy function, E(r),

$$E(r) = \int_0^r \int_0^{2\pi} |A(r,\theta)|^2 d\theta d\rho \qquad (5.1)$$

where $A(r,\theta)$ is the complex amplitude distribution defined in polar coordinates, is shown for two wavefronts differing by a factor of two in autocorrelation width. In both cases the peak-to-valley error was one wavelength. The large autocorrelation width was 75% of the aperture radius and the small autocorrelation width was 37.5% of the aperture radius. For this example the encircled energy radius at the 80% point is 20% larger for the small autocorrelation radius.

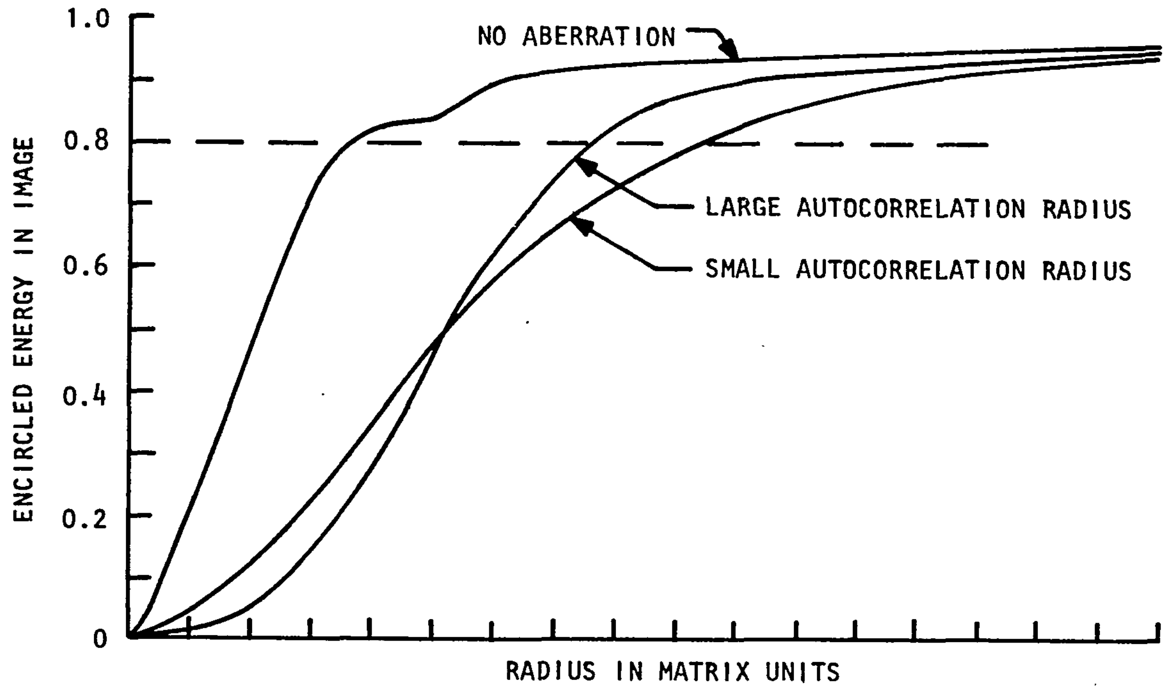

Figure 5.2. The Encircled Energy in the Image as Influenced by the Autocorrelation Radius.

With a clear aperture of 8 units and random aberration of peak-to-valley error 1 wavelength, autocorrelation radii of 6 (large) and 3 (small) are compared. The radius encircling 80% of the energy is a common criterion.

The characteristic types of aberration present in a component is, of course, determined by the manufacturing process. Optics which are fabricated on rotating machinery will, in general, have a tendency toward rotationally symmetric wavefront error, i.e. zones. Figure 5.3 shows the form the autocorrelation function would be expected to take in this instance for P_1, the center of the optics, and for P_2 near the edge. As the piece is worked toward perfection by the optician, zonal characteristics, which are easiest to control, are removed leaving residual irregular errors. This situation is portrayed in Fig. 5.4. The autocorrelation width becomes more nearly constant for high quality polished parts.

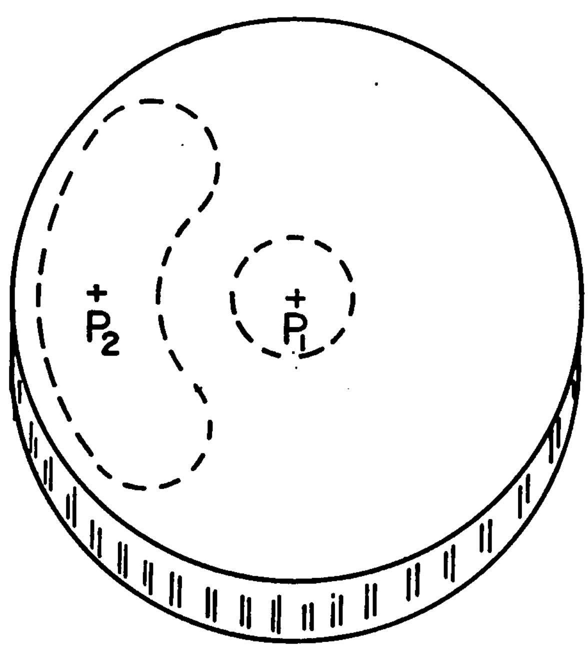

Figure 5.3. Variable Autocorrelation Size on the Surface of a Mirror at an Early Stage of Polishing.

The dotted lines represent approximately the bounds of the autocorrelation function for points P_1 and P_2.

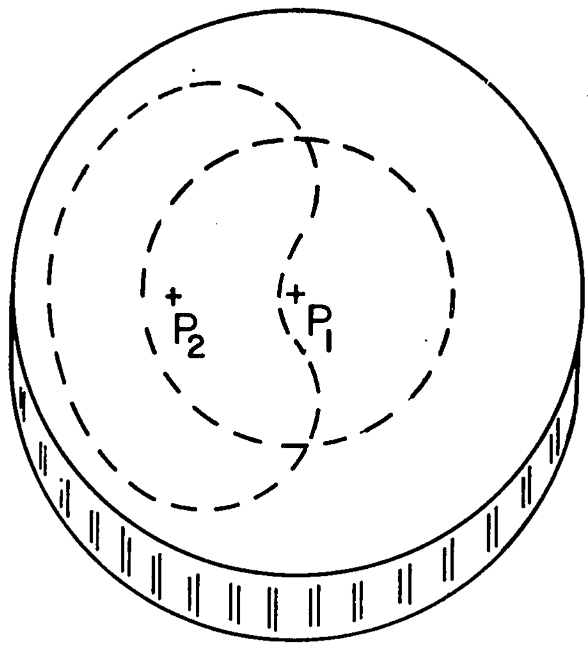

Figure 5.4. Nearly Constant Autocorrelation Size on the Surface of a Mirror at a Late Stage in Polishing.

The radial width of the autocorrelation function has grown faster than the azimuth width.

Diamond-turned optics may have a point of symmetry about some exterior point. Where possible, exact data from interferograms should be used for these components. However, in the absence of experimental data, the best assumption is that the autocorrelation width is constant.

Use of a constant autocorrelation function allows the random wavefronts to be created by a linear shift invariant process--a considerable simplification. Appendix D contains a detailed discussion of this process. Here it suffices to say that a delta-correlated function,

$G(x,y)$, is smoothed by an appropriate function, $s(x,y)$, by either convolution or weighting the frequency spectrum to yield a smoothed phase function $f(x,y)$. The complex amplitude, $A(x,y)$, is then modified by the phase errors,

$$A_1(x,y) = A_0(x,y)\exp[jf(x,y)]. \tag{5.2}$$

Figure 5.5 shows two wavefronts which were created from the same delta-correlated starting wavefront but were smoothed by different smoothing function widths. Gray tone pictures with eight shades of gray have been created by overstriking on a line printer. The wavefronts have the same peak-to-valley error. Figure 5.6 shows phase maps of the same wavefronts giving a clearer idea of the autocorrelation size.

Spatial Filters

Spatial filters serve a variety of purposes in the CO_2 laser fusion systems. Only the removal of aberration by the spatial filter is important for the LOTS system analyses. The configuration of a spatial filter is shown schematically in Fig. 5.7. The aberrated window (grossly exaggerated) introduces phase errors into the wavefront. Lens L1 of focal length, f_1, brings the light to a focus at the spatial filter which removes high spatial frequency components. Lens L2 of focal length, f_2, recollimates the beam.

The analysis of the effects of the two lenses in the absence of the spatial filter may be done using the concept of the effective propagation distance developed in Appendix A. The inital distribution $p_1(x,y)$ is transformed by the Lens L1,

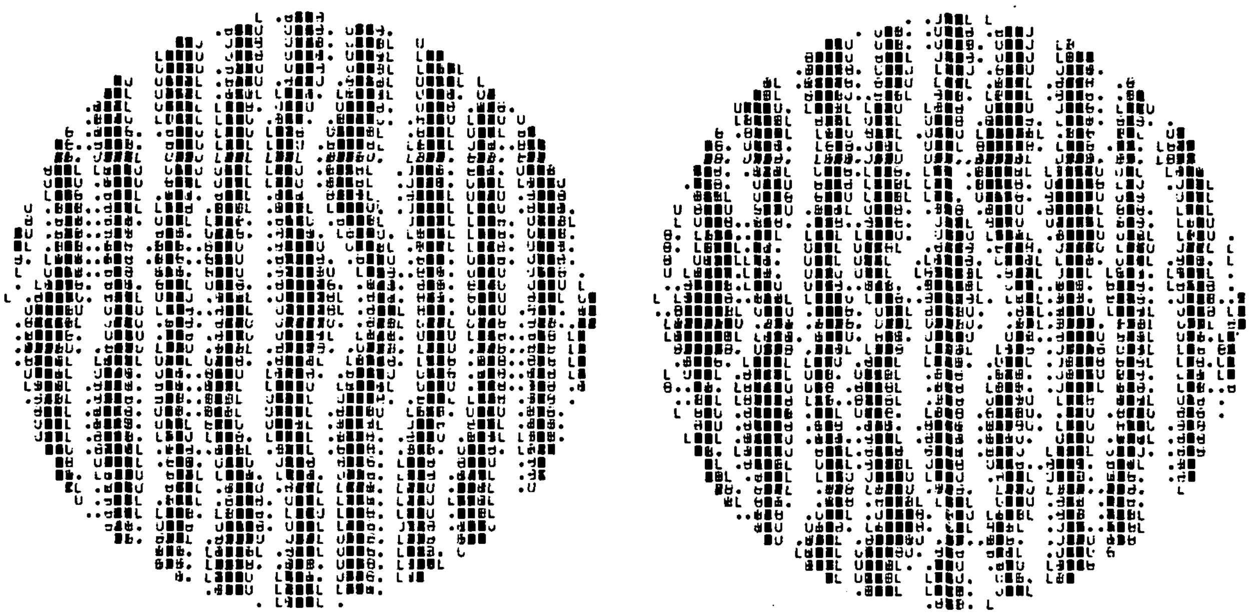

Figure 5.5. Interferograms of Wavefronts with Different Autocorrelation Widths.

The autocorrelation radius of the wavefront on the left is 20% and on the right is 10% of the aperture radius. The wavefronts have the same peak-to-valley wavefront error.

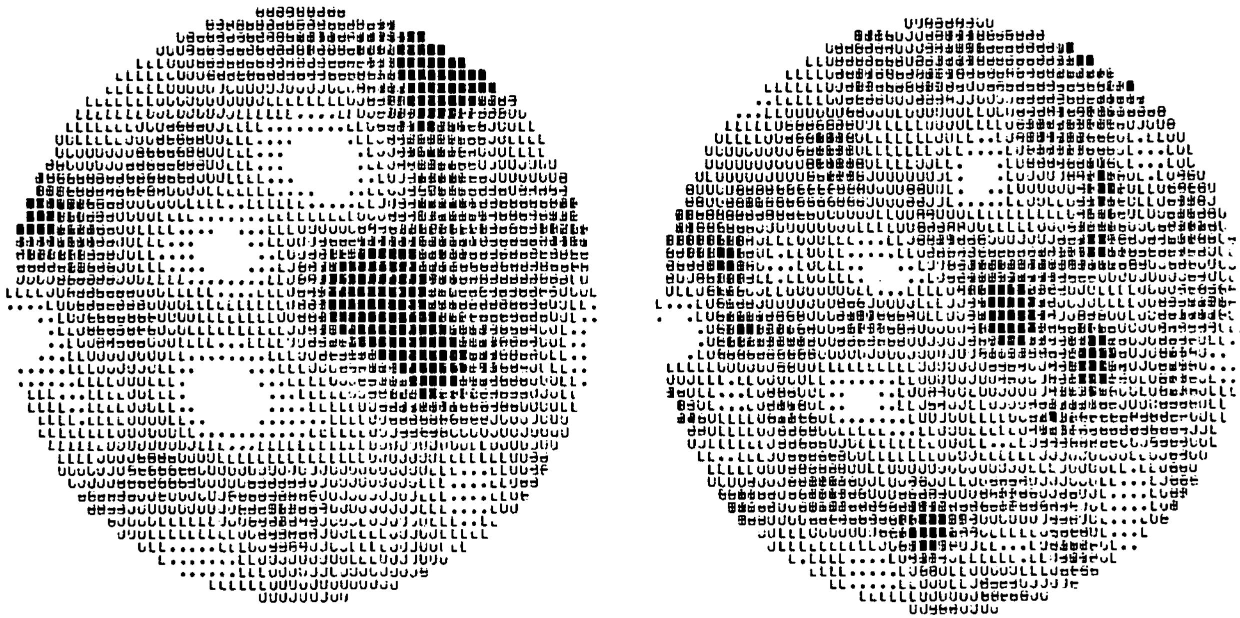

Figure 5.6. Phase Maps for the Wavefronts Shown in Fig. 5.5.

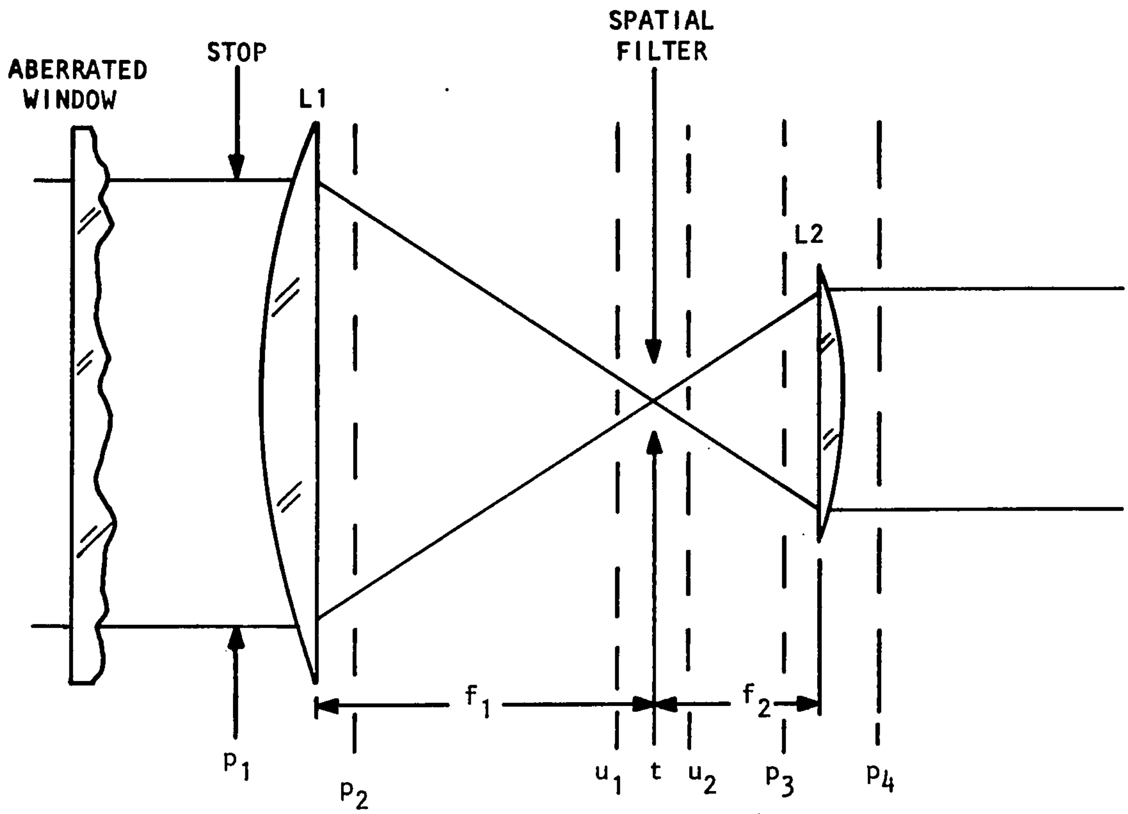

Figure 5.7. Schematic of Spatial Filter.

Figure 5.7. Schematic of Spatial Filter.

Planes p_1 and p_4 are the initial and final planes respectively. Planes u_1 and u_2 are actually coincident to the spatial filter plane t.

$$p_2(x,y) \;=\; p_1(x,y)\, \exp\left(-j\pi \frac{r^2}{\lambda f_1}\right) . \tag{5.3}$$

Similarly at lens L2,

$$p_4(x,y) \;=\; p_3(x,y)\, \exp\left(-j\pi \frac{r^2}{\lambda f_2}\right) . \tag{5.4}$$

At plane p_2 the distribution $f_2(x,y)$ may be defined such that

$$p_2(x,y) \;=\; g_2(x,y)\, \exp\left(-j\pi \frac{r^2}{\lambda f_1}\right) . \tag{5.5}$$

Similarly,

$$p_3(x,y) \;=\; g_3(x,y)\, \exp\left(j\pi \frac{r^2}{\lambda f_2}\right). \tag{5.6}$$

Using Eqs. (5.3) and (5.5) and Eqs. (5.4) and (5.6),

$$p_1(x,y) \;=\; g_2(x,y) \tag{5.7}$$

$$p_4(x,y) \;=\; g_3(x,y). \tag{5.8}$$

From Eq. (3.12) the relationship between $g_2(x,y)$ and $g_3(x,y)$ is obtained by substituting $z = -f$ and $z = f$,

$$g_3(x,y) \;=\; -\frac{f_1}{f_2}\, g_2\left(-\frac{f_1}{f_2}\, x,\; -\frac{f_1}{f_2}\, y\right) ** \frac{\exp\left[j\pi(r^2/\lambda z_e)\right]}{j\lambda z_e} \tag{5.9}$$

where

$$z_e \;=\; -\frac{f_1}{f_2}\,(f_2+f_1) \tag{5.10}$$

and ** represents two-dimensional convolution. The initial and final distributions $p_1(x,y)$ and $p_4(x,y)$ are related by

$$p_4(x,y) = -\frac{f_1}{f_2}\, p_1\left(-\frac{f_1}{f_2}\,x,\ -\frac{f_1}{f_2}\,y\right) ** \frac{\exp[j\pi(r^2/\lambda z_e)]}{j\lambda z_e}\,. \tag{5.11}$$

The distribution $P_1(x,y)$ is negated, inverted, and effectively propagated backward a distance $f_2 + f_2{}^2/f_1$. This analysis assumes that lens L2 does not limit the beam. In this case if the distribution is propagated forward by $f_2 + f_2{}^2/f_1$ beyond lens L2, the effects of propagation will be removed from $p_4(x,y)$. In the LOTS Manual (Lawrence, 1979) this is demonstrated in Example 13.

For the recollimating lens L2, Eq. (3.8) gives

$$p_4(x,y) = \frac{1}{j\lambda f_2}\, FF\left[u_2(x',y')\ \exp\left(j\pi\,\frac{r'^2}{\lambda f_2}\right)\right], \tag{5.12}$$

where primed coordinates are used at the image plane. If the spatial filter is described by the transmission function, $t(x,y)$,

$$u_2(x',y') = u_1(x',y')t(x',y'). \tag{5.13}$$

In the spatial frequency variable the transmission function is $t(\lambda f_2\xi,\lambda f_2\eta)$ and $p(x,y)$ with the spatial filter is

$$p_4(x,y) = \frac{1}{j\lambda f_2}\, FF\left[u_1(x',y')\ \exp\left(j\pi\,\frac{r'^2}{\lambda f_2}\right)\right] ** FF\left[t(\lambda f_2\xi,\lambda f_2\eta)\right]. \tag{5.14}$$

Equation (5.11) modified to include the spatial filter is

$$p_4(x,y) = -\frac{f_1}{f_2}\, p_1\left(-\frac{f_1}{f_2}\,x,\ -\frac{f_1}{f_2}\,y\right) ** \frac{\exp[j\pi(r^2/\lambda z_e)]}{j\lambda z_e} ** \frac{1}{\lambda^2 f_2{}^2}\, T\left(\frac{x}{\lambda f_2},\ \frac{y}{\lambda f_2}\right). \tag{5.15}$$

Equation (5.14) is the Fresnel diffraction description of the spatial filter.

In the case of a circular pinhole as a spatial filter $t(x',y') = \mathrm{cyl}(r'/2a)$, where "cyl" represents the cylinder function with radius, a (Gaskill, 1978). Then, using the "somb" function as defined by Gaskill (1978)

$$\frac{\pi}{4}\,(4a^2)\;\mathrm{somb}(2a\rho) \;=\; \mathrm{cyl}\left(\frac{r'}{2a}\right). \tag{5.16}$$

In the pupil plane this gives

$$\frac{1}{\lambda^2 f_2{}^2}\,T\left(\frac{x}{\lambda f_2},\,\frac{y}{\lambda f_2}\right) \;=\; \frac{\pi a^2}{\lambda^2 f_2{}^2}\left\{\frac{2J_1\left[2\pi(ar/\lambda f_2)\right]}{2\pi(ar/\lambda f_2)}\right\}. \tag{5.17}$$

In the limit as the radius of the spatial filter goes to infinity the expression in Eq. (5.17) becomes a delta function and no aberration is removed. But for decreasing spatial filter radius the Airy pattern of Eq. (5.17) smooths out the aberration in the wavefront.

Figure 5.8 shows the improvement in the Strehl ratio for spherical aberration, coma, and astigmatism as a function of spatial filter radius measured in multiples of the first Airy dark ring radius. The configuration for this calculation is the same as Fig. 5.7 with $f_1 = f_2$ and an aperture after the second lens of the same size as the stop in front of the lens.

In this calculation, the Zernike representation of the aberrations was used (Born and Wolf, 1959, p. 470) as shown in Table 5.1. To achieve a Strehl ratio of 0.8, Born and Wolf (1959, p. 470) give the following relation where ℓ, m, and n are the order of the field, aperture, and cosine dependence respectively

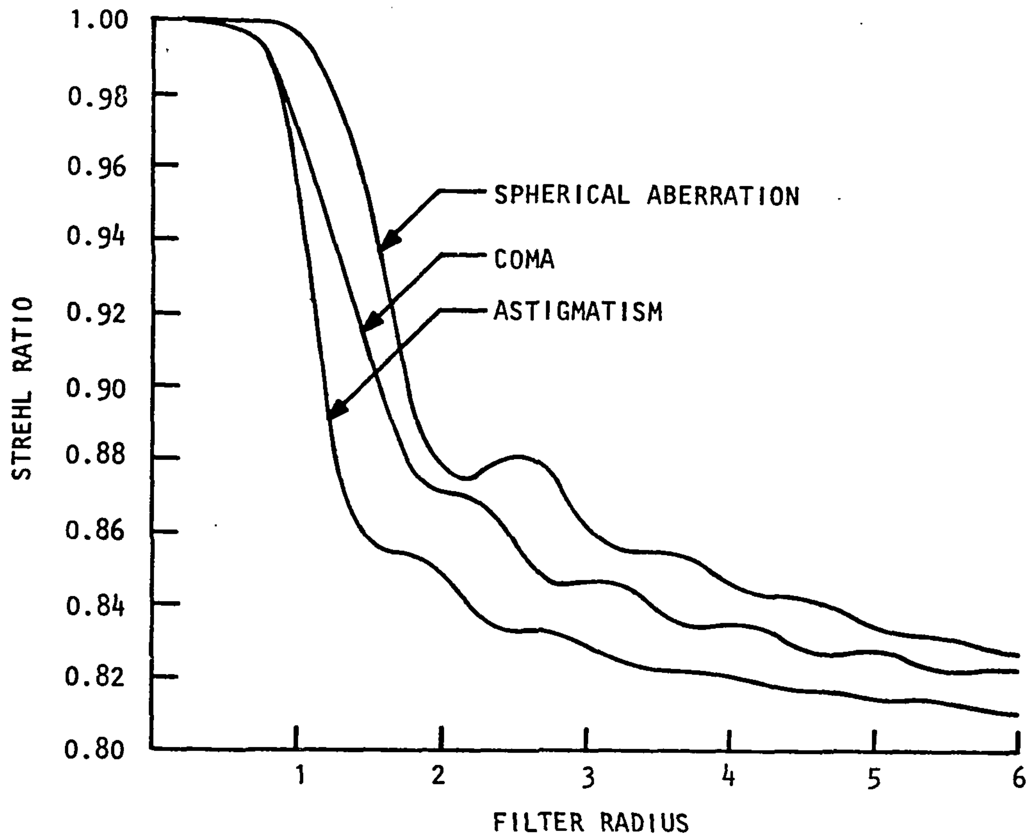

Figure 5.8. Change in Strehl Ratio for Spatial Filter Radii Measured in Multiples of the Radius of the First Dark Ring of the Airy Pattern.

Table 5.1. Zernike Aberration Forms

Spherical aberration	$\frac{A_{040}}{\sqrt{2}}(6\rho^4 - 6\rho^2 + 1)$
Coma	$A_{031}(3\rho^3 - 2\rho)\cos\theta$
Astigmatism	$A_{022}\rho^2(2\cos\theta - 1)$

$$\text{Strehl ratio} = 1 - \left(\frac{2\pi}{\lambda}\right)^2 \frac{A^2{}_{\ell nm}}{2(n+1)} = 0.8. \tag{5.18}$$

A more accurate approximation mentioned by Loomis (1976) is

$$\text{Strehl ratio} = \exp\left[- \left(\frac{2\pi}{\lambda}\right)^2 \frac{A^2{}_{\ell mn}}{1(n+1)}\right] = 0.8. \tag{5.19}$$

Using Eq. (5.19), the coefficient of the Zernike polynomials may be computed and transformed into the Seidel forms for entry into LOTS as shown in Table 5.2.

Table 5.2. Seidel Aberrations to Achieve Strehl Ratio = 0.8.

Aberration	Strehl ratio CLAP = 30	Strehl ratio CLAP = 7.808
SPH = 0.95493, FOCUS = 0.95493	0.80036	0.81605
COMA = 0.60395, TILT = 0.40263	0.79921	0.81568
AST = 0.34869, FOCUS = 0.17435	0.80252	0.80870

The computed Strehl ratio at a clear aperture radius of 30 is in agreement with Eq. (5.19). At a clear aperture radius of 7.808 some inaccuracy due to sampling is present. This clear aperture gives a radius of the first dark ring in the Airy pattern of 5 matrix units by Eq. (5.20) for convenience. The far field interval is $\Delta x = \lambda z/NT$.

$$1.22\left(\frac{\lambda z}{2a}\right)\left(\frac{NT}{\lambda z}\right)\bigg|_{a\,=\,7.808} = 5\ . \tag{5.20}$$

At a spatial filter radius of 1.5 Airy dark rings most of the spherical aberration, about half of the coma, and very little of the astigmatism is removed. Aberration removal by the spatial filter correlates approximately with the radial dependence of the aberration in the pupil plane. If the Seidel forms are used, this simple radial dependence is lost. Coma, for example, is harder to remove than astigmatism in this case because of the inherent tilt component in the Seidel form of coma.

Figure 5.9 shows interferograms before and after a spatial filter. The trapezoidal aperture is typical of the Antares system. These data are taken from Example 23 in the LOTS Manual, which gives full details of the calculation. The interferogram on the left represents a wavefront having a Strehl ratio of 0.435. After the spatial filter and truncation by an aperture of the same shape as the original, the Strehl ratio is raised to 0.668. This increase in Strehl ratio was achieved at the cost of a 39% loss in energy at the spatial filter. The interferogram on the right shows much straighter fringes. The variation in contrast reflects a variation in intensity introduced by the spatial filter.

Paraxial versus Gaussian Focus

It is well known that the best focus position for a laser beam of Gaussian intensity distribution will not in general coincide with the

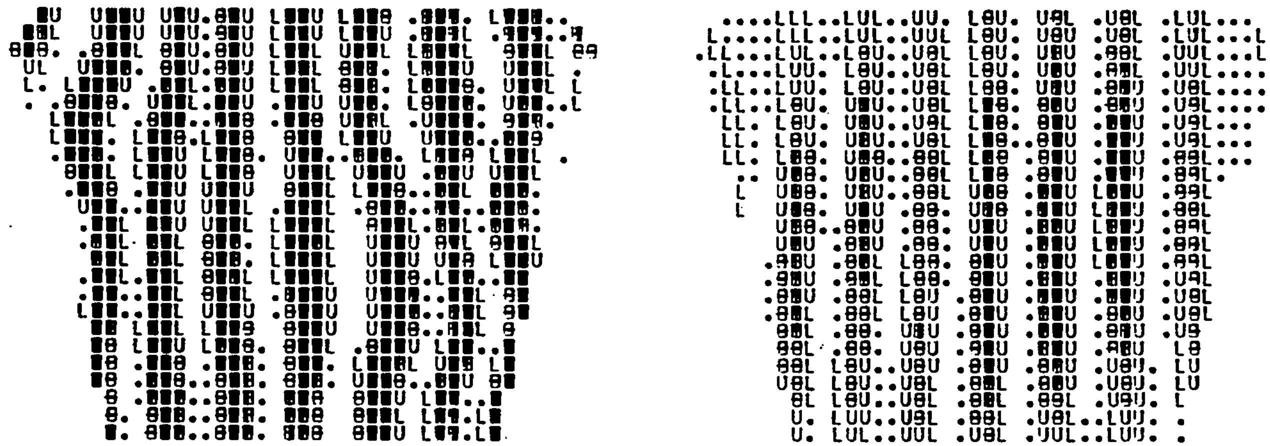

Figure 5.9. Interferograms before and after a Spatial Filter.

The interferogram on the left shows a wavefront before the spatial filter. The interferogram on the right shows the effects of aberration removal by the spatial filter.

paraxial focal plane of a lens. The intensity distribution in the front end of the laser systems is nearly Gaussian. From Dickson (1970) the separation between the Gaussian image waist and the paraxial focus for a beam with Gaussian waist at the lens is

$$\frac{\Delta f}{f} = \frac{-1}{1 + (\pi r_0{}^2/\lambda f)^2} \approx -\left(\frac{\lambda f}{\pi r_0{}^2}\right)^2 , \tag{5.21}$$

where f is the focal length of the lens and r_0 is the Gaussian waist radius at the lens.

The focus error in the pupil plane is

$$\frac{W}{\lambda} \approx \frac{1}{2}\frac{r_0{}^2}{f^2}\,\Delta f \approx -\frac{1}{2}\frac{f\lambda}{\pi^2 r_0{}^2} . \tag{5.22}$$

The maximum error occurs for f large and r_0 small. In the laser fusion system the minimum r_0 is about 1 cm. The maximum focal length is about 1 m. The focus error for these parameters is 0.005 wavelengths. This error is completely negligible so there is no need to deviate from the paraxial focal plane.

CHAPTER 6

DESCRIPTION OF THE LOTS CODE

A major part of this research effort has been the development of the LOTS code for laser fusion system analysis. The program is written in FORTRAN and consists of nine overlays, 120 subroutines, and over 8,000 statements. The code has been under development since 1975. It has been used in analyzing the Gemini (Viswanathan, Hayden, and Liberman, 1979), Helios (Lawrence, Liberman, and Viswanathan, 1977), and Antares (Lawrence and Sweatt, 1978) systems. General application of the code was addressed in a paper by Lawrence and Wolf (1979).

In spite of its size and internal complexity LOTS is designed to be readily used by persons familiar with the laser fusion system. The user has available 75 command words each of which defines an operation on the matrix. These commands provide for construction of the matrix representing the pulse and for manipulation of the pulse to simulate the various components and processes that exist in the laser fusion system. A variety of means of measuring and displaying the matrix parameters are available.

Complete operating instructions for program use are given in the LOTS Manual (Lawrence, 1979). This manual includes 33 examples illustrating 56 of the commands in problems similar to those encountered in the laser fusion system.

As the best means of describing the capabilities of LOTS and clarifying the analysis in Chapter 7, a brief description of each of the command words is presented below.

LOTS Commands

Command Structure

Input to LOTS consists of successive command lines. Each command line must contain a command word and up to six numeric entries. Command words and numeric entries are separated by one or more blanks. The command word and numeric entries may occupy any position on an 80-column input line with the restriction that the numeric entries must occur in the correct order.

Numeric entries may occur in any FORTRAN readable format. For example, the number 8 may be written:

```
8
8.
.8E+01
.08E2
8E0
.8+1
```

Extraneous characters in or attached to the number will cause the program to abort.

General Operational Commands

It is often helpful to annotate the program by means of comment cards. A comment card may be formed by making the first word the single letter "C" followed by one or more blanks and then any comments

C (comments)

There are three switches that change the program operation. The program will normally repeat each command as it is read. This may be switched off by

NOECHO

or switched back on by

ECHO

The program is assumed to be used from a teletype terminal. However, if output is directed to a device with overstrike capability, then grey-tone representations of FRINMAP, INTMAP, and PHASMAP can be made by using the command word

GREY V1

to switch on the overstrike feature. For line printer output use V1 = 0. For teletype output use V1 = 1. At Los Alamos use V1 = 2 for the Tektronics graphics terminal. V1 = 3 should be used on the Tektronics 4051 graphic terminal. This form may also be used at Los Alamos on the graphics terminal and is faster than V1 = 2.

GREY mode may be turned off by

NOGREY

The diffraction features of the program in DIST, GAIN, and GAINTP may be turned off by

DISTOFF

or turned back on by

DISTON

The wavelength is normally 10.6 μm. It may be reset by LAMDA in micrometers

LAMDA

A macro consisting of command lines may be formed by

DEFMACRO V1

V1 denotes the number of following commands which are to be formed into the macro. Calling DEFMACRO a second time will redefine the macro.

The macro is called by

MACRO V1

V1 denotes the number of times the macro is to be executed. If no value for V1 is entered the macro is executed once.

LOTS has provision for identifying points along an optical train by a station number and title. A title must be provided as the next line after the STATION command.

STATION (Title)

This identifying information is printed out with various display commands.

The program may be terminated by any of the following commands:

$\boxed{\text{END}}$

$\boxed{\text{EXIT}}$

$\boxed{\text{BYE}}$

$\boxed{\text{STOP}}$

or by an end-of-file mark.

Linear Operations

The correspondence between the matrix points and physical distance is defined by

$\boxed{\text{UNITS V1}}$

V1 has dimensions of centimeters per matrix unit. In general, the units should be specified before any other operation. Default value for UNITS is 1 cm.

The energy density distribution is assumed to be Gaussian with a $1/e^2$ radius defined by

$\boxed{\text{APOD V1 V2}}$

V1 is the radius of the Gaussian. If V2 is positive it defines the peak energy density in joules per square centimeter. If V2 is negative its absolute value defines the energy in the pulse. If V2 is not specified the default peak energy density is 1 mJ/cm^2.

The energy density may be changed by a multiplicative factor V1 with

MULT V1

The clear aperture may be defined by a variety of functions. The extent of the matrix is shown in Fig. 6.1. A circular aperture centered about the origin of radius V1 may be defined by

CLAP V1

The command

BLOWUP V1

expands the distribution using linear interpolation by V's.

The command

SHRINK V1

shrinks the distribution by V1.

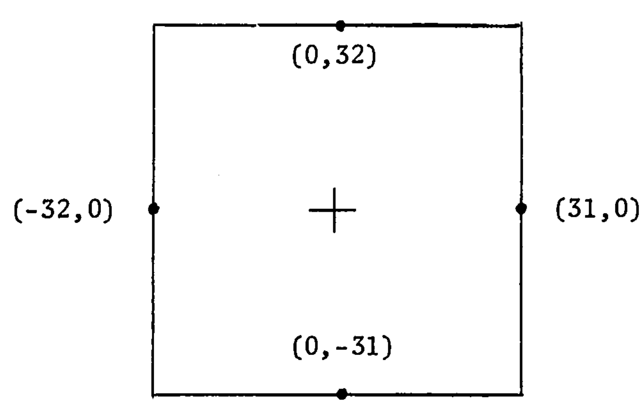

Figure 6.1. Dimensions of 64 x 64 Matrix.

If CLAP is called with no value for V1 the current value of CLAP is returned. If V1 is less than zero, matrix units are assumed for V1. This is true for CLAPXY, COBXY, and COBS as well. If V1 is greater than 46 units, all points will be included. A central obscuration of radius V1 may be defined by

COBS V1

Decentered clear apertures and obscurations may be defined by

CLAPXY V1 V2 V3 V4

COBSXY V1 V2 V3 V4

where

V1 = radius

V2 = X displacement

V3 = Y displacement

V4 = transmission of semi-opaque region.

A square aperture may be defined by

SQUARE V1

where V1 is the half width of the square.

Any general aperture consisting of straight line segments may be defined by its vertex points with GCLAP and GCOBS. GCLAP creates a general aperture.

```
GCLAP

X1    Y1
X2    Y2
X3    Y3
X4    Y4
 (etc.)
```

The X's and Y's are the vertex coordinates.

The polyhedron must consist of vertex angles less than 180^{o}.

GCOBS creates a general obscuration

```
GCOBS

X1    Y1
X2    Y2
X3    Y3
X4    Y4
 (etc.)
```

GCLAP and GCOBS may be combined to create composite apertures.

The display function PR64 is helpful in checking the accuracy of the aperture construction.

The first and third order aberrations of tilt, focus, astigmatism, coma, and spherical aberration may be added by

```
TILT V1 V2
```

```
FOCUS V1
```

```
AST V1 V2
```

```
COMA V1 V2
```

$\boxed{\text{SPH V1}}$

V1 is the error in wavelength at the edge of the clear aperture. V2 is the azimuth angle in degrees. Azimuth is measured clockwise from vertical.

In addition, tilt may be added by

$\boxed{\text{TILTRAD V1 V2}}$

where V1 is the tilt angle in radians and V2 is the azimuth angle in degrees.

Focus error may also be added by

$\boxed{\text{PHASERAD V1}}$

where V1 is the radius of the phase curvature in centimeters.

$\boxed{\text{NEWABR V1 V2 V3}}$

NEWABR adds a smoothed random aberration to the distribution. V1 determines the peak-to-valley wavefront error. If V1 is negative it is interpreted to be the RMS wavefront error. V2 is the autocorrelation radius at the $1/e^2$ point. If V2 is negative the number is interpreted to be in matrix units. V3 specifies the seed of the wavefront. Any positive odd integer will yield a unique wavefront. If the seed is not specified, a seed is automatically chosen. The same seed always gives the same wavefront.

The command

$\boxed{\text{ABR}}$

reads a title and a set of 36 Zernike polynomial coefficients from file ABR. The FRINGE program can be used to generate the polynomial coefficients in correct format by putting the word PUNCH in the command sequence.

Each call to ABR causes a set of coefficients to be read from ABR. The user should construct ABR by combining the polynomial sets from FRINGE in the order in which they are to be called.

The matrix may be set to unity at all points by

$\boxed{\text{ZERO}}$

The matrix is set to unity when LOTS starts.

Diffraction and Imaging

A focusing lens or mirror produces a far field pattern at the focal plane with a phase factor of radius equal to the focal length. The command

$\boxed{\text{IMAGE V1}}$

accomplishes this task where V1 is the focal length. V1 may be positive or negative according to the power of the focusing element.

Divergent light from the image distribution may be recollimated by

$\boxed{\text{PUPIL V1}}$

with V1 equal to the focal length of the lens.

The effect of free space propagation of a collimated beam is calculated by

$$\boxed{\text{DIST V1}}$$

V1 is the propagation distance. The accuracy of this calculation is limited for short sampling distances by the number of points across the beam distribution. The finite width of the matrix limits the accuracy at long propagation distances. As the beam expands by diffraction, it overfills the matrix causing aliasing.

If the distribution obtained with DIST shows significant energy near the edge of the matrix then the accuracy of the calculation is suspect. The DIST routine will automatically switch to a combination of FOCUS and IMAGE routines which accomplish the same thing as DIST but which rescale the matrix to reduce aliasing problems.

Nonlinear Phenomena

In the CO_2 laser amplifiers the amplifying medium is reasonably well described by the Frantz-Nodvick equation.

For a collimated beam the Frantz-Nodvick equation may be solved in closed form

$$\left(e^{EO/ES} - 1\right) = e^{gL}\left(e^{EI/ES} - 1\right)$$

where

ES = saturation energy density

EI = input energy density

EO = output energy density

g = gain per unit length

L = length.

The command is

$$\boxed{\text{GAIN V1 V2 V3}}$$

where

V1 = gain per centimeter

V2 = saturation energy density in millijoules per square centimeter

V3 = length of amplifier.

For a noncollimated beam the differential equation form of the Frantz-Nodvick must be solved

$$\frac{dE}{dx} = ES * g\left(1 - e^{-E/ES}\right) - \frac{2B}{(B+X)}$$

where

E = intensity

g = gain per cm

ES = saturation energy density

B = (DI x L)/(DO - DI)

DI = input diameter

DO = output diameter

L = length of amplifying medium.

This differential equation is solved numerically for each nonzero matrix point.

The function is called by

$$\boxed{\text{GAINTP V1 V2 V3 V4 V5}}$$

where

V1 = gain per cm

V2 = saturation intensity in mJ/cm^2

V3 = input diameter

V4 = output diameter

V5 = length of amplifying media.

Saturable absorbers may be simulated with LOTS. It is necessary to have experimental or analytical data describing the transmission versus input energy density for any saturable absorber of interest. LOTS uses a four-parameter curve fit. The parameters are determined by the following technique.

Plot the transmission versus input energy density on log-log paper. The curve should look approximately like Fig. 4.2.

The curve is described by TMAX, TMIN, ES, and the slope. TMAX is the maximum transmission, TMIN is the minimum transmission. TAVG is the geometric mean of TMAX and TMIN. The energy density point having a transmission of TAVG is ES, the saturation energy density. The value of the slope to be used is the slope at ES read off the log-log plot. Initial values are then determined by using the command

$$\boxed{\text{SATPLOT V1 V2 V3 V4}}$$

where

V1 = TMAX

V2 = TMIN

V3 = saturation intensity, ES

V4 = slope.

This function plots and lists the curve of transmission versus energy density based on the four parameters. The user may then adjust the numeric entries and recompute SATPLOT until a satisfactory fit is obtained.

The saturable absorber is simulated by

SATFUNC V1 V2 V3 V4

where

V1 = TMAX

V2 = TMIN

V3 = saturation intensity, ES

V4 = slope.

With sufficiently high energy density the index of refraction becomes a variable. The command

INTPHAS V1

allows this effect to be introduced. V1 is the ratio of phase error in wavelengths to beam intensity in J/cm^2.

Display Commands

The command word

ENCIRC

displays an encircled energy calculation of the beam matrix. The command word

ENERGY

gives the total energy in the beam matrix.

A summary of the energy at each specified station is generated by

ENGPLOT

The command word

STREHL

computes the Strehl ratio.

The command word

RELPK

gives the maximum intensity.

A summary of the Strehl ratio at each specified station is generated by

STRPLOT

The summary file is reinitialized by this command

RESTART

An interferogram of the beam distribution may be created by

FRINMAP V1 V2 V3

A plane wave of energy density equal to the peak energy density of the beam distribution with a tilt of V1 waves at the edge of the array and of azimuth angle V2 in degrees. V3 specifies the relative energy density of the reference wave. If V3 is unspecified the reference wave energy density is set equal to the peak energy density of the beam wavefront.

A map of the phase may be created by

PHASMAP

The program must by in GREY mode.

A map of the energy density distribution is given by

INTMAP V1

In GREY mode, V1 specifies the upper limit to the grey scale in terms of the fractional peak energy density. Energy densities greater than V1 are printed at the darkest grey level. A zero value of V1 is interpreted as 1. In NOGREY mode only points greater than V1 relative energy density are displayed. In NOGREY mode, if V1 is not specified, it is interpreted as zero. INTMAP interpolates to give a square pattern on the line printer.

FRINMAP, PHASMAP, and INTMAP are printed on a 60-column by 36-row area which appears square on standard line printer format. LOTS uses linear interpolation to accomplish this.

The routine

PR64

is similar to INTPHAS except that no linear interpolation is used. Each printed point corresponds to a matrix element.

The command word

$\boxed{\text{PDATA}}$

prints the current station title and station number, the energy and Strehl ratio, the program units, a half x-profile of the complex amplitude and a full x-profile of the energy density.

$\boxed{\text{PSHORT}}$

is the same as PDATA except the complex amplitude information is omitted.

$\boxed{\text{IDATA}}$

is the same as PDATA except that the maximum peak energy density is substituted for the Strehl ratio.

$\boxed{\text{ISHORT}}$

is the same as IDATA without the complex amplitude data.

A circular section of the beam energy density distribution of 8 units' radius is printed by the command word

$\boxed{\text{PRININ V1}}$

If V1 equals 1 then the phase in radians is printed also.

The wavefront statistic may be displayed by the command

$\boxed{\text{WAVSTAT}}$

The peak-to-valley error and the RMS error in wavelengths are printed.

Data along a linear scan of the distribution may be obtained by

XSCAN V1

YSCAN V1

V1 specifies the row for SCAN (between 31 and 32) or the column for YSCAN (between 32 and 31).

A row-by-row listing of the complex values of the matrix may be produced by

DUMP V1 V2

For this function the rows are identified by numbers -31 to 32. V1 is the lower row number, V2 is the top row number. A complete listing of the matrix given by DUMP -31 32 creates about 17 pages of output.

It is occasionally useful to have a page advance in output directed to a line printer. The command

PAGE

causes the line printer to start a new page.

The command

TIME

gives the elapsed CPU time since the beginning of the job.

Matrix Storage

The matrix and the program switches may be stored and retrieved by the commands

BUFFOUT V1

BUFFIN V1 V2

BUFFOUT writes the matrix and other associated variables as a record to a file called TAPE4. This file is stored for later use after program termination as OLDBUF automatically by the procedure file operating LOTS. Repeated calls to BUFFOUT will store multiple records. If V2 is nonzero, TAPE4 is rewound before writing.

BUFFIN retrieves the matrix and associated variables from NEWBUF created by a previous LOTS run. If V1 is nonzero, then BUFFIN retrieves the record from TAPE4. This allows temporary storage of the record during the program. Retrieval from TAPE4 with V2 zero rewinds TAPE4 before reading. If V2 is positive, LOTS starts from the present position without rewind and advances V2-1 records before starting retrieval.

The MASK functions allow the user to store and retrieve any complex 64 x 64 matrix. These masks may be created by LOTS or by an external FORTRAN program.

The command

STORE "Keyname"

will store the current distribution as a mask with identifier "keyname."

The units of this distribution are also stored. Up to 60 masks may be stored.

The command

LIST

lists the contents of the MASK file.

The command

GETMASK
"Keyname"

will multiply the current distribution by the mask names "keyname." If the current units are different from the mask units, the mask will be expanded, shrunk, or inverted as necessary to match the current units. If the MASK is stored with zero units, no scaling is done.

GETMASK may be used to store and recall the distribution without changing the program switches. The command ZERO should be called to set the matrix to unity at all points and then GETMASK should be called with the desired kayname.

Command word

ADDFILE
"Keyname"
"Units"

causes LOTS to read a mask from local file TAPE22 and add it to the MASK file. The user must enter the keyname and the numerical value of the units to be associated with the mask in the line immediately following ADDFILE.

The file attached as TAPE22 should be created by a FORTRAN program from a complex 64 x 64 array.

Let A be the complex array.

Let K be the output tape number.

Then

```
BUFFER OUT(k,1),  (A(1,1), A(64,64))
III = UNIT(K)
```

will create a file of the proper form for LOTS.

The command

DELETE "Keyname"

will remove the keyname from the listing. The size of the MASK file can be reduced by command word

COPY

At program termination, the procedure file will store the new condensed version of the MASK file.

Details needed for accessing and running the program at Los Alamos or the University of Arizona are included in the LOTS Manual.

CHAPTER 7

TYPICAL ANALYSIS

The project which is the subject of this dissertaion was limited to developing a program for analyzing the CO_2 laser fusion systems. The responsibility for the important task of defining the configuration to be analyzed falls on the user. However, in order to illustrate the operation of the program, an analysis of a system which is approximately the same as a preliminary design of the Antares power amplifier (circa February 1978) is presented here. Because this analysis was based on a preliminary design and because of the unofficial nature of the documentation, this analysis should not be construed as being directly applicable to the Antares system in its final form.

The system configuration is based on a memorandum by Jones and Zeigner (1978) and by a component list by Jones (1978). Characteristics of the gain were obtained from P. N. Wolfe by phone. The component surface accuracy tolerances were the subject of some debate at that stage of design. The surface accuracy values in this analysis represent one out of several different viewpoints voiced at that time.

The analysis covers the last part of the Antares system which begins at the vacuum input window to the power amplifier. The power amplifier is shown schematically in Fig. 1.3. An annular beam passes through the vacuum input window and is deflected to hit a polyhedron mirror which divides the beam into 12 segments. The analysis follows one segment through more turning mirrors and a spatial filter. Four relay mirrors follow the spatial filter. Leaving the last relay mirror the beam diverges slightly as it passes through four gain cells. Cold gas absorption exists in the regions outside the gain cells. Between the absorber window and the back reflector lies the saturable material. The pulse leaves the back reflector converging very slightly. The pulse traverses the four gain cells again and exits the gain media region through the output window. Additional mirrors translate and steer the beam. The final mirror is the focusing parabola.

Table 7.1 defines the necessary component characteristics. The distance associated with each component is the distance between that component and the previous one. The index of the medium is handled by using reduced distances in the data. Focal length is given a positive value if the element acts to converge the beam. The clear aperture values indicate the scaling of a normalized trapezoidal aperture with normalized coordinates (-1,.729), (1,.729), (-.633,-.729) and (.633, -.729). The beam passes through the absorber window twice so that random aberration with the same seed must be used in both cases. It is assumed that the saturable absorber data reflect measurement in the double pass mode used in the amplifier.

Table 7.2 gives the exact input to LOTS for this analysis. The aperture shape is assumed to be a constant shape whose size follows the geometrical size of the propagating laser pulse. The size is therefore constant in matrix units, making the mask functions very convenient. The first step is to define the mask with the name TRAP which

Table 7.1. Component Characteristics.

NO.	NAME	DIST	FOCAL LENGTH	TRANS - MISSION	WAVE ERROR	CLEAR APERTURE	DIVERGENCE	g_o	Es
1	Vacuum Window	-	-	.98	.05	2.07	0.0	-	-
2	Turning Mirror	161.8	-	.99	.05	2.07	0.0	-	-
3	Polyhedron Mirror	20.32	-	.99	.05	2.07	0.0	-	-
4	Turning Mirror	125.48	-	.99	.05	2.07	0.0	-	-
5A	Trombone 1	28.96	-	.99	.05	2.07	0.0	-	-
5B	Trombone 2	11.94	-	.99	.05	2.07	0.0	-	-
5C	Trombone 3	11.94	-	.99	.05	2.07	0.0	-	-
6	Focus Mirror	180.34	129.79	.99	.05	2.07	-.01595	-	-
7	Spatial Filter	129.79	-	-	-	.033	-	-	-
8	Input Window	213.87	-	.99	.05	3.39	.01595	-	-
9	Relay Mirror 1	75.69	73.03	.99	.05	4.59	-.04720	-.00156	286
10	Relay Mirror 2	50.8	-	.99	.05	3.32	-.04720	-.00156	286
11	Relay Mirror 3	50.8	-43.56	.99	.05	2.05	0.0	-.00156	286
12	Relay Mirror 4	62.23	-105.41	.99	.05	2.07	.01959	-.00156	286
	Cold Gas	141.89	-	-	-		.01959	-.00156	286
	Gain Cell 1	75	-	-	-		.01959	.0219	313
	Cold Gas	100.41	-	-	-		.01959	-.00156	286
	Gain Cell 2	75	-	-	-		.01959	.0219	313

Table 7.1. Continued.

NO.	NAME	DIST.	FOCAL LENGTH	TRANS - MISSION	WAVE ERROR	CLEAR APERTURE	DIVERGENCE	g_o	Es
	Cold Gas	100.41	-	-	-	-	.01959	-.00156	286
	Gain Cell 3	75	-	-	-	-	.01959	.0219	313
	Cold Gas	100.41	-	-	-	-	.01959	-.00156	286
	Gain Cell 4	75	-	-	-	-	.01959	.0129	313
13	ABS Window	159.35	-	.98	.1	19.81	.01959		
	Saturable Absorber	TMAX = .6, ES = .014, TMIN = 1.2 x 10^{-4}, SLOPE = .9							
14	Back Reflector	50.82	-	.98	.1	20.7	-.000773	-	-
13	ABS Window	50.8	-	.98	.1	19.81	-.000773	-	-
	Cold Gas	159.35	-	-	-	-	-.000773	-.00156	286
	Gain Cell 4	75	-	-	-	-	-.000773	.0219	313
	Cold Gas	100.41	-	-	-	-	-.000773	-.00156	286
	Gain Cell 3	75	-	-	-	-	-.000773	.0219	313
	Cold Gas	100.41	-	-	-	-	-.000773	-.00156	286
	Gain Cell 2	75	-	-	-	-	-.000773	.0219	313
	Cold Gas	100.41	-	-	-	-	-.000773	-.00156	286
	Gain Cell 1	75	-	-	-	-	-.000773	.0219	313
15	Output Window	159	-	.98	.1	20.0	-.000773	-.00156	286
16	Periscope 1	297	-	.99	.1	19.7	-.000773	-	-

Table 7.1. Continued.

NO.	NAME	DIST.	FOCAL LENGTH	TRANS-MISSION	WAVE ERROR	CLEAR APERTURE	DIVERGENCE	g_o	Es
17	Periscope 2	73.66	-	.99	.1	19.6	-.000773	-	-
18	Turning Mirror	3655	-	.99	.1	16.87	-.000773	-	-
19	Fold Mirror	2161.54	-	.99	.1	15.21	-.000773	-	-
20	Focus Mirror	150	294.64	.99	.1	15.1	-.0512	-	-

Table 7.2. Input Data for the Antares System.

```
C      CALCULATIONS FOR THE ANTARES LASER FUSION SYSTEM
C
C      FORM A UNIFORM INTENSITY INPUT PULSE
C
C
C      DEFINE TRAPEZOIDAL APERTURE
C      THE APERTURE SIZE REMAINS CONSTANT WITH RESPECT TO
C      MATRIX UNITS
C
UNITS .1
GCLAP
-2.07 1.51
-1.31 -1.51
1.31 -1.51
2.07 1.51
UNITS
STORE
TRAP
UNITS .1
C      ADJUST INTENSITY TO ACHIEVE 2.25 JOULES AFTER THE SPATIAL FILTER
MULT 359.2416839
STATION
INPUT PULSE
C      FORM OUTPUT DATA MACRO
DEFMACRO 5
PSHORT
FRINMAP 6 90
STRPLOT
ENGPLOT
PAGE
GREY
MACRO
C
C
C      FUNCTION NEWABR INTRODUCES A SMOOTHED RANDOM WAVEFRONT OF .05
C      WAVES RMS WITH AUTOCORRELATION WIDTH OF 5 MATRIX UNITS OF
C      TYPE 1.
C
NEWABR .05 -5 1
MULT .98
STATION
1 VACUUM WINDOW
MACRO
C
DIST 161.8
NEWABR .1 -5 3
GETMASK
TRAP
MULT .99
STATION
2 TURNING MIRROR
MACRO
C
DIST 20.32
NEWABR .05 -5 5
```

Table 7.2, Continued, Input Data for the Antares System.

```
GAINTP -.00156 286 20.48 20.4 100.41
GAINTP .0219 313 20.4 20.35 75
STATION
GAIN CELL 3
MACRO
C
GAINTP -.00156 286 20.35 20.27 100.41
GAINTP .0219 313 20.27 20.21 75
STATION
GAIN CELL 2
MACRO
C
GAINTP -.00156 286 20.21 20.14 100.41
GAINTP .0219 313 20.14 20.08 75
STATION
GAIN CELL 1
MACRO
C
GAINTP -.00156 286 20.08 19.96 159
NEWABR .1 -5 33
GETMASK
TRAP
MULT .98
STATION
15 OUTPUT WINDOW
MACRO
C
GAINTP 0 0 19.96 19.73 297
NEWABR .1 -5 35
GETMASK
TRAP
MULT .99
STATION
16 PERISCOPE 1
MACRO
C
GAINTP 0 0 19.73 19.67 73.66
NEWABR .1 -5 37
GETMASK
TRAP
MULT .99
STATION
17 PERISCOPE 2
MACRO
C
GAINTP 0 0 19.67 16.87 3655
NEWABR .1 -5 39
GETMASK
TRAP
MULT .99
STATION
18 TURN MIRROR
MACRO
C
GAINTP 0 0 16.87 15.21 2161.54
NEWABR .1 -5 41
```

Table 7.2, Continued, Input Data for the Antares System.

```
GETMASK
TRAP
MULT .99
STATION
3 POLYHEDRON MIRROR
MACRO
C
DIST 125.48
NEWABR .05 -5 7
GETMASK
TRAP
MULT .99
STATION
4 TURNING MIRROR
MACRO
C
DIST 28.96
NEWABR .05 -5 9
GETMASK
TRAP
MULT .99
STATION
5A TROMBONE 1
MACRO
C
DIST 11.94
NEWABR .05 -5 11
GETMASK
TRAP
MULT .99
STATION
5B TROMBONE 2
MACRO
C
DIST 11.94
NEWABR .05 -5 13
GETMASK
TRAP
MULT .99
STATION
5C TROMBONE 3
MACRO
C
DIST 180.34
NEWABR .05 -5 15
GETMASK
TRAP
MULT .99
STATION
6 FOCUS MIRROR
MACRO
C
IMAGE 129.79
C
C     SPATIAL FILTER
C
```

Table 7.2, Continued, Input Data for the Antares System.

```
CLAP .033
ENERGY
PUPIL 213.87
NEWABR .05 -5 17
GETMASK
TRAP
MULT .99
STATION
8 INPUT WINDOW
MACRO
C
C     COLD GAS ABSORBTION
C
GAINTP -.00156 286 3.39 4.59 75.69
NEWABR .05 -5 19
GETMASK
TRAP
MULT .99
STATION
9 RELAY MIRROR 1
MACRO
C
GAINTP -.00156 286 4.59 3.32 50.8
NEWABR .05 -5 21
GETMASK
TRAP
MULT .99
STATION
10 RELAY MIRROR 2
MACRO
C
GAINTP -.00156 286 3.32 2.05 50.8
NEWABR .05 -5 23
GETMASK
TRAP
MULT .99
STATION
11 RELAY MIRROR 3
MACRO
C
GAIN -.00156 286 62.23
NEWABR .05 -5 25
GETMASK
TRAP
MULT .99
STATION
12 RELAY MIRROR 4
MACRO
C
GAINTP -.00156 286 2.07 4.84 141.89
GAINTP .0219 313 4.84 6.31 75
STATION
GAIN CELL 1
MACRO
C
GAINTP -.00156 286 6.31 8.273 100.41
```

Table 7.2, Continued, Input Data for the Antares System.

```
GAINTP .0219 313 8.273 9.739 75
STATION
GAIN CELL 2
MACRO
C
GAINTP -.00156 286 9.739 11.702 100.41
GAINTP .0219 313 11.702 13.168 75
STATION
GAIN CELL 3
MACRO
C
GAINTP -.00156 286 13.168 15.131 100.41
GAINTP .0219 313 15.131 16.597 75
STATION
GAIN CELL 4
MACRO
C
GAINTP -.00156 286 16.597 19.712 159.35
NEWABR .1 -5 31
GETMASK
TRAP
MULT .98
STATION
13 ABS WINDOW
MACRO
C
SATFUNC .6 .014 1.2E-04 .9
STATION
SATURABLE ABS
MACRO
C
IMAGE -1008.08
PUPIL 1058.9
NEWABR .1 -5 29
MULT .98
GETMASK
TRAP
STATION
14 BACK REFLECTOR
MACRO
C
GAINTP 0 0 20.7 20.66 50.8
NEWABR .1 -5 31
GETMASK
TRAP
MULT .98
STATION
13 ABS WINDOW
MACRO
C
GAINTP -.00156 286 20.66 20.54 159.35
GAINTP .0219 313 20.54 20.48 75
STATION
GAIN CELL 4
MACRO
C
```

Table 7.2, Continued, Input Data for the Antares System.

```
GETMASK
TRAP
MULT .99
STATION
19 FOLD MIRROR
MACRO
C
GAINTP 0 0 15.21 15.1 150
NEWABR .1 -5 43
GETMASK
TRAP
MULT .99
STATION
20 FOCUS MIRROR
MACRO
BUFFOUT
C
C     SHRINK PUPIL DISTRIBUTION FOR BETTER IMAGE RESOLUTION
C
SHRINK .5
IMAGE 294.64
ENCIRC
PAGE
ISHORT
```

will be applied at the appropriate places later on. Secondly, a uniform pulse distribution is assumed. The initial energy density is set to achieve 2.25 J in the pulse immediately after the spatial filter. The data display is defined by DEFMACRO. The command NEWABR .05 -5 1 defines a random wavefront with peak-to-valley error of 0.05 waves and auto-correlation width of five matrix units. The aberration seed in this case is "1." Successive odd integers define unique seeds. The efficiency of the component is 0.98 entered by MULT .98. GETMASK calls the trapezoidal aperture TRAP. The command station records the current Strehl ratio and energy with a name supplied in the line immediately following. Subsequent surfaces follow Table 7.1 according to usage defined in Chapter 6.

The calculations from the data in Table 7.2 produce 263 pages of output. Table 7.3 shows the first three pages of output. Commands are preceded by two hyphens or in the case of commands, in the macro file by two periods. Figure 7.1 is an interferogram of the input pulse that indicates a uniform energy density free of aberration.

Figure 7.2 shows the interferogram of the focusing mirror just prior to the spatial filter. The crooked fringes indicate the presence of aberration. Figure 7.3 shows the first optical element following the spatial filter. The fringes are almost perfectly straight. The contrast of the fringes gives a visual indication of the nonuniformity of energy density introduced by the spatial filter. The interferogram is formed by adding a reference wavefront with a uniform energy density equal to the maximum energy density in the pulse. The energy density of the

Table 7.3. Antares Calculations. Input Pulse Formation.

```
--C     CALCULATIONS FOR THE ANTARES LASER FUSION SYSTEM
--C
--C     FORM A UNIFORM INTENSITY INPUT PULSE
--C
--C
--C     DEFINE TRAPEZOIDAL APERTURE
--C     THE APERTURE SIZE REMAINS CONSTANT WITH RESPECT TO
--C     MATRIX UNITS
--C
--UNITS .1
ONE MATRIX UNIT =     .1000000  CM.

--GCLAP
 POINTS ARE
  -2.07000E+00   1.51000E+00
  -1.31000E+00  -1.51000E+00
   1.31000E+00  -1.51000E+00
   2.07000E+00   1.51000E+00
--UNITS
ONE MATRIX UNIT =    0.0000000  CM.

--STORE
KEYNAME     TRAP        STORED
    3  FILES STORED

--UNITS .1
ONE MATRIX UNIT =     .1000000  CM.

--C     ADJUST INTENSITY TO ACHIEVE 2.25 JOULES AFTER THE SPATIAL FILTER
--MULT 359.2416639
MULTIPLY INTENSITY BY     3.59242E+02

--STATION
*INPUT PULSE
--C     FORM OUTPUT DATA MACRO
--DEFMACRO 5
*** LIST OF MACRO COMMANDS ***

..PSHORT
..FRINMAP 6 90
..STRPLOT
..ENGPLOT
..PAGE

*** END OF MACRO LIST ***

--GREY
--MACRO
..PSHORT
STATION        1

INPUT PULSE

ENERGY =     3.761260E+00  JOULES
```

Table 7.3. Continued.

SIREHL RATIO 1.00000

ONE MATRIX UNIT = .1000000 CM.

PROFILE OF INTENSITY JOULES/ SQ. CM.

0.	0.	0.	0.	0.	0.	0.	0.
0.	0.	0.	0.	0.	0.	0.	0.
3.59E-01	3.59E-01	3.59E-01	3.59E-01	3.59E-01	3.59E-01	3.59E-01	3.59E-01
3.59E-01	3.59E-01	3.59E-01	3.59E-01	3.59E-01	3.59E-01	3.59E-01	3.59E-01
3.59E-01	3.59E-01	3.59E-01	3.59E-01	3.59E-01	3.59E-01	3.59E-01	3.59E-01
3.59E-01	3.59E-01	3.59E-01	3.59E-01	3.59E-01	3.59E-01	3.59E-01	3.59E-01
3.59E-01	0.	0.	0.	0.	0.	0.	0.
0.	0.	0.	0.	0.	0.	0.	0.

..FRINMAP 6.00E+00 9.00E+01

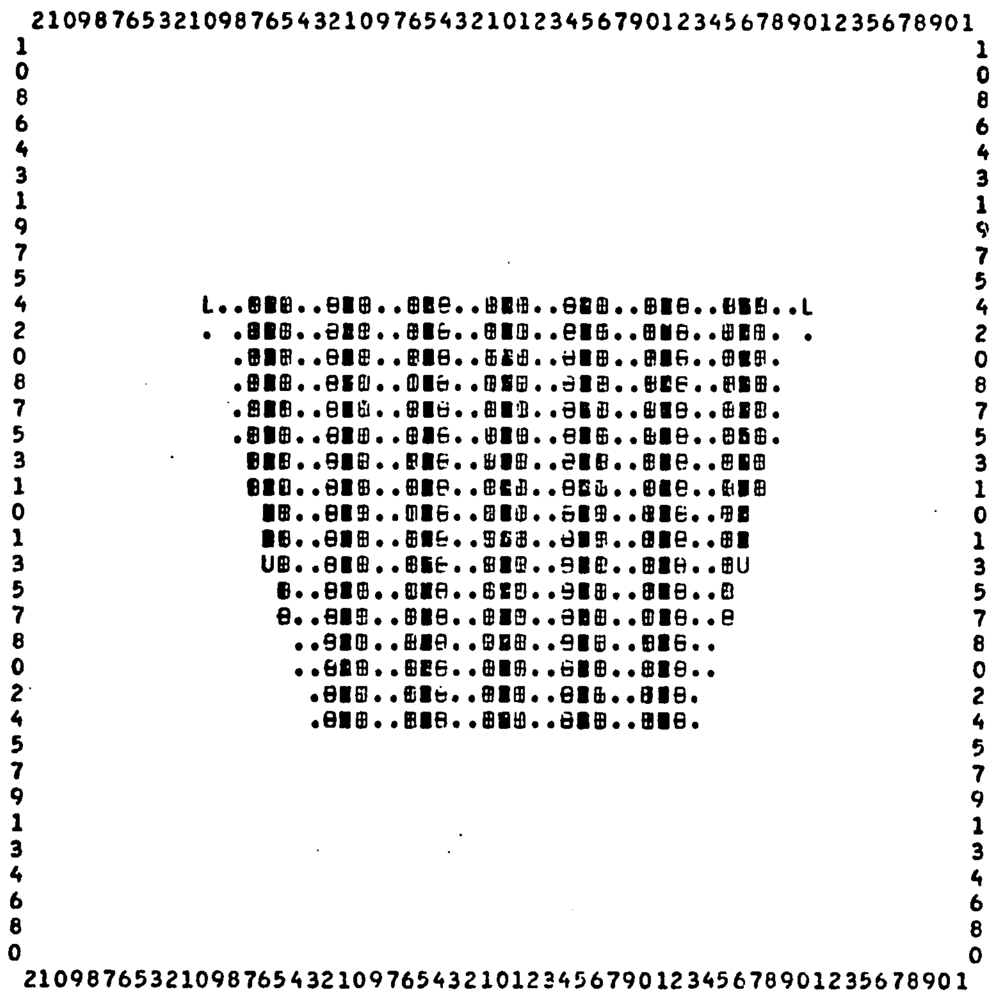

INPUT PULSE

Figure 7.1. Interferogram of the Input Pulse.

..FRINMAP 6.00E+00 9.00E+01

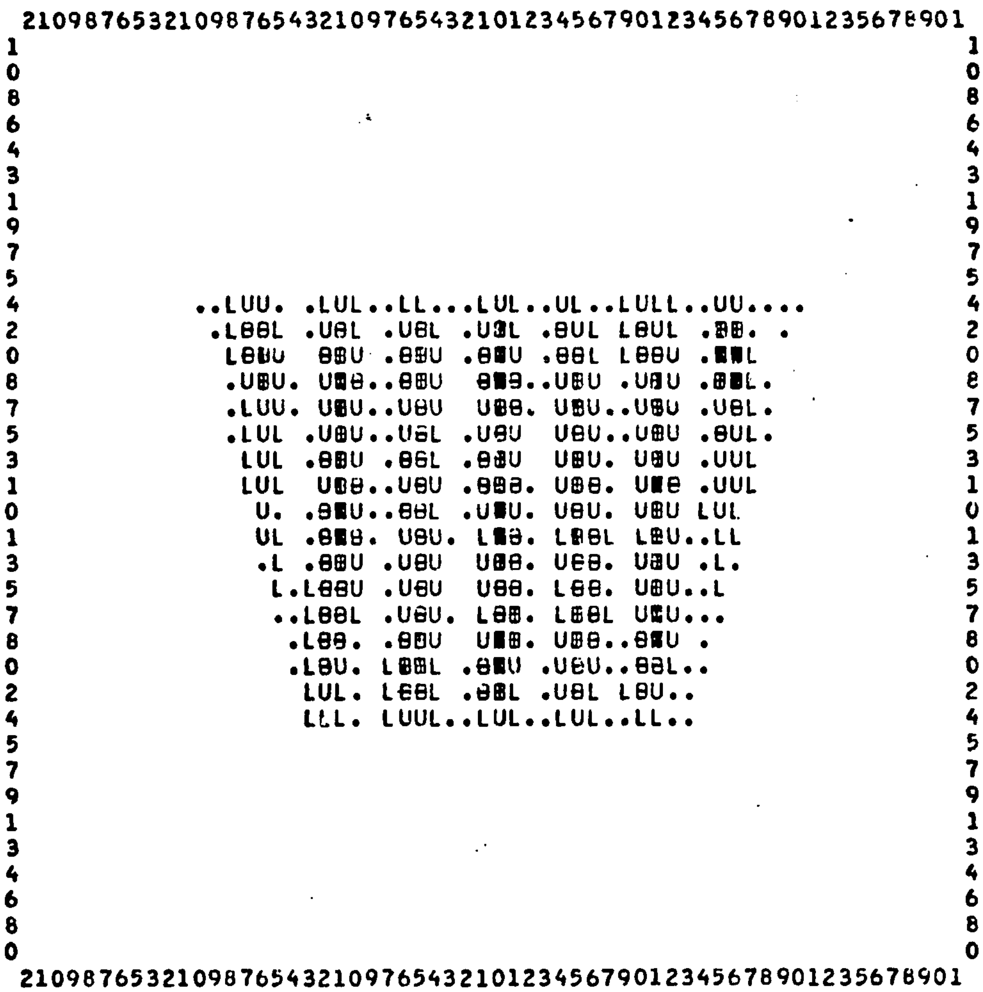

6 FOCUS MIRROR

Figure 7.2. Interferogram at the Focus Mirror.

..FRINMAP 6.00E+00 9.00E+01

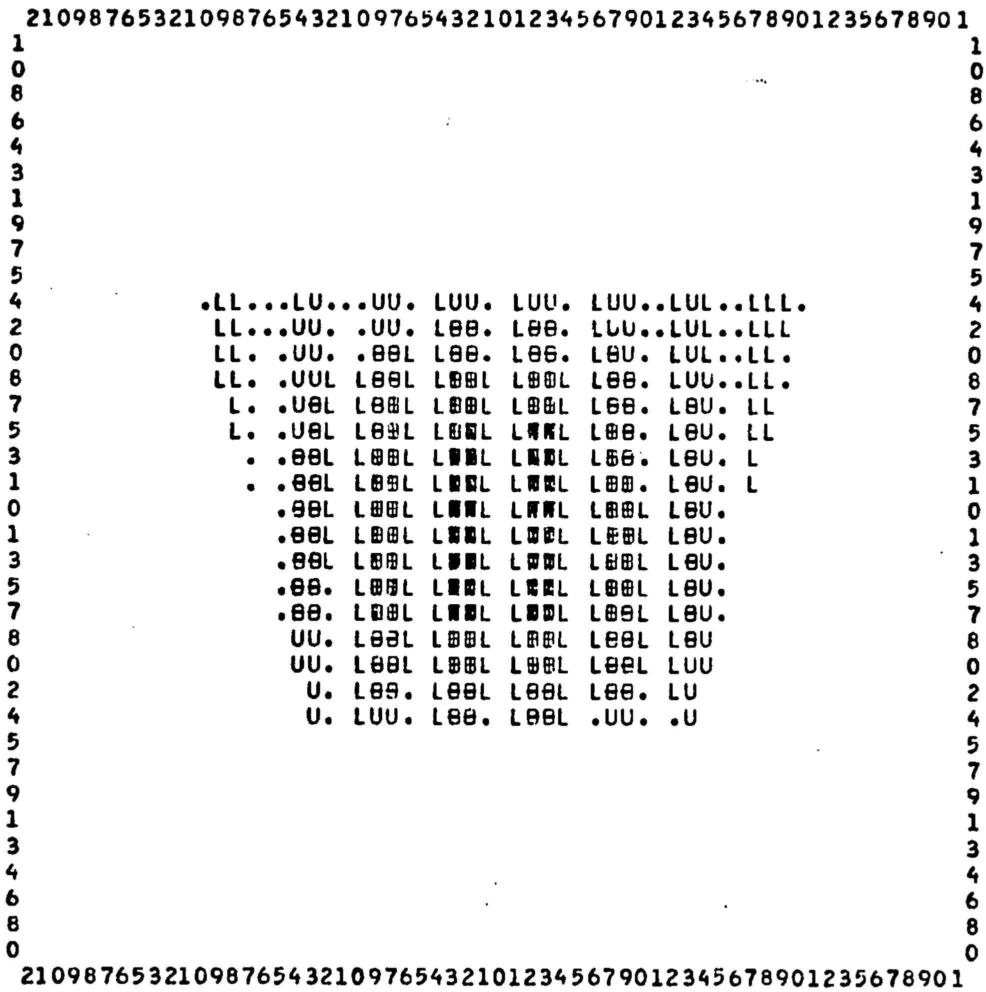

8 INPUT WINDOW

Figure 7.3. Interferogram after Spatial Filter.

pulse drops from a maximum in the center so contrast in the interferogram drops toward the edge.

Figure 7.4 shows the pulse just prior to entering the gain cells. Conditions are similar to Fig. 7.3 except that there is slightly greater aberration present. Figure 7.5 shows the pulse at the end of the fourth gain cell. Diffraction has scattered light outside the original aperture. The gain medium is somewhat saturated and the low energy density regions are amplified more. This reduces the degree of contrast variation. This effect is more readily observed in Fig. 7.6 after the trapezoidal aperture at the saturable absorber. Comparison of Fig. 7.6 and Fig. 7.4 shows the change in uniformity clearly.

From the spatial filter the aberration of the components accumulates so that the wavefront shown in Fig. 7.7 at the final mirror is further aberrated. The second pass through the gain cells has further improved the uniformity.

Figure 7.8 gives a plot and Table 7.4 a tabulation of the values of Strehl ratio. Strehl ratio shows a general decrease because of component aberration. At three points the Strehl ratio improves. At the spatial filter, aberration is removed as discussed previously. The two other points of increase are due to the removal of diffracted light by apertures after the long propagation paths through the gain cells. This diffracted light does not have constant phase and therefore reduces the Strehl ratio. Saturated gain increases this effect as discussed in Chapter 4.

..FRINMAP 6.00E+00 9.00E+01

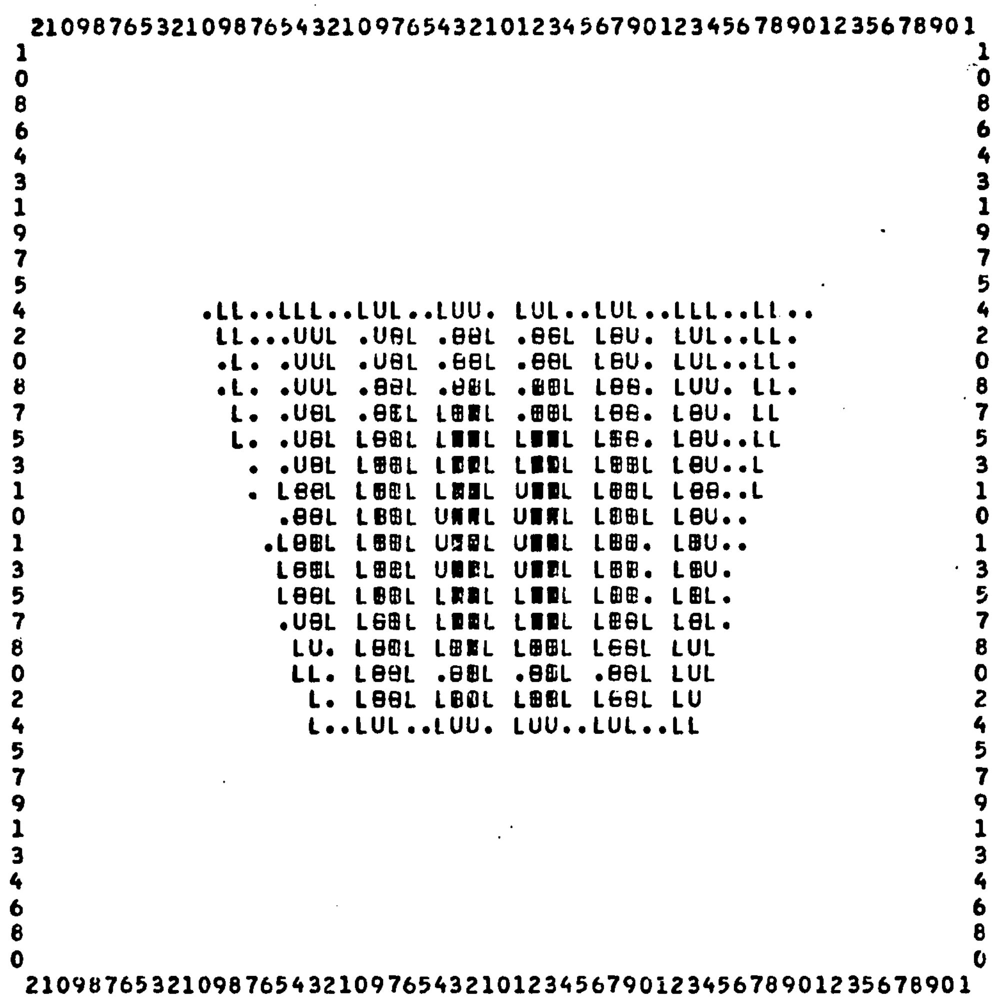

12 RELAY MIRROR 4

Figure 7.4. Interferogram prior to Gain Cells.

..FRINMAP 6.00E+00 9.00E+01

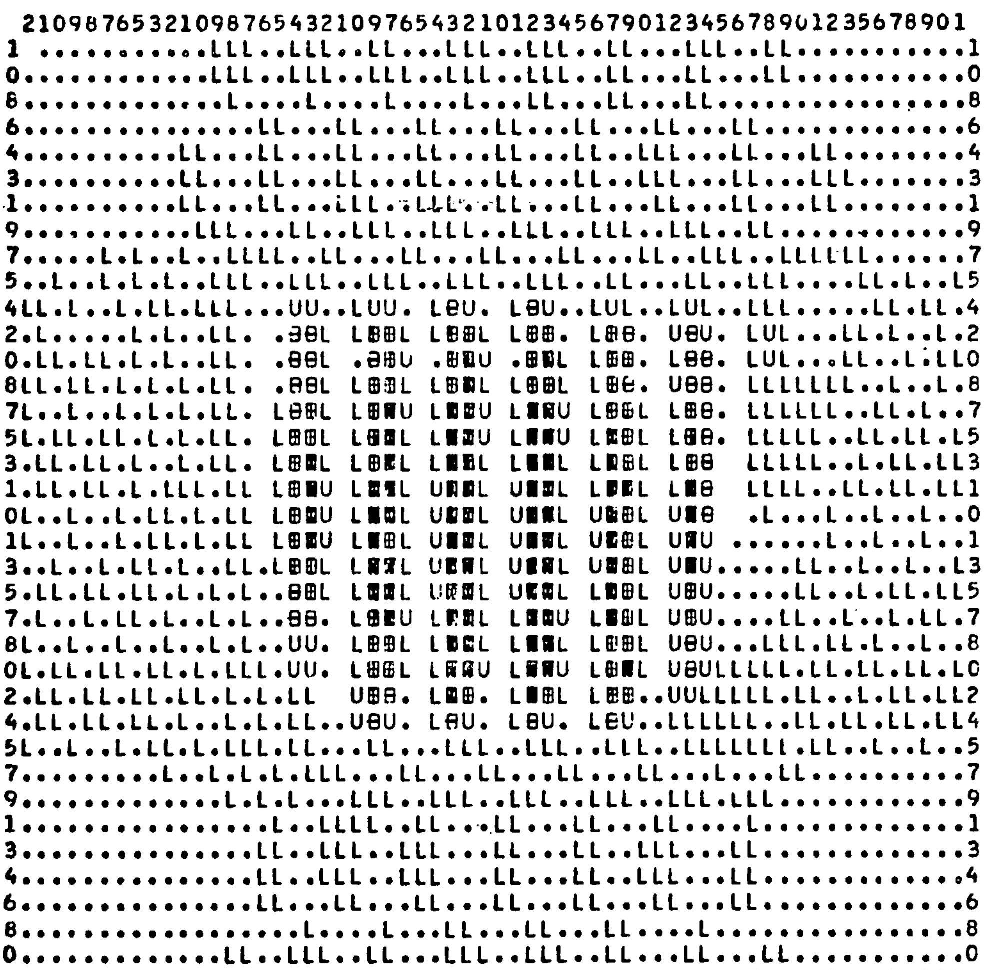

GAIN CELL 4

Figure 7.5. Interferogram after Gain Cells.

..FRINMAP 6.00E+00 9.00E+01

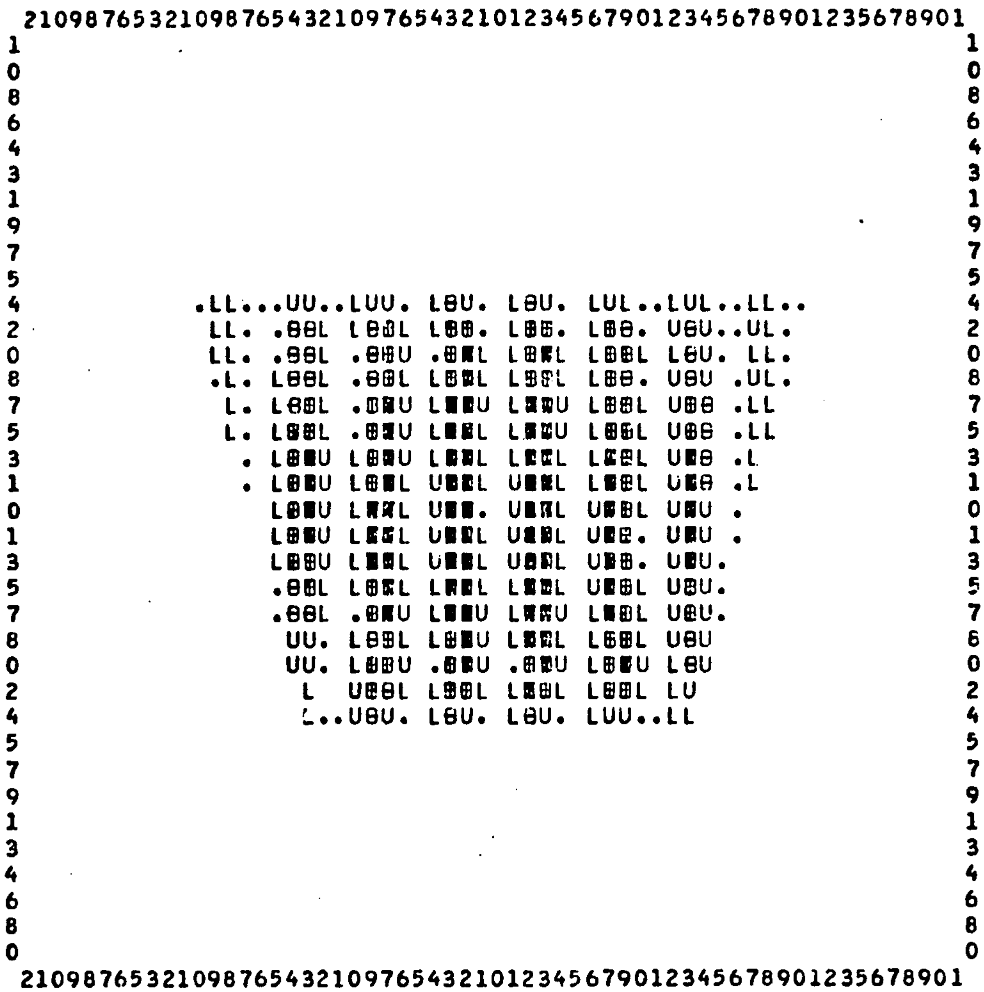

13 ABS WINDOW

Figure 7.6. Interferogram after Application of the Trapezoidal Aperture.

..FRINMAP 6.00E+00 9.00E+01

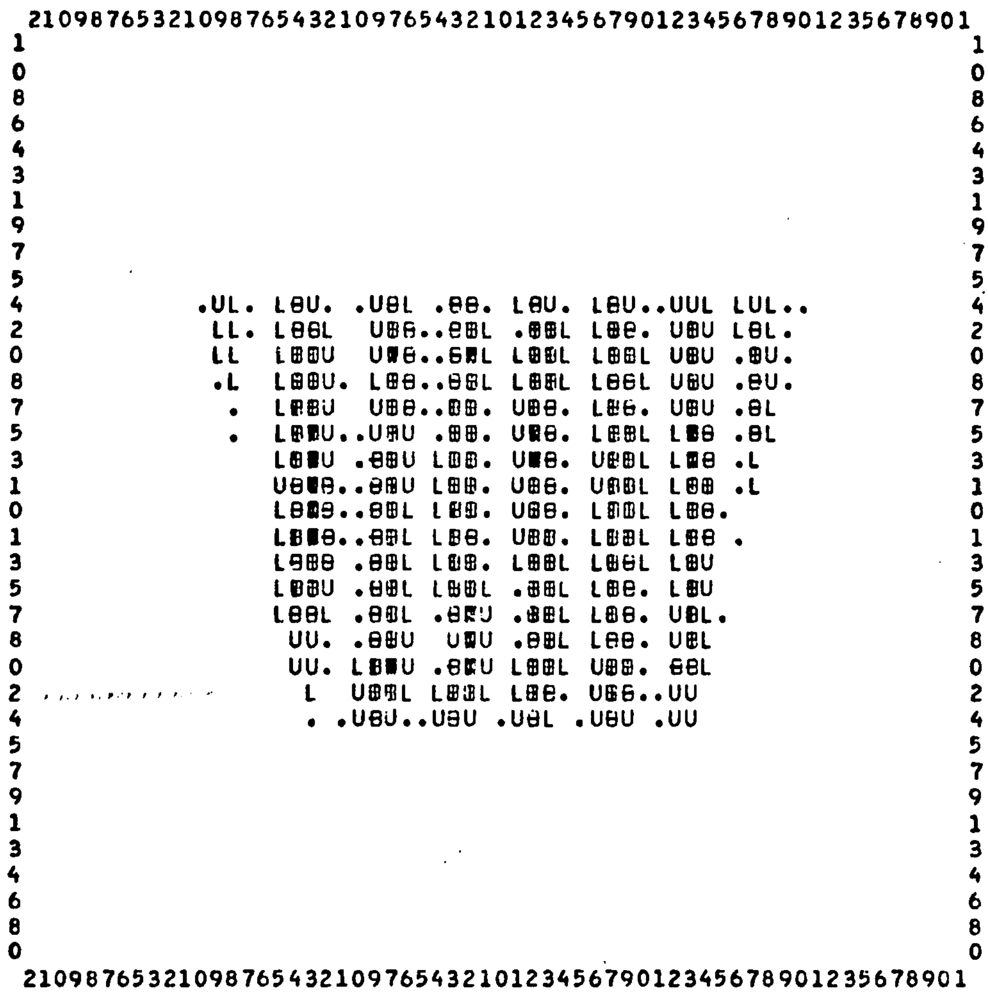

20 FOCUS MIRROR

Figure 7.7. Interferogram at Final Focusing Mirror.

```
..STRPLOT

STATION              STREHL RATIO

   .0   .1   .2   .3   .4   .5   .6   .7   .8   .9  1.0
   I....I....I....I....I....I....I....I....I....I....I
 1 I                                                 * INPUT PULSE
 2 I                                                *  1 VACUUM WINDOW
 3 I                                              *    2 TURNING MIRROR
 4 I                                             *     3 POLYHEDRON MIRR
 5 I                                            *      4 TURNING MIRROR
 6 I                                            *      5A TROMBONE 1
 7 I                                           *       5B TROMBONE 2
 8 I                                           *       5C TROMBONE 3
 9 I                                          *        6 FOCUS MIRROR
10 I                                                *  8 INPUT WINDOW
11 I                                                *  9 RELAY MIRROR 1
12 I                                               *   10 RELAY MIRROR 2
13 I                                               *   11 RELAY MIRROR 3
14 I                                               *   12 RELAY MIRROR 4
15 I                                            *      GAIN CELL 1
16 I                                           *       GAIN CELL 2
17 I                                          *        GAIN CELL 3
18 I                                         *         GAIN CELL 4
19 I                                             *     13 ABS WINDOW
20 I                                             *     SATURABLE ABS
21 I                                            *      14 BACK REFLECTOR
22 I                                           *       13 ABS WINDOW
23 I                                           *       GAIN CELL 4
24 I                                          *        GAIN CELL 3
25 I                                         *         GAIN CELL 2
26 I                                        *          GAIN CELL 1
27 I                                          *        15 OUTPUT WINDOW
28 I                                          *        16 PERISCOPE 1
29 I                                          *        17 PERISCOPE 2
30 I                                        *          18 TURN MIRROR
31 I                                       *           19 FOLD MIRROR
32 I                                     *             20 FOCUS MIRROR
   I....I....I....I....I....I....I....I....I....I....I
   .0   .1   .2   .3   .4   .5   .6   .7   .8   .9  1.0

STATION              STREHL RATIO
```

STATION	STREHL	TITLE
1	1.00000	INPUT PULSE
2	.99557	1 VACUUM WINDOW
3	.94433	2 TURNING MIRROR
4	.93805	3 POLYHEDRON MIRROR

Figure 7.8. Strehl Ratio Values along the Optical Train.

Table 7.4. Tabulation of Values of Strehl Ratio.

5	.91367	4 TURNING MIRROR
6	.90065	5A TROMBONE 1
7	.89484	5B TROMBONE 2
8	.88778	5C TROMBONE 3
9	.86849	6 FOCUS MIRROR
10	.98852	8 INPUT WINDOW
11	.98459	9 RELAY MIRROR 1
12	.97481	10 RELAY MIRROR 2
13	.96957	11 RELAY MIRROR 3
14	.96299	12 RELAY MIRROR 4
15	.90628	GAIN CELL 1
16	.89327	GAIN CELL 2
17	.87920	GAIN CELL 3
18	.85797	GAIN CELL 4
19	.93942	13 ABS WINDOW
20	.93965	SATURABLE ABS
21	.91636	14 BACK REFLECTOR
22	.88939	13 ABS WINDOW
23	.88119	GAIN CELL 4
24	.86910	GAIN CELL 3
25	.85154	GAIN CELL 2
26	.82584	GAIN CELL 1
27	.87385	15 OUTPUT WINDOW
28	.87407	16 PERISCOPE 1
29	.87303	17 PERISCOPE 2
30	.83056	18 TURN MIRROR
31	.80447	19 FOLD MIRROR
32	.77708	20 FOCUS MIRROR

Figure 7.9 shows a plot and Table 7.5 a tabulation of the total pulse energy. The energy increase during the two gain passes is evident. The spatial filter which removed essentially all the aberration accumulated prior to that point reduced the energy by only 37%. Because of the saturation of the amplifier, the final energy is quite insensitive to this energy loss.

The final energy is 1.21 kJ according to this calculation for one segment. For 72 segments the total energy is 87.4 kJ. This is 12.6% short of the planned 100 kJ and is in reasonable agreement with the planned value. The origin of the difference lies in the choice of amplifier characteristics being different from those used in obtaining the 100 kJ value. Since the primary purpose of the program is to study how system changes perturb the final pulse characteristics, this degree of accuracy is sufficient. Subsequent LOTS calculations done at Los Alamos using more accurate modeling of the system yield 100.8 kJ (Wolfe, Saxman, and Lawrence, 1979).

Calculations using LOTS have also been performed on the Helios (Viswanathan et al., 1978) and Gemini (Viswanathan et al., 1979) CO_2 laser fusion systems.

```
..ENGPLOT

STATION          ENERGY IN JOULES

   .0001 .001 .01  .1   1   10  100 1000 10000
    I....I....I....I....I....I....I....I....I
 1                        *                      INPUT PULSE
 2                        *                      1 VACUUM WINDOW
 3                        *                      2 TURNING MIRROR
 4                        *                      3 POLYHEDRON MIRROR
 5                        *                      4 TURNING MIRROR
 6                        *                      5A TROMBONE 1
 7                        *                      5B TROMBONE 2
 8                        *                      5C TROMBONE 3
 9                        *                      6 FOCUS MIRROR
10                       *                       8 INPUT WINDOW
11                       *                       9 RELAY MIRROR 1
12                       *                       10 RELAY MIRROR 2
13                      *                        11 RELAY MIRROR 3
14                      *                        12 RELAY MIRROR 4
15                         *                     GAIN CELL 1
16                            *                  GAIN CELL 2
17                               *               GAIN CELL 3
18                                 *             GAIN CELL 4
19                                *              13 ABS WINDOW
20                               *               SATURABLE ABS
21                               *               14 BACK REFLECTOR
22                               *               13 ABS WINDOW
23                                  *            GAIN CELL 4
24                                   *           GAIN CELL 3
25                                    *          GAIN CELL 2
26                                     *         GAIN CELL 1
27                                     *         15 OUTPUT WINDOW
28                                     *         16 PERISCOPE 1
29                                     *         17 PERISCOPE 2
30                                     *         18 TURN MIRROR
31                                     *         19 FOLD MIRROR
32                                     *         20 FOCUS MIRROR
    I....I....I....I....I....I....I....I....I
   .0001 .001 .01  .1   1   10  100 1000 10000

STATION          ENERGY IN JOULES


STATION ENERGY     TITLE

  1   3.7613E+00   INPUT PULSE
```

Figure 7.9. Laser Pulse Energy along the Optical Train.

Table 7.5. Tabulation of Total Energy Pulse.

2	3.6860E+00	1 VACUUM WINDOW
3	3.4405E+00	2 TURNING MIRROR
4	3.3912E+00	3 POLYHEDRON MIRROR
5	3.2999E+00	4 TURNING MIRROR
6	3.2550E+00	5A TROMBONE 1
7	3.2208E+00	5B TROMBONE 2
8	3.1871E+00	5C TROMBONE 3
9	3.1132E+00	6 FOCUS MIRROR
10	1.9743E+00	8 INPUT WINDOW
11	1.7532E+00	9 RELAY MIRROR 1
12	1.6146E+00	10 RELAY MIRROR 2
13	1.4956E+00	11 RELAY MIRROR 3
14	1.3746E+00	12 RELAY MIRROR 4
15	5.1676E+00	GAIN CELL 1
16	1.9448E+01	GAIN CELL 2
17	6.5559E+01	GAIN CELL 3
18	1.8772E+02	GAIN CELL 4
19	1.5486E+02	13 ABS WINDOW
20	9.2578E+01	SATURABLE ABS
21	9.0727E+01	14 BACK REFLECTOR
22	8.8912E+01	13 ABS WINDOW
23	2.5326E+02	GAIN CELL 4
24	5.6247E+02	GAIN CELL 3
25	9.6321E+02	GAIN CELL 2
26	1.4048E+03	GAIN CELL 1
27	1.3048E+03	15 OUTPUT WINDOW
28	1.2915E+03	16 PERISCOPE 1
29	1.2786E+03	17 PERISCOPE 2

Table 7.5. Continued.

30	1.2462E+03	18 TURN MIRROR
31	1.2260E+03	19 FOLD MIRROR
32	1.2137E+03	20 FOCUS MIRROR

CHAPTER 8

CONCLUSIONS AND RECOMMENDATIONS

Using Fresnel diffraction theory, linear system theory, the rate equation approximation, and appropriate experimental data, the LOTS computer program has been developed to serve as an optical engineering analysis tool for systems of the CO_2 laser fusion type. The capability of LOTS to treat the principal factors, i.e., nonlinear gain, saturable absorbers, diffraction propagation, spatial filters, and aberrated components has been shown in microcosm in Chapters, 3, 4, and 5. The capability to correctly model a complete system is demonstrated by the analysis of a preliminary design of the Antares system in Chapter 7. Application of LOTS to the Antares, Helios, and Gemini systems is described in the literature as noted in Chapters 6 and 7.

While the mathematical and physical theory which forms the basis of LOTS is well known, the application of this theory to an end-to-end calculation of a CO_2 laser fusion system was first done by means of the LOTS code in the summer of 1976.

Details of other propagation codes--developed for CW laser systems--are not always available because of company proprietary restrictions. It is, however, the author's belief that in addition to being specifically designed for the pulsed CO_2 laser fusion systems, LOTS is unique in its versatility, user-oriented command structure, and efficient use of computer central memory and central processor time.

The author is aware of no prior use of smoothed random wavefronts to simulate components known only by their specification values in this type of analysis.

The theory of Fresnel diffraction for noncollimated beams has been presented in a more clear and concise form than previously. See, for example, Sziklas and Siegman (1975). The simple guidelines and error calculations for numerical diffraction calculations presented in Chapter 3 are considered to be an improvement as well.

To further extend the capabilities of LOTS the author recommends the completion of the expandable matrix version of LOTS. The expandable version of LOTS allows the user to define independently the size of the matrix and the size of the high speed memory allocated for matrix storage. Sophisticated routines have been developed to make the most efficient use of CPU and IO time. Data transfer is handled by special utility routines which may be readily changed to adapt to operational system differences. At its current stage of completion the basic data handling routines, matrix transpose algorithm, random wavefront formation by convolution, and interpolation routines are operational. About half the functions of LOTS remain to be modified to use the new data transfer routines. In addition, data display routines for film and electrostatic plotter should be developed.

APPENDIX A

EFFECTIVE PROPAGATION DISTANCE

With the conventions shown in Fig. 3.4, the distribution at the center of curvature is

$$p_0(x_0,y_0) = \frac{\exp\left(-j\,\frac{\kappa r_0^2}{2z_1}\right)}{-j\lambda z_1} \iint_{-\infty}^{\infty} p_1(x_1,y_1)\,\exp\left(-j\,\frac{\kappa r_1^2}{2z_1}\right)$$

$$\times\,\exp\left[j\,\frac{2\pi}{\lambda z_1}\,(x_1x_0+y_1y_0)\right]\,dx_1dy_1\,. \qquad \text{(A.1)}$$

In terms of $p_0(x_0,y_0)$ the distribution at Plane 2 is

$$p_2(x_2,y_2) = \frac{\exp\left(-j\,\frac{\kappa r_2^2}{2z_2}\right)}{j\lambda z_2} \iint_{-\infty}^{\infty} p_0(x_0,y_0)\,\exp\left(j\,\frac{\kappa r_0^2}{2z_2}\right)$$

$$\times\,\exp\left[-j\,\frac{2\pi}{\lambda z_2}\,(x_2x_0+y_2y_0)\right]\,dx_0dy_0\,. \qquad \text{(A.2)}$$

Define $f(x,y)$ such that

$$p(x,y) = f(x,y)\,\exp\left(j\,\frac{\kappa r^2}{2z}\right)\,. \qquad \text{(A.3)}$$

With Eq. (A.3), Eq. (A.2) becomes

$$f_2(x_2,y_2) = \frac{1}{j\lambda z_2} \iint_{-\infty}^{\infty} p_0(x_0,y_0)\,\exp\left(j\,\frac{\kappa r_0^2}{2z_2}\right)$$

$$\times\,\exp\left[-j\,\frac{2\pi}{\lambda z_2}\,(x_2x_0+y_2y_0)\right]\,dx_0dy_0 \qquad \text{(A.4)}$$

and Eq. (A.1) becomes

$$p_0(x_0,y_0) = \frac{\exp\left(-j\,\frac{\kappa r_0^2}{2z_1}\right)}{-j\lambda z_1} \iint_{-\infty}^{\infty} f_1(x_1,y_1)$$

$$\times \exp\left[j\,\frac{2\pi}{\lambda z_1}\,(x_1x_0+y_1y_0)\right] dx_1dy_1 . \tag{A.5}$$

Combining Eqs. (A.4) and (A.5),

$$f_2(x_2,y_2) = \frac{1}{\lambda^2 z_1 z_2} \iint_{-\infty}^{\infty} \exp\left[j\,\frac{\kappa r_0^2}{2}\left(\frac{1}{z_2} - \frac{1}{z_1}\right)\right]$$

$$\times \left\{\iint_{-\infty}^{\infty} f_1(x_1,y_1)\, \exp\left[j\,\frac{2\pi}{\lambda z_1}\,(x_1x_0+y_1y_0)\right] dx_1dy_1\right\}$$

$$\exp\left[-j\,\frac{2\pi}{\lambda z_2}\,(x_2x_0+y_2y_0)\right] dx_0dy_0 . \tag{A.6}$$

Defining scaled coordinates $\tilde{x}_2$ and $\tilde{y}_2$,

$$\tilde{x}_2 = \frac{z_1}{z_2}\,x_2, \quad \tilde{y}_2 = \frac{z_1}{z_2}\,y_2 . \tag{A.7}$$

The spatial frequency variables are

$$\xi = -\frac{x_0}{\lambda z_1}, \quad \eta = -\frac{y_0}{\lambda z_1}, \quad \rho^2 = \varepsilon^2 + \eta^2 . \tag{A.8}$$

By defining a new propagation variable the quadratic phase factor becomes

$$\exp\left[j\,\frac{\kappa r_0^2}{2}\left(\frac{1}{z_2} - \frac{1}{z_1}\right)\right] = \exp\left[-j\pi\lambda z_e \rho^2\right], \tag{A.9}$$

where z_e is

$$z_e \equiv (z_2-z_1)\,\frac{z_1}{z_2} . \tag{A.10}$$

Equation (A.6) becomes

$$f_2(\tilde{x}_2,\tilde{y}_2) = \frac{z_1}{z_2}\iint_{-\infty}^{\infty} \exp(-j\pi\lambda z_e\rho^2)$$
$$\times\left\{\iint_{-\infty}^{\infty} f_1(x_1,y_1)\exp\left[-j2\pi(\xi x_1+\xi y_1)\right]dx_1dy_1\right\}$$
$$\times \exp\left[j2\pi(\tilde{x}_2\xi+\tilde{y}_2\eta)\right]d\xi d\eta. \quad \text{(A.11)}$$

Dropping the tildas and using the FF notation for Fourier transforms, Eq. (A.11) is written

$$f_2(x_2,y_2) = FF^{-1}\{H(\xi,\eta;z_e)FF\left[f_1(x_1,y_1)\right]\}$$
$$H(\xi,\eta;z_e) = \frac{z_1}{z_2}\exp\left[-j\pi\lambda z_e(\xi^2+\eta^2)\right]. \quad \text{(A.12)}$$

The Fourier transform of the equation is

$$F_2(\xi,\eta) = F_1(\xi,\eta)H(\xi,\eta;z_e). \quad \text{(A.13)}$$

Equation (A.13) expresses the near field diffraction process for collimated or noncollimated beams.

APPENDIX B

PROPERTIES OF THE DISCRETE FOURIER TRANSFORM

For reference, several properties of the DFT are listed in Table B.1 along with the corresponding continuous Fourier transform (CFT) expressions.

Table B.1. DFT and CFT Expressions.

Forward transform

$$H\left(\frac{m}{NT}, \frac{n}{NT}\right) = T^2 \sum_k \sum_\ell h(kT, \ell T) \exp\left[-j2\pi\left(\frac{km+\ell n}{N}\right)\right] \tag{B.1}$$

$$H(\xi,\eta) = \iint_{-\infty}^{\infty} h(x,y) \exp[-j2\pi(\xi x+\eta y)]dxdy$$

Inverse transform

$$h(kT,\ell T) = \frac{1}{N^2T^2} \sum_m \sum_n H\left(\frac{m}{NT}, \frac{n}{NT}\right) \exp\left[j2\pi\left(\frac{km+\ell n}{N}\right)\right] \tag{B.2}$$

$$h(x,y) = \iint_{-\infty}^{\infty} H(\xi,\eta) \exp[j2\pi(\xi x+\eta y)]d\xi d\eta$$

Convolution in the spatial domain

$$g(kT,\ell T) = T^2 \sum_o \sum_p f(oT,pT)h(kT-oT,\ell T-pT) \tag{B.3}$$

$$g(x,y) = \iint_{-\infty}^{\infty} f(\alpha,\beta)h(x-\alpha,y-\beta)d\alpha d\beta$$

Table B.1. Continued

Convolution in the frequency domain	
$G\left(\frac{m}{NT}, \frac{n}{NT}\right) = \frac{1}{N^2T^2} \sum_o \sum_p F\left(\frac{o}{NT}, \frac{p}{NT}\right) H\left(\frac{m-o}{NT}, \frac{n-p}{NT}\right)$	(B.4)
$G(\xi,\eta) = \iint_{-\infty}^{\infty} F(\alpha,\beta)H(\xi-\alpha,\eta-\beta)d\alpha d\beta$	
Orthogonality of basis functions	
$\frac{1}{N^2T^2} \sum_m \sum_n \exp\left[j2\pi\left(\frac{km+\ell n}{NT}\right)\right] \exp\left[-j2\pi\left(\frac{om+pn}{NT}\right)\right] = \delta(kT-oT, \ell T-pT)$	(B.5)
$\iint_{-\infty}^{\infty} \exp[j2\pi(\xi x+\eta y)] \exp[-j2\pi(\xi x_1+\eta y_1)]d\xi d\eta = \delta(x-x_1, y-y_1)$	
Delta function combing property	
$T^2 \sum \sum f(oT,pT)\delta(kT-oT,\ell T-pT) = f(kT,\ell T)$	(B.6)
$\iint_{-\infty}^{\infty} f(\alpha,\beta)\delta(x-\alpha,y-\beta)d\alpha d\beta = f(x,y)$	
Parseval's theorem	
$T^2 \sum_k \sum_\ell \lvert f(kT,\ell T)\rvert^2 = \frac{1}{N^2T^2} \sum_m \sum_n \left\lvert H\left(\frac{m}{NT}, \frac{n}{NT}\right)\right\rvert^2$	(B.7)
$\iint_{-\infty}^{\infty} \lvert f(x,y)\rvert^2 dxdy = \iint_{-\infty}^{\infty} \lvert F(\xi,\eta)\rvert^2 d\xi d\eta$	

APPENDIX C

SOME USEFUL DIFFRACTION APPROXIMATIONS

In Chapter 3 approximations for the intensity in the Airy pattern, the radial excluded energy in the Airy pattern, and the intensity in the shadow region of the circular near-field diffraction pattern are used. These approximations are developed from the asymptotic approximations for Bessel functions of the first kind (Abramowitz and Stegun, 1964, p. 364)

$$J_n(x) \simeq \left(\frac{2}{\pi x}\right)^{\frac{1}{2}} \cos\left(x - \frac{n\pi}{2} - \frac{\pi}{4}\right) . \tag{C.1}$$

This is a reasonably good approximation for $x > n$.

Airy Pattern Intensity

The normalized Airy pattern is

$$I(a,\rho) = \left[2\,\frac{J_1(2\pi a\rho)}{2\pi a\rho}\right]^2 , \tag{C.2}$$

where a is the aperture radius and ρ is the spatial frequency. To describe the envelope of this pattern for $a\rho > 1$ the cosine in (A.1) is taken to have unit value giving,

$$I(a,\rho) = \frac{1}{\pi^4 a^3 \rho^3} . \tag{C.3}$$

Excluded Energy

The energy outside a given radius in the Airy pattern is

$$I(a,\rho) = J_0{}^2(2\pi a\rho) + J_1{}^2(2\pi a\rho).$$

Taking the approximation of Eq. (C.1),

$$J_0{}^2(x) = \frac{2}{\pi x}\cos^2\left(x - \frac{\pi}{4}\right), \tag{C.4}$$

$$J_1{}^2(x) = \frac{2}{\pi x}\cos^2\left(x - \frac{3\pi}{4}\right), \tag{C.5}$$

and

$$I(a,\rho) \simeq \frac{1}{\pi^2 a\rho}. \tag{C.6}$$

Shadow Intensity of Circular Diffraction Pattern

The normalized Fresnel diffraction pattern of a circular aperture illuminated by a normally incident plane wave is (Born and Wolf, 1959, p. 434)

$$I(s,t) = \left[U_1{}^2(s,t) + U_2{}^2(s,t)\right] \tag{C.7}$$

where

a = aperture radius

$s = 2\pi(a^2/\lambda z) = 2\pi F$

$t = 2\pi(ar/\lambda z) = 2\pi F(r/a)$

F = Fresnel number

U_k = kth Lommel function.

The Lommel function is defined as

$$U_k(s,t) \geq \sum_{n=0}^{\infty} (-1)^n \left(\frac{s}{t}\right)^{2n+k} J_{2n+k}(t). \tag{C.8}$$

Equation (C.1) can be used to approximate $J_{2n+k}(t)$ only if $t > 2n + k$. Since $t \simeq 2\pi F$, this condition is satisfied for small values of n for U_1 and U_2. By moving far enough into the geometrical shadow the terms for which t is less than 2n + k may be made negligible. The first step is to determine how far into the shadow it is necessary to be to make the approximation of Eq. (C.1). Let ε be an allowable upper limit on the negligible terms. Then the requirement is expressed as

$$\left| \left(\frac{s}{t}\right)^{2n+k} J_{2n+k}(t) \right| < \varepsilon \tag{C.9}$$

for $t < 2n + k$. The Bessel function takes on a range of values

$$0 \leq \left| J_{2n+k}(t) \right| \leq 1. \tag{C.10}$$

Then Eq. (C.9) will be met if

$$\left(\frac{s}{t}\right)^{t} < \varepsilon. \tag{C.11}$$

The region of interest is the geometrical shadow where $s < t$. Then Eq. (A.9) is satisfied if

$$\left(\frac{s}{t}\right)^{t} < \varepsilon. \tag{C.12}$$

Taking the natural logarithm of Eq. (A.12)

$$s \ln \frac{s}{t} < \ln \varepsilon. \tag{C.13}$$

Since we are examining the lower bound of validity for t, the small argument series expansion for natural logarithms may be used (Abramowitz and Stegun, 1964)

$$\ln(1+z) = z - \frac{1}{2}z^2 + \frac{1}{3}z^3 - \ldots$$

$$(|z| \leq 1 \text{ and } z \neq 1).$$

To the first term Eq. (A.14) applied to Eq. (A.13) is

$$s \ln\left(1 + \frac{s-t}{t}\right) = -\frac{t-s}{s}.$$

Recalling the $s = 2\pi F$, the requirement becomes

$$\frac{t-s}{s} > \frac{\ln \varepsilon}{-2\pi F}. \tag{C.15}$$

Assuming that $\ln \varepsilon \simeq -2\pi$ is a tolerable error limit, then the requirement for the Bessel function approximation of (C.1) is

$$\frac{t-s}{s} > \frac{1}{F}. \tag{C.16}$$

In terms of the aperture radius, a, the distance, Δr, into the shadow region is

$$\Delta r > \frac{a}{F}. \tag{C.17}$$

Assuming the requirement of Eq. (C.15) is met

$$U_k(s,t) \simeq \sum_{n=0}^{\infty} (-1)^n \left(\frac{s}{t}\right)^{2n+k} \left(\frac{2}{\pi t}\right)^{\frac{1}{2}} \cos\left(t - (2n+k)\frac{\pi}{2} - \frac{\pi}{4}\right). \tag{C.18}$$

But,

$$(-1)^n \cos\left(t - n\pi - \frac{k\pi}{2} - \frac{\pi}{4}\right) = \cos\left(t - \frac{k\pi}{2} - \frac{\pi}{4}\right). \tag{C.19}$$

Then

$$U_k(s,t) \simeq \left(\frac{s}{t}\right)^k \cos\left(t - \frac{k\pi}{2} - \frac{\pi}{4}\right)\left(\frac{2}{\pi t}\right)^{\frac{1}{2}} \sum_{n=0}^{\infty} \left(\frac{s}{t}\right)^{2n} \tag{C.20}$$

and

$$U_k(s,t) \simeq \frac{(s/t)^k}{[1 - (s/t)^2]^2} \left(\frac{2}{\pi t}\right)^{\frac{1}{2}} \cos\left(t - \frac{k\pi}{2} - \frac{\pi}{4}\right). \quad (C.30)$$

The normalized diffraction pattern is

$$I(s,t) = [U_1{}^2(s,t) + U_2{}^2(s,t)]. \quad (C.31)$$

Employing Eq. (C.30),

$$I(s,t) \simeq \frac{2}{\pi t} \frac{(s/t)^2 \cos^2[t-(\pi/4)] + (s/t)^4 \sin^2[t-(\pi/4)]}{[1 - (s/t)^2]^2}$$

As t increases the envelope of this functions becomes

$$I(s,t) \simeq \frac{2}{\pi t} \frac{(s/t)^2}{[1 - (s/t)^2]^2} . \quad (C.33)$$

Recalling that $s = 2\pi F$ and $t = 2\pi F(r/a)$, the normalized intensity in the shadow is

$$I(a,r) = \frac{1}{\pi^2 F} \frac{(a/r)^3}{[1 - (a/r)^2]^2} . \quad (C.34)$$

APPENDIX D

RANDOM WAVEFRONT CONSTRUCTION

The methods used for random wavefront construction are drawn from the theory of random processes (see for example Beckmann, 1967). For consistency with this theoretical approach, notation in this appendix differs somewhat from that used elsewhere in this dissertation.

Capital letters are used to denote variables and lower case letters to denote the values or realizations assumed by that variable. For example, let F be a random variable assuming values f. The probability density will be written P(f). If a random variable is a function of some parameter, i.e., F(x,y) where x,y are the usual spatial coordinates, it is called a random process. The random wavefront construction process is a random process creating specific wavefronts of the form f(x,y). The process F(x,y) has probability distribution P(f;x,y).

In this notation, the kth moment of a two-dimensional random process, F(x,y), is

$$m_k[F(x,y)] = \langle F(x,y)^k \rangle = \int f^k P(f;x,y)\,df \tag{D.1}$$

and the central moment is

$$\begin{aligned} M_k[F(x,y)] &= \langle [F(x,y) - \langle F(x,y) \rangle]^k \rangle \\ &= \int [f - \langle F(x,y) \rangle]^k P(f;x,y)\,df. \end{aligned} \tag{D.2}$$

For two random processes there exist joint probability distributions and joint moments. Only the first joint moment, the autocorrelation function, is of concern in this discussion. In two dimensions the autocorrelation function is

$$R(x_1,y_1,x_2,y_2) = \langle F(x_1,y_1)F(x_2,y_2)\rangle$$

$$= \iint f_1 f_2 P(f_1,f_2;x_1,y_1,x_2,y_2)\,df_1 df_2. \quad (D.3)$$

In the case of a stationary process, i.e., one whose statistics are independent of spatial coordinates, this may be written

$$R(\Delta x,\Delta y) = \langle F(x,y)F(x+\Delta x,y+\Delta y)\rangle. \quad (D.4)$$

Construction Method

In Chapter 5 arguments were made that an autocorrelation function which was constant over the surface was reasonable to assume for the optics in the laser fusion system. One method of creating a random process with the required autocorrelation process is to generate a delta-correlated random process $G(x,y)$ and then smooth the process with a function $s(x,y)$. The term delta-correlated means

$$R(\Delta x,\Delta y) = \sigma^2\delta(\Delta x,\Delta y). \quad (D.5)$$

The random function generator in FORTRAN provides a convenient means of generating $G(x,y)$. This function has probability distribution $P(x)$ such that

$$P(x) = \begin{cases} 1 & 0 \le x \le 1 \\ 0 & x > 1,\ x < 0 \end{cases}. \quad (D.6)$$

If the results of calls to the random function generator are denoted Z_i, then G(x,y) may be formed by

$$G(x,y) = Z_1 - Z_2. \tag{D.7}$$

This ensures a zero mean. Because of the convolution of probability functions, the probability distribution of Eq. (D.7) has a triangular shape. This feature may be exploited if a nearly Gaussian probability distribution is desired by using more random calls

$$G(x,y) = Z_1 - Z_2 + Z_3 - Z_4 \ldots. \tag{D.8}$$

The repeated self-convolutions converge very quickly to the Gaussian form. This is shown pictorially in Gaskill (1978).

The random wavefronts are constructed by smoothing with s(x,y) such that

$$F(x,y) = \iint_{-\infty}^{\infty} G(\alpha,\beta)\, s(x-\alpha, y-\beta)\, d\alpha\, d\beta. \tag{D.9}$$

The mean is

$$\begin{aligned} \langle F(x,y)\rangle &= \left\langle \iint_{-\infty}^{\infty} G(\alpha,\beta)\, s(x-\alpha, y-\beta)\, d\alpha\, d\beta \right\rangle \\ &= \langle G(x,y)\rangle \iint_{-\infty}^{\infty} s(x,y)\, dx\, dy. \end{aligned} \tag{D.10}$$

The autocorrelation function is

$$
\begin{aligned}
R(\Delta x,\Delta y) &= \langle F(x,y)F(x+\Delta x,y+\Delta y)\rangle \\
&= \left\langle \iiiint_{-\infty}^{\infty} G(\alpha,\beta)s(x-\alpha,y-\beta)G(\gamma,\delta)s(x+\Delta x-\gamma,y+\Delta y-\delta)\right. \\
&\qquad \left. d\alpha d\beta d\gamma d\delta \right\rangle \\
&= \iiiint_{-\infty}^{\infty} \langle G(\alpha,\beta)G(\gamma,\delta)\rangle s(x-\alpha,y-\beta) \\
&\qquad s(x+\Delta x-\gamma,y+\Delta y-\delta)\,d\alpha d\beta d\gamma d\delta . \qquad \text{(D.11)}
\end{aligned}
$$

But G(x,y) is delta-correlated with zero mean, i.e.,

$$
G(\alpha,\beta)G(\gamma,\delta) = \begin{cases} 0 & \alpha \neq \gamma,\ \beta \neq \delta \\ \sigma^2 & \alpha = \beta,\ \beta = \delta \end{cases} .
$$

Then the four-dimensional integral reduces to a two-dimensional integral due to the combing property of the delta function

$$
\begin{aligned}
R(\Delta x,\Delta y) &= \sigma^2 \iint_{-\infty}^{\infty} s(\alpha,\beta)s(\alpha+\Delta x,\beta+\Delta y)\,d\alpha d\beta \\
&= \sigma^2 s(\Delta x,\Delta y) \bigstar\bigstar\, s(\Delta x,\Delta y) \qquad \text{(D.12)}
\end{aligned}
$$

where $\bigstar\bigstar$ represents two-dimensional autocorrelation. The autocorrelation function of F(x,y) has the same form as the autocorrelation function of s(x,y).

Numerical Considerations in Smoothing

Because of the linear nature of the smoothing operation, it may be done by convolution as in Eq. (D.9) or by the frequency space operation

$$\tilde{F}(\xi,\eta) = \tilde{G}(\xi,\eta)\tilde{s}(\xi,\eta) \tag{D.13}$$

where the tilda denotes the Fourier transform. This technique is called the transfer function approach. Usually the transfer function method is preferred because of the efficiency of the FFT algorithm and because the operation can be done in place, i.e., without requiring additional computer memory. However, in this application other techniques are competitive. To compare techniques it is necessary to consider the relative speeds of various operations. These speeds, of course, vary considerably on different computers but the relative speeds are reasonably constant. Table D.1 shows relative times for the operations needed for this analysis.

Table D.1. Relative Times of Computer Operations.

Operation	Time x 10^{-6} units
Addition	1
Multiplication	5
Exponentiation	150
Random number generation	25

For the CDC 6400 the unit is about 1.0. For the Cyber 175 it is about 0.1, and for the CDC 6600 it is about 0.5. For the analysis the time of other operations is ignored.

The calculations will be based on the scheme shown in Fig. D.1, with the smoothing function radius J = 10 and the matrix width N = 64. It is assumed that the smoothing function is a Gaussian distribution.

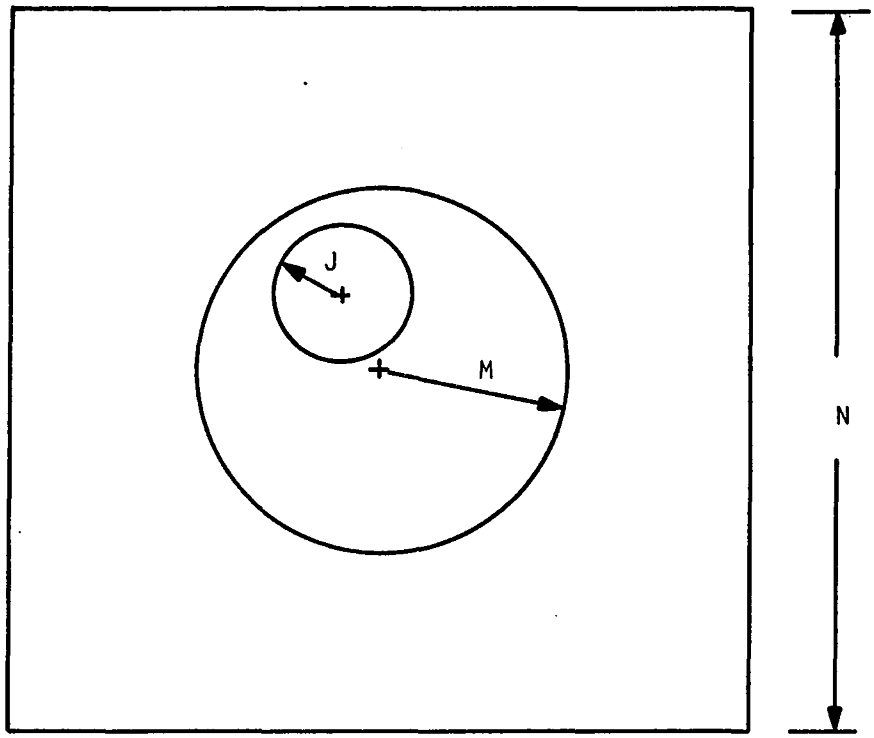

Figure D.1. Typical Numerical Configuration for Generation of Random Wavefronts.

A pupil of radius M is embedded in a square array of dimension N. The smoothing function is of radius J.

For the transfer function technique the operating time is shown in Table D.2. The two-dimensional FFT involves 2N one-dimensional transforms taking $N \log_2 N$ multiplications. In the spectral weighting only an octant of the rotationally symmetrical exponential function need be computed.

Table D.2. Transfer Function Operational Time.

Operation	Computer events	Time
Random number generation	$25\ N^2 \times 10^{-6}$	0.10
FFT (two dimensional)	$5\ (2N \times \log_2 N) \times 10^{-6}$	0.25
Spectral weighting	$150\ (N^2/8) \times 10^{-6}$	0.08
FFT (two dimensional)	$5\ (2N^2 \log_2 N) \times 10^{-6}$	0.25
		0.68

This procedure can be simplified somewhat. The function $\tilde{G}(\xi,\eta)$ may be constructed directly saving the time for one of the Fourier transformations. $G(\xi,\eta)$ must be constructed to be Hermitian to have $G(x,y)$ strictly real. This is most efficiently done by only filling the positive half plane with random phasors and taking the real part of the inverse transform

$$G(x,y) = 2\mathrm{Re}\left\{\int_{-\infty}^{\infty}\int_{0}^{\infty} \tilde{G}(\xi,\eta)\ \exp[j2\pi(\xi x+\eta y)]\,d\xi\,d\eta\right\} \qquad \text{(D.14)}$$

and the smoothed function F(x,y) is

$$F(x,y) \;=\; 2\mathrm{Re}\left\{ \int_{-\infty}^{\infty}\int_{0}^{\infty} \tilde{G}(\xi,\eta)\tilde{s}(\xi,\eta)\ \exp\ j2\pi(\xi x+\eta y)\ d\xi d\eta\ .\right.$$

In addition to being Hermitian, $\tilde{G}(\xi,\eta)$ must be a phasor uniformly distributed in phase called a UDP phasor. That is, if $\tilde{G}(\xi,\eta)$ is written in polar form

$$\tilde{G}(\xi,\eta) \;=\; A(\xi,\eta)\ e^{i\theta(\xi,\eta)}, \tag{D.15}$$

then $\theta(\xi,\eta)$ must have a uniform probability distribution from 0 to 2π. This is a requirement for F(x,y) to be stationary. Consider the variance where F(x,y) has zero mean

$$\begin{aligned}<F(x,y)^2> \;=\; <\iiiint_{-\infty}^{\infty} & \mathrm{Re}\left\{\tilde{s}(\alpha,\beta)\tilde{G}(\alpha,\beta)\ \exp[j2\pi(\alpha x+\beta y)]\right\} \\ & \mathrm{Re}\left\{\tilde{s}(\gamma,\delta)\tilde{G}(\gamma,\delta)\ \exp[j2\pi(\gamma x+\delta y)]\right\} \\ & d\alpha d\beta d\gamma d\delta>.\end{aligned} \tag{D.16}$$

Because $\tilde{G}(\xi,\eta)$ is delta-correlated this may be simplified to

$$\begin{aligned}<F(x,y)^2> \;=\; <\iint_{-\infty}^{\infty} & \Big(\mathrm{Re}\Big\{\tilde{s}(\alpha,\beta)\tilde{G}(\xi,\eta) \\ & \exp[j\pi(\xi x+\eta y)]\Big\}\Big)^2 d\xi d\eta>.\end{aligned} \tag{D.17}$$

The x,y dependence in the Fourier kernel will, in general, cause the variance to be a function of x and y. For example, consider $\tilde{G}(\xi,\eta)$ strictly real

$$\begin{aligned}<F(x,y)^2> \;=\; \iint_{-\infty}^{\infty} & \tilde{s}^2(\xi,\eta)<G(\xi,\eta)^2> \\ & \cos^2[2\pi(\xi x+\eta y)]d\xi d\eta.\end{aligned} \tag{D.18}$$

Making the substitution $2\cos^2\theta = 1 + \cos 2\theta$, $\xi' = 2\xi$, and $\eta' = 2\eta$; this expression becomes

$$\langle F(x,y)\rangle = \frac{1}{2}\langle G(\xi,\eta)^2\rangle\left[\iint_{-\infty}^{\infty} \tilde{s}(\xi,\eta)^2 d\xi d\eta + \frac{1}{4}\iint_{-\infty}^{\infty} \tilde{s}\left(\frac{\xi'}{2}, \frac{\eta'}{2}\right)^2 \cos 2\pi(\xi' x+\eta' y) d\xi' d\eta'\right]. \tag{D.19}$$

For a real, even smoothing function

$$R(x,y) = \iint \tilde{s}(\xi,\eta)^2 \cos[2\pi(\xi x+\eta y)] d\xi d\eta. \tag{D.20}$$

Then Eq. (D.17) becomes

$$\langle F(x,y)^2\rangle = \frac{1}{2}\langle\tilde{G}(\xi,\eta)\rangle[R(0,0) + R(2x,2y)]. \tag{D.21}$$

The function F(x,y) is nonstationary with respect to the variance. This occurs because the Fourier kernel becomes nearly constant for $x \simeq 0$, $y \simeq 0$ and the contribution to the variance is twice the value where the Fourier kernel is oscillating rapidly.

If $\tilde{G}(\xi,\eta)$ is a UDP phasor, then a phasor $\tilde{G}'(\xi,\eta)$ defined by

$$\tilde{G}'(\xi,\eta) = \tilde{G}(\xi,\eta) \exp[j2\pi(\xi x+\eta y)] \tag{D.22}$$

is also a UDP phasor. The phase has merely been rotated. Therefore, the Fourier kernel may be dropped from Eq. (D.17). Again, assuming s(x,y) real and even, the variance is

$$\langle F(x,y)^2\rangle = \langle\{\mathrm{Re}[\tilde{G}(\xi,\eta)]\}^2\rangle \iint_{-\infty}^{\infty} \tilde{s}(\xi,\eta)^2 d\xi d\eta. \tag{D.23}$$

For $\tilde{G}(\xi,\eta)$ written in polar form this may be written in terms of the modulus A(s,)

$$\langle F(x,y)^2\rangle = \frac{1}{2}\langle A(\xi,\eta)^2\rangle \iint_{-\infty}^{\infty} \tilde{s}(\xi,\eta)^2 d\xi d\eta \tag{D.24}$$

which may be rewritten by Parsevel's theorem as

$$\langle F(x,y)^2\rangle = \frac{1}{2}\langle A(\xi,\eta)^2\rangle \iint_{-\infty}^{\infty} s(x,y)dxdy. \tag{D.25}$$

If s(x,y) is relatively slowly varying with respect to the sample spacing, then the probability density function of F(x,y) will be Gaussian to an excellent degree of approximation no matter how $A(\xi,\eta)$ is distributed.

$\tilde{G}(\xi,\eta)$ may be generated as a UDP phasor by

$$\tilde{G}(\xi,\eta) = {}_1 \exp(j2\pi {}_2), \tag{D.26}$$

where z_1 and z_2 are independent random numbers. This operation takes about 200×10^{-6} units.

Alternatively $\tilde{G}(\xi,\eta)$ may be created by

$$\tilde{G}(\xi,\eta) = (Z_1 - Z_2 + Z_3 - Z_4 \ldots Z_n)$$
$$+ j(Z_n - Z_{n+1} + Z_{n+2} - Z_{n+3} \cdots Z_{2n}). \tag{D.27}$$

For n = 4 this operation will yield $\tilde{G}(\xi,\eta)$ Gaussian distributed in modulus and uniform in phase. The computational time is essentially the same as for Eq. (D.26) however.

The computational time for creation of this modified transfer function technique is shown in Table D.3.

Table D.3. Modified Transfer Function Technique.

Operation	Computer events	Time
$\tilde{G}(\xi,\eta)\tilde{s}(x,y)$	$[200(N^2/2)+150(N^2/8)]\times10^{-6}$	0.49
FFT	$5(2N^2 \log_2 N)\times10^{-6}$	0.25
		0.74

Because of the necessity to use UDP phasors, this operation is slower than the original transfer function approach.

In both the transfer function approach and the modified transfer function approach, a major part of the computational time was devoted to computing exponentials. Because the width of the smoothing function is generally small with respect to the matrix size, it is worth considering the convolution approach. Table D.4 shows the computational times for the example of N = 64, J = 10. The increase in the number of multiplications far outweighs the reduction in exponentiations.

Table D.4. Convolution Smoothing Technique

Operation	Computer events	Time
Generate smoothing functions	$150(\pi J^2)\times10^{-6}$	0.05
Generate random numbers	$25(N+J)^2\times10^{-6}$	0.14
Convolution	$5(\pi J^2N^2)\times10^{-6}$	6.43
		6.59

However, the convolution technique can be considerably improved if the autocorrelation function is desired to be Gaussian. Again use is made of the fact that repeated self-convolutions yield a Gaussian distribution. Let s(x,y) be a square zero-one function. The smoothing operation is then repeated to achieve the Gaussian autocorrelation functions. Three convolutions do a good job. If the width of the desired smoothing function is J, then s(x,y) should be about J/3 on a side. By scanning with the zero-one function, the πJ^2 multiplications can be replaced with 2/3 J additions as the leading edge of the shifted s(x,y) is added and the trailing edge is subtracted. The computational time for this operation is shown in Table D.5.

Table D.5. Modified Convolution Technique

Operation	Computer events	Time
Generate random numbers	$25(N+J)^2$	0.14
Smooth with s(x,y)	$3(2/3\ JN^2)$	0.08
		0.22 units

This method is the quickest for the small autocorrelation widths which are typical. For the LOTS code the disadvantage of having to use a matrix of N+J on a side outweighs the advantage in time.

In the case of a matrix which is too large to fit completely into central memory, the modified convolution technique is the preferred method. In this situation the Fourier transform technique requires an out-of-core transpose which runs very slowly because of the large number of mass storage data exchanges. Using the larger matrix of N+J on a side is not a severe disadvantage if the matrix must be maintained in mass storage.

REFERENCES

Abramowitz, M., and I. A. Stegun, Handbook of Mathematical Functions, Dover Publications, New York (1964).

Ahrenkiel, R. K., J. F. Figueira, C. R. Phipps, Jr., D. J. Dunlany, S. J. Thomas, and A. J. Sievers, Appl. Phys. Lett. **33**, 705 (1978).

Avizonis, P. V., and R. L. Grotbeck, J. Appl. Phys. **37**, 687 (1966).

Beckmann, P., Probability in Communication Engineering, Harcourt, Brace and World, New York (1967).

Born, M., and E. Wolf, Principles of Optics, Pergamon Press, New York (1959).

Brigham, E., The Fast Fourier Transform, Prentice-Hall, New Jersey (1974).

Czuchlewski, S. J., A. V. Nowak, E. Foley, and J. F. Figueira, Opt. Lett. **2**, 39 (1978).

Dickson, L. D., Appl. Opt. **9**, 1854 (1970).

Figueira, J. F., W. H. Reichelt, G. T. Schappert, T. F. Stratton, and C. A. Fenstermacher, Appl. Phys. Lett. **22**, 216 (1973).

Frantz, L. M., and J. S. Nodvick, J. Appl. Phys. **34**, 2346 (1963).

Gaskill, J. D., Linear Systems, Fourier Transforms and Optics, Wiley, New York (1978).

Goodman, J. W., Introduction to Fourier Optics, McGraw-Hill, New York (1968).

Hopf, F. A., and M. Scully, Phys. Rev. B **1**, 50 (1970).

Innes, D. J., and A. L. Bloom, Spectra-Physics Laser Technical Bulletin, Vol. 5, Spectra-Physics, Inc., Mountain View, California (1966).

Jones, K. C., Preliminary Element Description, Los Alamos Scientific Laboratory, March 6, 1978.

Jones, K. C., and V. L. Zeigner, Los Alamos Scientific Laboratory Office Memorandum, L-10/78-088, February 7, 1978.

Lawrence, G., LOTS Manual, Optical Sciences Center, University of Arizona (1979).

Lawrence, G., I. Liberman, and V. Viswanathan, "Optical Analysis of the LASL 10 kJ CO_2 Laser Fusion System," paper presented at Optical Society of America, 1977.

Lawrence, G., and J. Munroe, "Effects of Window Segmentation on the Antares Laser Fusion System," paper presented at the Optical Society of America, 1977.

Lawrence, G., and W. Sweatt, "Application of the LOTS Computer Code to the Antares Laser Fusion System and Other Physical Optics Problems," paper presented at the Optical Society of America, 1978.

Lawrence, G., and P. Wolfe, Proceedings of the Los Alamos Conference on Optics '79, Los Alamos Scientific Laboratory, 1979.

Lax, M., G. P. Agrawal, and W. H. Louisell, Opt. Lett. 4, 303 (1979).

Loomis, J., FRINGE Manual, Version 2, Optical Sciences Center, University of Arizona (1976).

Loomis, J., Optical Interferogram Reduction and Interpretation, ASTM STP666, A. H. Guenther and D. H. Liebenberg, Eds., American Society for Testing Materials (1978).

Lowenthal, D. D., Appl. Opt. 13, 2126 (1974).

Montgomery, M. D., R. L. Carlson, D. E. Casperson, S. J. Czuchlewski, J. F. Figueira, R. F. Haglund, Jr., J. S. Ladish, A. V. Nowak, and S. Singer, Appl. Phys. Lett. 32, 324 (1978).

Phipps, C. R., Jr., and S. J. Thomas, Opt. Lett. 1, 93 (1977).

Rench, D. B., Appl. Opt. 13, 2546 (1974).

Rench, D. B., and A. N. Chester, Appl. Opt. 12, 997 (1973).

Richards, B., and E. Wolfe, Proc. Roy. Soc. A 253, 358 (1959).

Sargent, M., M. O. Scully, and W. E. Lamb, Jr., Laser Physics, Addison-Wesley, Reading, Massachusetts (1974).

Schappert, G. T., Appl. Phys. Lett. 23, 319 (1973).

Schappert, G., and E. Stark, Appl. Phys. Lett. 23, 602 (1974).

Siegman, A. E., and E. A. Sziklas, Appl. Opt. 13, 2775 (1974).

Stark, E. E., Jr., W. H. Reichelt, G. T. Schappert, and T. F. Stratton, Appl. Phys. Lett. 23, 322 (1973).

Sziklas, E. A., and A. E. Siegman, Appl. Opt. 14, 1874 (1975).

Viswanathan, V. K., J. E. Sollid, W. S. Hall, I. Liberman, and G. Lawrence, Optical Interferogram Reduction and Interpretation, ASTM STP666, A. E. Guenther and D. H. Liebenberg, Eds., American Society of Testing and Materials (1978).

Viswanathan, V. K., J. J. Hayden, and I. Liberman, Proceedings of the Los Alamos Conference on Optics '79, Los Alamos Scientific Laboratory, 1979.

Wolfe, P. N., A. C. Szxman, and G. Lawrence, Proceedings of the Los Alamos Conference on Optics '79, Los Alamos Scientific Laboratory, 1979.